Design and Analysis of an End-of-Arm Robotic Drilling Tool for Aerospace Manufacturing with Active Vibration Control

by

Mahdi Kazemiesfahani

A thesis submitted to the Faculty of Graduate Studies of

The University of Manitoba

In partial fulfilment of the requirements of the degree of

MASTER OF SCIENCE

Department of Mechanical Engineering

University of Manitoba

Winnipeg

Abstract

Automated drilling is crucial in aerospace manufacturing, significantly impacting production efficiency, quality, and safety. This thesis presents the design, prototyping, and analysis of the Advanced Collaborative Multifunctional End-Effector (ACME), a robotic drilling tool specifically developed for aerospace applications. ACME addresses key industry challenges by integrating lightweight design, collaborative robot (cobot) compatibility, precise positional control, and advanced vibration suppression capabilities.

ACME utilizes mechanisms for efficient planar movement, combined with a passive self-normalizing drilling head capable of maintaining normality on complex, double-curvature surfaces. The device is engineered to provide high clamping forces essential for multi-layered material stacks, while remaining within the payload limits of commercially available cobots. Experimental verification confirmed ACME's operational efficacy, achieving target performance metrics including a maximum clamping force exceeding 1000 N, rapid drilling cycles of approximately 12 seconds per hole, and an optimal workspace suitable for typical aerospace panel configurations. Despite minor deviations in geometric hole quality compared to CNC benchmarks, results were within acceptable aerospace standards.

A comprehensive dynamic model, developed and verified experimentally through frequency response functions (FRF), effectively characterizes system behaviors and supports precise vibration control. The thesis further investigates active vibration control (AVC) methods employing voice coil actuators (VCAs), demonstrating significant reductions in operational vibration amplitudes and enhancing overall drilling precision. The outcomes highlight ACME's potential as a cost-effective, flexible, and high-precision automated drilling solution for aerospace

manufacturing, laying the groundwork for future advancements in robotic automation and vibration control strategies.

Table of Contents

List of Tables

List of Figures

Nomenclature

Abbreviation	Definition
ACME	Advanced Collaborative Multifunctional End-Effector
cobot	Collaborative Robot
CNC	Computer Numerical Control
FRF	Frequency Response Function
AVC	Active Vibration Control
VCA	Voice Coil Actuator
DH	Denavit–Hartenberg (parameters)
FPK	Forward Pose Kinematics
IPK	Inverse Pose Kinematics
UR	Universal Robots (e.g., UR10, UR20 collaborative robots)
CRX	Collaborative Robot Series from FANUC (e.g., CRX-25iA)
KUKA	KUKA Robotics (e.g., LBR iisy cobot series)
ADU	Automatic Drilling Unit
TCP	Tool Center Point
FFT	Fast Fourier Transform
RMS	Root Mean Square
MS	MATLAB Simulink
CFRP	Carbon Fiber Reinforced Polymer
TMD	Tuned Mass Damper
ATMD	Adaptive Tuned Mass Damper
MRE	Magnetorheological Elastomer
DVF	Dynamic Vibration Feedback
MEMS	Microelectromechanical Systems
PID	Proportional–Integral–Derivative (controller)
COM	Center of Mass
CAD	Computer-Aided Design
HP	Horsepower
HDMI	High-Definition Multimedia Interface

GUI	Graphical User Interface
CMM	Coordinate Measuring Machine
DC	Direct Current
USB	Universal Serial Bus
GPIO	General-Purpose Input/Output
TTL	Transistor–Transistor Logic
ODE	Ordinary Differential Equation
RPM	Revolutions Per Minute
PCB	Printed Circuit Board
ICP	Integrated Circuit Piezoelectric (sensors)
SCADAS	Siemens Compact Data Acquisition System
QTY	Quantity

Acknowledgments

I would like to express my sincere gratitude and appreciation to Dr. Matt Khoshdarregi, my academic advisor and Dr. Amir Zargar, supervisor at the National Research Council Canada, for their invaluable guidance, support, and encouragement throughout my studies. Their incredible drive for success is evident in their work, and I am proud to be a researcher learning and growing under their supervision.

I would also like to thank my colleagues and friends at the Intelligent Digital Manufacturing Laboratory (IDM Lab) and Aerospace Manufacturing Technologies Center (NRC-AMTC) for fostering a collaborative and engaging research environment. In particular, I am deeply grateful to Aghiles Yousfi, Erfan Dilfanian, and Hamed Hosseini for their generous assistance and support, offered without hesitation or expectation, whenever it was needed.

This research was financially supported by the National Research Council Canada (NRC-CNRC).

Finally, I am forever grateful for my parents. I would not be where I am today in both my research and personal life without their love and support.

1 Introduction

Drilling is a fundamental operation in aerospace manufacturing, critically influencing productivity, quality, and safety standards in aircraft assembly lines. With hundreds of thousands of holes drilled per aircraft, achieving precise positioning, normality, and clamping force is paramount, especially for multi-layered composite materials such as carbon fiber-reinforced polymer (CFRP), aluminum, and titanium. Manual drilling methods are labour-intensive, prone to errors, ergonomically challenging, and lack flexibility in adapting to engineering changes. Existing automated drilling solutions, though precise, often require substantial capital investment, extensive floor space, and strict safety barriers, limiting their applicability in collaborative work environments.

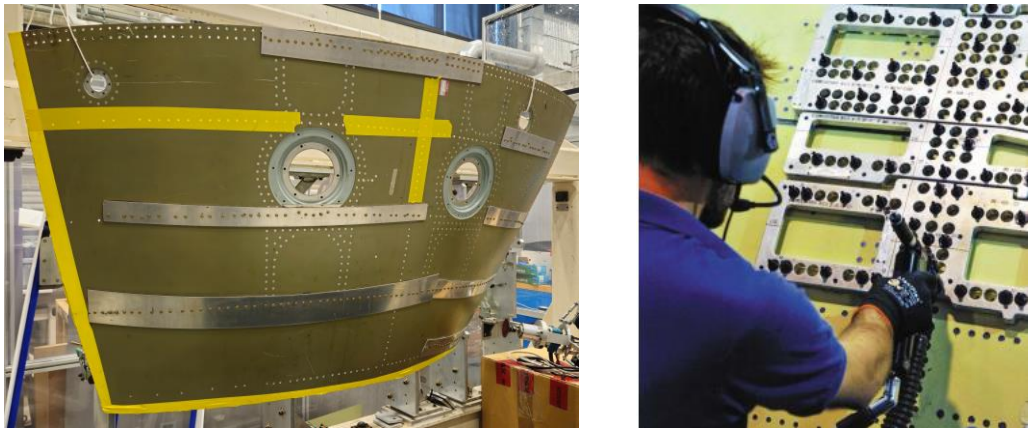

Figure 1-1, (a) aerospace panel, (b) Manual drilling in aerospace manufacturing

In response to these limitations, this thesis proposes the Advanced Collaborative Multifunctional End-Effector (ACME), a novel robotic drilling tool explicitly designed for collaborative robot (cobot) integration. ACME aims to revolutionize automated aerospace drilling by combining cost efficiency, high operational flexibility, enhanced precision, and inherent safety for human-robot collaboration. The device employs a lightweight design to remain within typical cobot payload capacities (<30 kg) and features innovative mechanisms for efficient motion, passive self-normalization for precise drilling alignment on complex geometries, and integrated vacuum-

assisted clamping to provide substantial clamping forces essential for maintaining structural integrity during drilling.

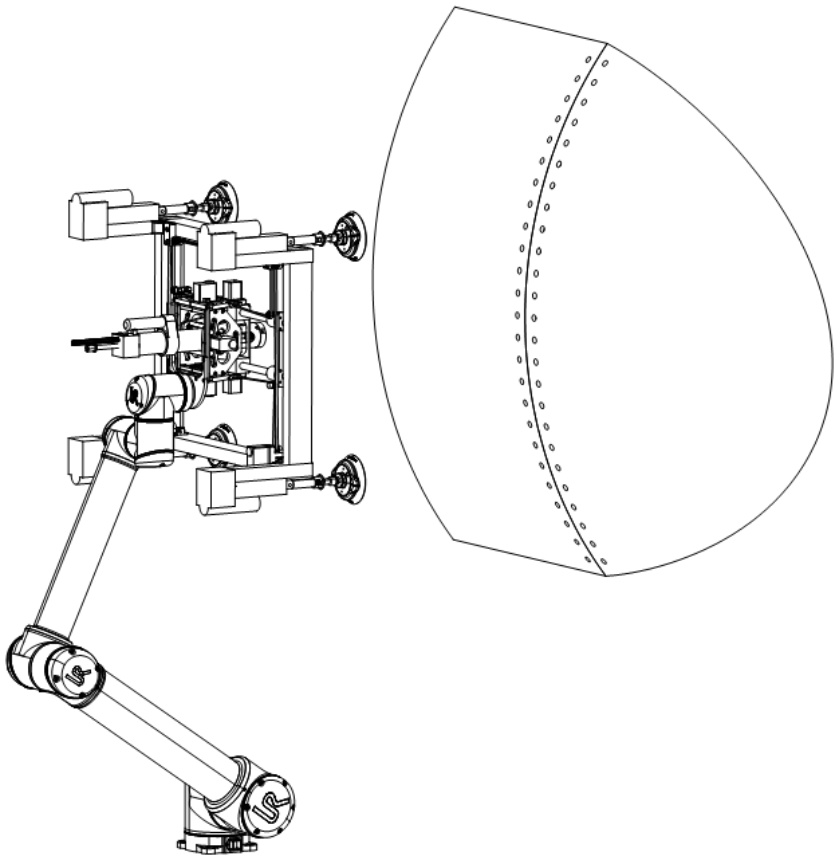

Figure 1-2, ACME mounted on top of a UR10 cobot

Additionally, the inherent flexibility in robotic systems, often causing vibrations detrimental to precision, has been systematically addressed through comprehensive dynamic modelling and experimental verification. This thesis further explores active vibration control (AVC) techniques utilizing voice coil actuators (VCAs), effectively mitigating vibrations during the simulation and ensuring adherence to stringent aerospace drilling tolerances.

Objectives and Contributions

The objectives of this research are to:

- Develop and prototype an advanced collaborative drilling end-effector suitable for aerospace manufacturing and integration with collaborative robots (cobots).
- Integrate robust kinematic and dynamic models to facilitate precise motion planning and accurate predictions of structural behaviour.
- Implement effective Active Vibration Control (AVC) methods to minimize vibration-induced errors during drilling operations.
- Verify the prototype and developed models' performance in simulation and experimentally to confirm their capability to meet aerospace standards for quality and efficiency.

The collaborative and integrated nature of this research, supported by the National Research Council Canada (NRC-CNRC), provides a robust foundation for advancing automated drilling technologies, significantly benefiting aerospace manufacturers in Canada and globally.

2 Literature Review

2.1 Introduction

Automated drilling in aerospace manufacturing is essential due to stringent requirements for precision, productivity, and safety. Advances in robotics, automation, and control systems address complex issues related to multi-layered drilling, curved surfaces, and tight aerospace tolerances. This comprehensive literature review explores scholarly advancements across primary domains like automated drilling devices, dynamic analysis, and vibration suppression and control.

2.2 Automated Drilling

Automated drilling systems have significantly advanced aerospace manufacturing processes by enhancing precision, repeatability, and safety. Precise control of drilling and clamping forces is especially crucial when working with complex, multi-material stacks composed of carbon fibre-reinforced polymers (CFRP), aluminum, and titanium. Several studies have explored critical aspects of aerospace drilling, emphasizing the importance of optimal drilling parameters and clamping force control. Research in [1], [2], [3], [4] demonstrated that precise control over clamping forces is essential to reduce interlayer chip formation and interface damage, thereby improving hole quality. Their force-deformation models indicated that reducing interlayer gaps significantly mitigates damage to the surface, especially critical when drilling CFRP/Ti stacks. Required clamping forces, essential for aligning layers during drilling operations, typically range from 500 N to 1500 N, contingent upon material stiffness. Titanium, due to its hardness, necessitates higher thrust and thus greater clamping forces compared to aluminum and CFRP, highlighting material-specific force requirements [2]. Similarly, Pardo [5] investigated multi-material aerospace stacks and underscored how adjusting drilling forces and cooling parameters

can lead to enhanced borehole quality and reduced tool wear, particularly when dealing with CFRP and titanium layers.

Maintaining normality during drilling is equally vital for aerospace manufacturing, where angular deviations are strictly controlled within ±0.5° [6], [7]. Systems developed by Jie and Shu-Hui [6] and Shi et al. [7] utilize advanced methods such as eccentric disks and real-time laser-based adjustments to maintain normality, ensuring precision during complex operations. Additionally, Chen et al. [8] developed a laser sensor-based orientation adjustment system effective for double-curvature surfaces. Yuan et al. [9] proposed a passive positional correction approach using an extreme learning machine, capable of predicting and correcting positional errors without continuous sensor feedback, significantly enhancing positioning accuracy. An "auto-normalization algorithm" using multiple laser sensors has also been introduced in [10] to estimate and maintain surface normality effectively. Efficient chip management is another critical factor in aerospace drilling, particularly when drilling CFRP/Ti stacks. Poor chip evacuation can lead to delamination and compromised hole integrity. Laporte et al. [11] demonstrated that vibration-assisted drilling effectively reduces chip size and enhances evacuation, producing smoother hole finishes and minimizing the need for subsequent finishing operations, crucial for aerospace component quality [11].

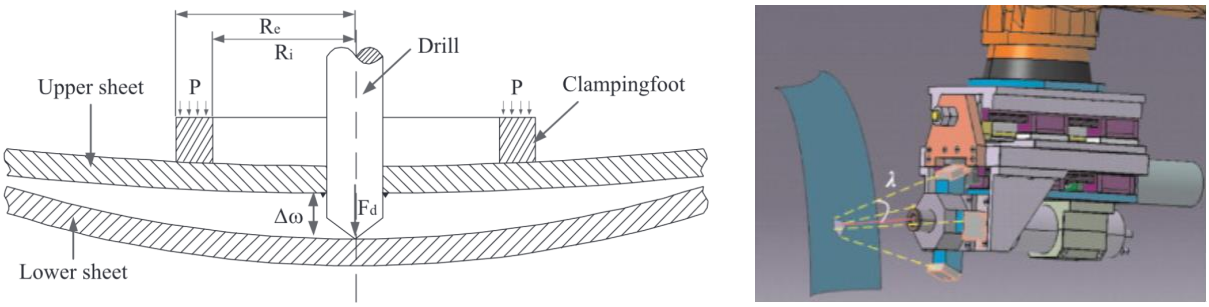

(a) *(b)*

Figure 2-1, (a) applied clamping forces using clamping foot [4], (b) sensor-based normality detection and compensation [10]

Furthermore, recent literature highlights jig-less robotic drilling solutions to improve flexibility and reduce setup time. Marguet et al. [12], Cirillo et al. [13], and systems like MTM Robotics' Mini FlexTrack [14] illustrate crawling drilling robots, collaborative systems, and flex-track structures, offering localized clamping forces adaptable to complex geometries. These jig-less approaches contrast starkly with traditional rigid jigs, significantly enhancing manufacturing flexibility, reducing setup times, and optimizing workspace utilization in aerospace production environments.

Safety considerations are integral to automated aerospace drilling, particularly in collaborative settings involving human-robot interactions. Traditional industrial robots, characterized by high inertia and rigidity, present notable safety hazards. Solutions such as passive compliance mechanisms in robot joints [15], end-effector airbags [16], and low-impedance actuation methods [17] effectively mitigate collision risks and enhance operational safety. Additionally, employing lightweight materials, including aluminum and carbon-fibre composites, contributes to lower inertia and safer interaction environments [18], [19].

Collaborative robots (cobots), designed explicitly for safe interaction with human workers, represent a practical solution for automated aerospace drilling. Nevertheless, their limited payload capacities and structural stiffness present challenges. To overcome these, techniques such as trajectory optimization and gravitational load-balancing have been employed to enhance cobot payload capacities without significantly increasing structural mass [20], [21]. Flexible link manipulators and variable stiffness mechanisms have also been explored to improve payload-to-mass ratios, enhancing energy efficiency and maneuverability without sacrificing precision [19], [22]. Furthermore, the Independent Load And Measurement Arm (ILAMA) concept decouples

load measurement from load-bearing structures, allowing cobots to optimize payload capabilities while preserving the precision necessary for aerospace applications [18].

Crawler Robots
- Attaches using suction cups to apply necessary forces
- The moving mechanism (crawling) is too slow
- Not suitable for double curvature

Flex-Tracks
- Flexible rail of suction cups
- Reported slippage and malfunction during operation
- Long installation time
- Not suitable for double curvature

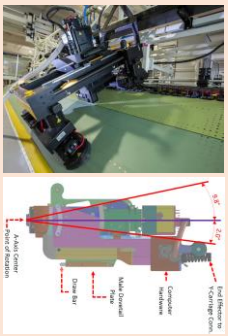

KUKA-ALEMA
- End of Arm tool for drilling
- High quality using real-time force control
- Huge footprint and unsafe work area
- Significant capital investment

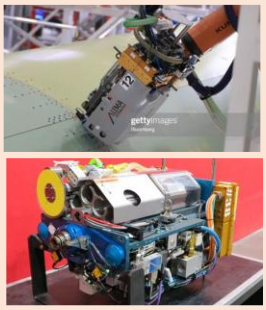

Solution by ARM
- End of Arm tool for drilling using cobots
- Attaches using suction cups
- One hole per attachment of the end-effector to the surface

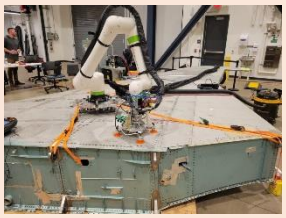

Solution by DLR
- C-clamp ADU on cobot
- Using AMRs to move the cobots
- Limited to holes close to edges

Solution by Safran
- ADU (Automatic Drilling Unit) on cobot end-effector
- Helps the operator to handle the ADU
- No clamping force or normality comp. provided

Figure 2-2, Summary of the existing automated drilling methods

2.3 Dynamic Analysis and Vibration Control

Dynamic analysis is essential in robotic drilling systems to accurately predict the response and performance of the robot under operational conditions. Accurate modelling and analysis of robot dynamics is crucial to enhance positional and orientational precision, ensuring the quality and integrity of drilled holes in aerospace manufacturing. The ACME system's dynamic and vibration response can significantly impact its drilling accuracy and predictability, making it necessary to understand and control the sources and effects of vibrations within the robotic system.

Robotic drilling systems rely extensively on precise kinematic and dynamic models to achieve the required accuracy. The Denavit-Hartenberg (DH) convention is widely utilized for modelling robotic manipulators, facilitating systematic forward and inverse kinematic solutions necessary for accurate trajectory planning and control [23]. Recent studies emphasize hybrid robotic systems that combine prismatic and rotational joints to better handle complex aerospace drilling operations on curved surfaces [8], [9]. Dynamic modelling critically influences drilling accuracy by capturing essential factors such as joint flexibility and structural compliance. Newton-Euler and Lagrangian approaches are common methods for deriving dynamic equations. Wang and Keogh [24] highlight the importance of accurately modelling joint flexibility to achieve realistic simulation results. Similarly, Huynh and Altintas [25] underscore the predictive accuracy gained by incorporating flexible joint dynamics into robotic drilling systems.

Precise dynamic simulations depend heavily on experimentally identified joint stiffness and damping parameters. Studies by Zaeh et al. [26] and Chen and Ahmadi [27] demonstrate the necessity of high-fidelity dynamic models through experimental verification of stiffness and damping, which are indispensable for the deployment of effective vibration control strategies.

Vibrations in robotic drilling can critically degrade hole quality and surface finish. The primary sources include environmental vibrations, inertial vibrations due to rapid movements, and process-induced vibrations.

Environmental Vibration: Originates externally, transmitted through the base structure. These vibrations are typically mitigated through passive or semi-active isolation methods, such as quasi-zero stiffness systems [28] or magnetorheological damping [29].

Inertial Vibration: Arises from residual energy during abrupt movements or high-jerk trajectories. Thomsen et al. [30] propose trajectory optimization and input shaping techniques to minimize these inertial effects, thereby enhancing robotic precision.

Process Vibration: Occurs from self-excited vibrations during drilling, affecting surface quality and tool life. Process vibrations are primarily controlled through the optimization of cutting parameters and implementing active vibration control methods [31], [32].

Multiple methods are proposed to mitigate the unwanted effects of these sources of vibrations. Effective vibration suppression in robotic systems is categorized into three primary methodologies:

Passive Systems: Include structural reinforcements and tuned mass dampers (TMDs). These methods improve structural stiffness and stability but lack adaptability to changing operational conditions. Key studies are summarized in Table 2-1.

Table 2-1, Summary of studies on passive vibration control

Reference	*Methodology*	*Outcome*
[32]	Integrated mechanical shock absorber in tool	Increased process efficiency by 53%
[33]	Installed four tunable mass dampers (TMDs)	Reduced vibration amplitude by 98%

[34]	Implemented adaptive tunable mass dampers (ATMDs)	Reduced dominant spindle frequency by 17%

Semi-Active Systems: Utilize devices such as Magnetorheological elastomer (MRE) absorbers. These systems adapt stiffness and damping in real-time, providing superior adaptability. Yuan et al. [35] highlight MRE's effectiveness in suppressing dynamic vibrations through real-time feedback control.

Active Systems: Employ active vibration control (AVC) strategies that counteract vibrations through real-time actuator adjustments based on sensor feedback. These systems, such as those implemented by Wang and Keogh [24] and Zaeh et al. [26], have demonstrated substantial reductions in vibration amplitudes and adaptability to varying conditions.

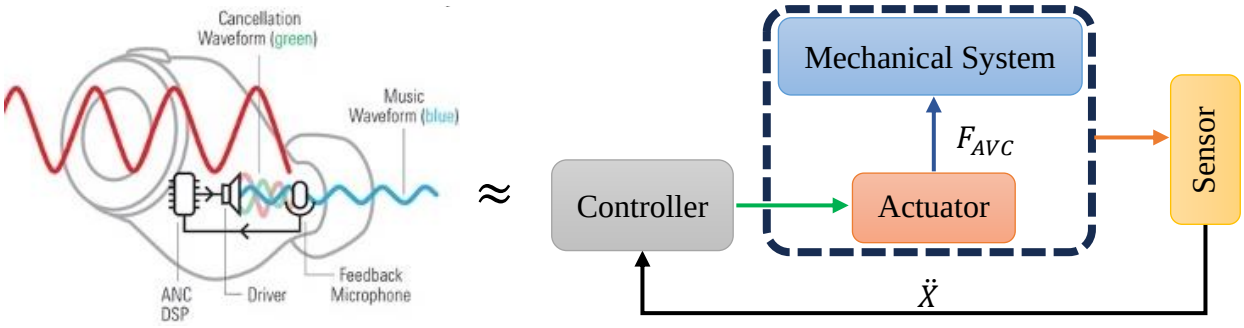

Figure 2-3, General schematic of the principals of an AVC and its similarity to a sound noise cancellation

AVC is the most sophisticated vibration suppression approach, leveraging real-time feedback loops with sensors (e.g., accelerometers) and actuators (e.g., voice coil actuators) to counteract vibration actively. However, AVC systems demand precise frequency response function (FRF) identification and accurate knowledge of the system's dynamic characteristics, such as stiffness and damping and they require high sampling and actuation frequencies for effective control.

Accurately identifying the system's Frequency Response Function (FRF) under different excitations is essential for developing active controllers. Techniques such as automatic FRF extraction have been investigated by various researchers [26], [36], [37]. These methods use external high-frequency actuators to apply forces, extract the FRF, and subsequently determine critical model parameters such as stiffness and damping. Nevertheless, actuator limitations, including force and frequency saturation, must be carefully considered. Table 2-2 summarizes recent AVC methods employed in robotic systems.

Table 2-2, Summary of AVC methods

Reference	*Sensing*	*Actuation*	*Max. Output Force*	*Controller*
[24]	MEMS 3-axis accelerometer (5000 Hz)	Voice coil actuator	15.6 N force output	PID
[26]	Accelerometer	Magnetic Actuator	45 N at 1000 Hz	DVF & H∞
[36]	Accelerometer	Piezoelectric Actuator	-	Proportional (P)
[37]	Accelerometer	Voice Coil Actuator	89 N at 1000 Hz	Proportional (P)

These AVC systems utilize advanced control algorithms, including proportional-integral-derivative (PID) and robust H∞ controllers, to dynamically mitigate vibrations based on real-time data, significantly enhancing system precision and stability [24], [26]. Active vibration controllers enable broader vibration suppression capabilities and robustness across varying robot poses [31].

2.4 Summary

Automated drilling plays a pivotal role in aerospace manufacturing, significantly impacting production efficiency, precision, and safety. The reviewed literature emphasizes critical developments in automated drilling devices, dynamic analysis, and vibration suppression methodologies.

Advancements in automated drilling have led to enhanced precision and safety, particularly in multi-material stacks common in aerospace structures. Key research highlights include the importance of precise control over clamping forces to prevent defects like interlayer chip formation and delamination. Maintaining normality during drilling is equally crucial, with studies highlighting various sensor-based active and passive compensation methods to ensure angular accuracy within stringent aerospace standards. Jig-less robotic solutions, such as crawler robots, flex-tracks, and collaborative robots (cobots), provide improved flexibility, reduced setup time, and safer interactions in comparison to traditional automated systems, though they present limitations in speed, payload capacity, and structural stiffness.

Dynamic analysis forms the basis for accurately predicting robotic drilling performance. Accurate kinematic and dynamic modelling, notably through Denavit-Hartenberg parameters and flexible joint considerations, facilitates precise motion planning and control. The Newton-Euler and Lagrangian methods are predominant for deriving dynamic equations, with experimental verification crucial for parameter accuracy.

Vibration control, essential for maintaining hole quality and precision, addresses environmental, inertial, and process-induced vibrations. Passive methods provide basic vibration mitigation through structural modifications, whereas semi-active and active systems offer adaptive vibration

suppression. Active vibration control (AVC) employs real-time feedback and actuator responses, showing superior performance and adaptability. Detailed frequency response function (FRF) identification is critical for AVC implementation, guiding effective controller development. Future research should focus on refining active vibration control strategies, improving experimental parameter identification, and enhancing system adaptability for diverse aerospace drilling scenarios.

3 Design and Prototyping

3.1 Introduction

The development of a specialized drilling end-effector for curved and multi-layered aerospace components demands a careful balance of mechanical, electronic, and operational requirements. This chapter presents the process of designing and prototyping ACME (Advanced Collaborative Multifunctional End-Effector), an automated End-of-Arm drilling tool that aims to provide high clamping force, accurate positioning, and collaborative-safe interaction with its operator. Meeting the strict tolerances required in aerospace drilling that needs a lightweight yet rigid structure, precise linear and rotary motions, and robust sensing and control hardware, all of which must be integrated into a single cohesive system. Consequently, every aspect of ACME's design, from the initial requirements to the final assembled prototype, reflects the need for reliability, repeatability, and ease of deployment on a shared factory floor.

The chapter proceeds by outlining the key design requirements and constraints that guided the system's architecture. Then delves into the end-effector's mechanical structure, detailing the design choices, actuation, and sensing that collectively ensure quality, meeting operational forces, and a sufficiently large workspace for drilling tasks on double-curvature surfaces. The subsequent sections focus on the mechatronics and control components that enable ACME to achieve accurate motion and real-time feedback. Finally, the essential specifications and capabilities of the prototype are consolidated, and these design decisions lay the foundation for ACME's kinematics, dynamic modelling, vibration control, and simulated verifications that are discussed in subsequent chapters.

3.2 Requirements and Constraints

The development of an automated drilling end-effector for aerospace manufacturing necessitates the fulfillment of several stringent requirements, each of which helps ensure reliable performance under production-line conditions.

A sufficiently high clamping force is critical for maintaining layer compression in stacked composite/metal assemblies and for preventing unwanted interlayer burr formation during drilling. As suggested in [4], a minimum clamping force of 500 N is necessary to close the gap between two aluminum sheets with a thickness of 2mm. As a result, a minimum of 700 N of clamping force capacity was considered as a design objective for prototyping ACME. Meeting this threshold is necessary to ensure that the gaps do not form between the stacked layers, thereby mitigating burrs and delamination in aluminum and CFRPs.

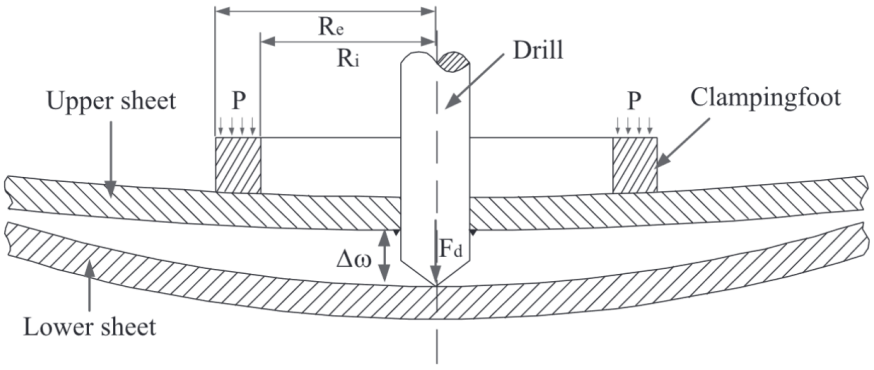

Figure 3-1, Clamping force is applied using the clamping foot to close the gap between the stacked aluminum sheets [4]

By integrating ACME with a cobot, a highly cost-effective, adaptable, and safe drilling solution is achieved. Conventional automated drilling solutions rely on large, high-payload robots that require substantial floor space and strict safety enclosures to prevent potential hazards. Their considerable footprint makes them less adaptable in constrained production environments and unsuitable for direct human interaction. Compared to conventional automated drilling systems, which often

exceed a million dollars in initial investment, the ACME-cobot combination presents a much more affordable alternative. This solution also enables aerospace manufacturers to adopt automation without the prohibitive safety measures of large-scale industrial robotic systems, ultimately improving production efficiency while maintaining flexibility in manufacturing processes by reducing the footprint of industrial automation.

Figure 3-2, Large footprint and safeguards of existing robotic drilling solutions

A primary objective of ACME's weight management is to ensure seamless integration with cobots, including models such as the KUKA LBR iisy 15 R930 (15 kg payload), the Fanuc CRX-25iA (25–30 kg payload), and the UR20 (25 kg payload). High-end cobots typically offer payload capacities in the 15–30 kg range. By keeping ACME's total mass at or below 20 kg, it remains feasible for most common cobots to handle while preserving a buffer for dynamic loads. This enables ACME to effectively expand a cobot's static drilling capability while ensuring operational safety close to human-robot collaborative settings.

(a) (b) (c)

Figure 3-3, (a) The UR20. (b) Fanuc CRX-25iA. (c) KUKA LBR iisy 15 R930. Three high-end collaborative robots

Ensuring normality during drilling on double curvature surfaces is a critical design requirement for ACME. Deviations from normality can lead to out-of-tolerance hole geometry, increased tool wear, and poor fastener fitment, all of which are unacceptable in aerospace applications. ACME must adjust the drilling bit angle to the surface, enabling it to adapt to varying surface geometries. Figure 3-4 illustrates a representative double curvature surface, highlighting the challenges posed by varying surface normal vectors and the necessity of normality compensation mechanisms.

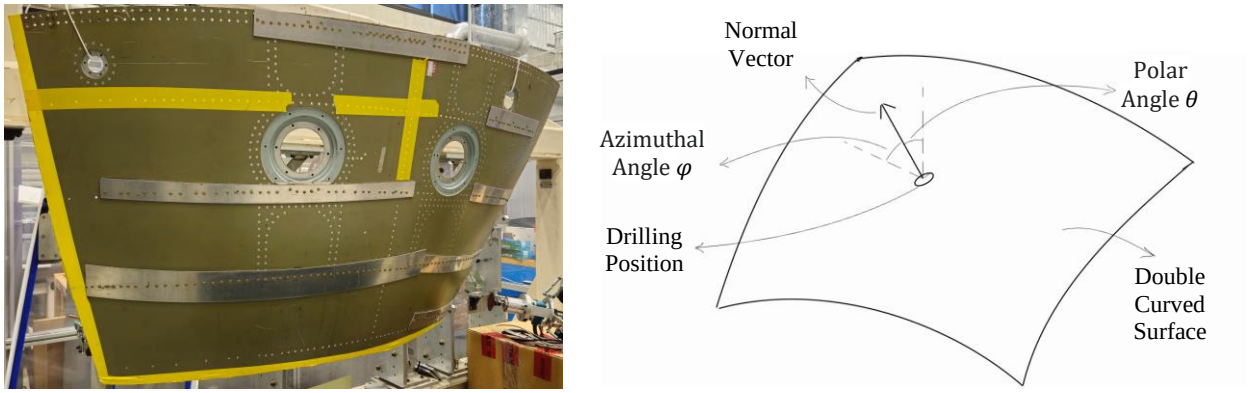

Figure 3-4, Double curvature surfaces in aerospace manufacturing

The workspace of ACME must be sufficiently large to allow efficient and uninterrupted drilling operations. A key requirement is that ACME covers an area large enough to drill multiple holes without the need for frequent major repositioning, thereby minimizing delays associated with reattaching the end-effector for each individual hole. This capability significantly improves productivity by reducing idle time and ensuring rapid execution of drilling sequences. The workspace must accommodate typical aerospace drilling patterns, allowing the system to handle a series of holes within a single setup before requiring relocation.

Table 3-1 outlines the aforementioned core attributes, ranging from weight limits and clamping force to affordability, ranking them by importance on a scale of 1 to 5, with 5 denoting the most critical. These attributes collectively address the practical and technical demands of multi-layered, curved-surface drilling for aircraft structures.

Table 3-1, List of design requirements and their respective rankings

Attribute	*Ranking*
Light-weight design	5
Meet Minimum Required Clamping Force	5
Range of Operation (Workspace)	4
Quick Positioning and Fast Drilling Cycle	3
Accurate Positioning and Normality Compensation	2
Affordability (Low-cost design)	1

All these requirements, encompassing weight constraints, clamping force, accurate positioning, workspace, rapid attachment, and cost-effectiveness, must be addressed in a single cohesive design to ensure reliable aerospace drilling. The overall mass of the end-effector must remain below the collaborative robot's payload limit (20kg, per Table 3-2) to prevent excessive strain on the cobot's actuators. A clamping force of at least 700 N (also from Table 3-2) is critical for compressing stacked layers and avoiding defects like delamination, with Table 3-1 ranking this attribute at the

highest level (5). An adequately sized workspace, no less than 300 mm in its largest dimension, as indicated in Table 3-2, enables drilling on large or curved fuselage sections without frequent repositioning. Rapid system setup and repositioning are also key, reflected by a 10-minute assembly threshold and typical per-hole positioning times under 10 seconds, both of which directly affect production throughput. Although ranked lower (1) for the primary prototype in Table 3-1, affordability remains a major motivator, keeping the cost near 25,000 CAD so the solution can compete with expensive, large-footprint automated drilling cells. By meeting these specifications collectively, the end-effector achieves the necessary balance of lightweight construction, secure clamping, precision drilling, flexible reach, quick deployment, and cost-effectiveness, thereby aligning with the demanding environment of aerospace manufacturing.

Table 3-2, Quantitative values of the technical Specifications

Characteristics	*Objective*	*Threshold Value for the prototype*	*Ideal Value*
Weight (M)	↓	20 kg	$M \leq 15\ kg$
Setup Time (T_s)	↓	2 min	$T_a \leq 1\ min$
Positioning time of the drilling head (T_p)	↓	15 s	$T_p \leq 10\ s$
The Longer Dimension of the Workspace (LW)	↑	300 mm	$LW \geq 300\ mm$
Minimum clamping force (F_c)	↑	700 N	$F_c \geq 900\ N$
Positioning Error (P-E) *Normal Error (N-E)*	↓	P-E: 1 mm N-E: 2°	P-$E \leq 0.2\ mm$ N-E $\leq 0.5°$
Cost (C)	↓	25,000 CAD	$C \leq \$25{,}000$

3.3 ACME Prototype that Meets the Requirements

ACME is designed as a compact, five-degree-of-freedom (5-DoF) system that combines three linear axes (X, Y, and Z) with two rotational axes (A and B). This configuration enables both planar translation and precise angular adjustments for maintaining normality on curved surfaces. A lightweight outer frame serves as the main structure onto which Z-axis linear actuators, X–Y carriages, sensors, and the drilling head are mounted (containing the A and B rotational mechanisms). The system integrates a load cell for force measurement and uses vacuum-assisted suction cups for stable attachment and clamping on the surface. By attaching to a collaborative robot, ACME leverages the cobot's reach and inherent safety features while compensating for its limited payload capacity through direct surface attachment.

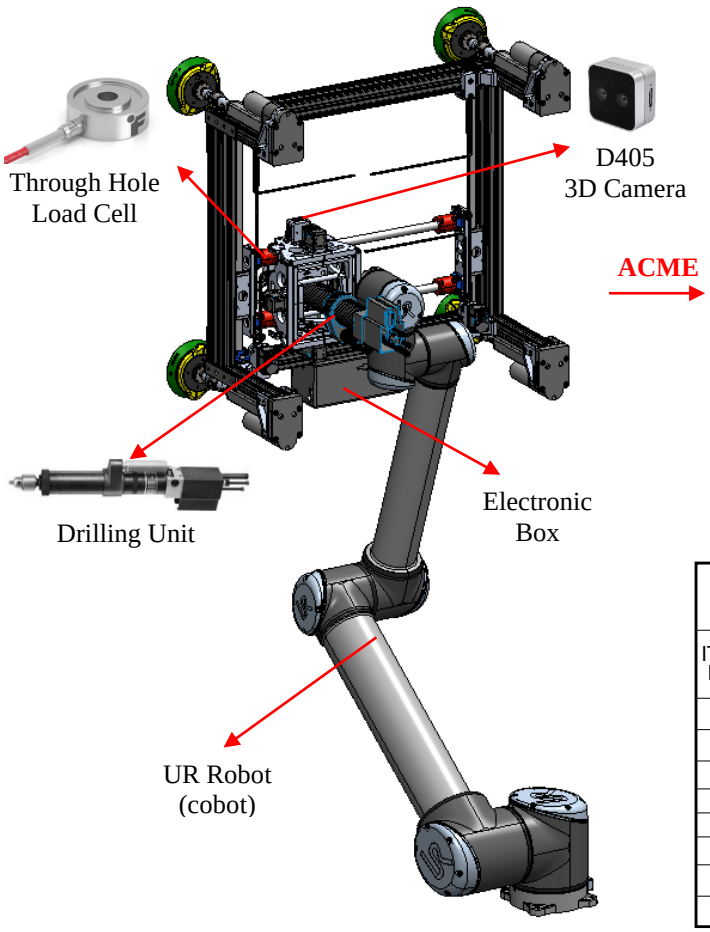

ACME

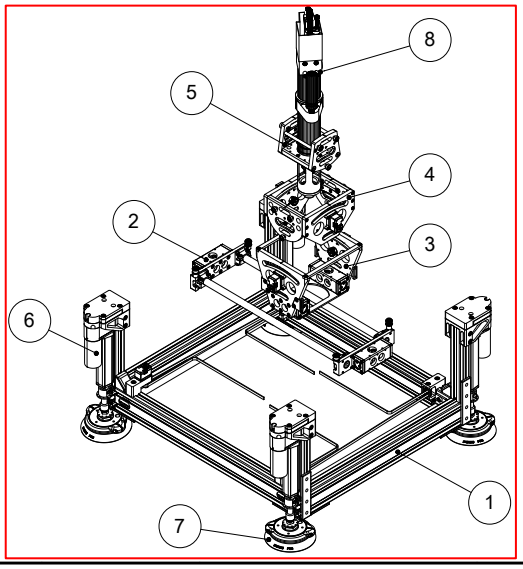

BOM Table

ITEM NO.	PART NUMBER	DESCRIPTION	QTY.
1	ACME-01-00-00	Main Body	1
2	ACME-02-00-00	X Carriage	1
3	ACME-03-00-00	Y Carriage	1
4	ACME-04-00-00	A Rotation	1
5	ACME-05-00-00	B Rotation	1
6	ACME-06-00-00	Z (Clamping) Linear Actuator	4
7	ACME-07-00-00	Suction Cup	4
8	DU	Drilling Unit	1

Figure 3-5, ACME connected to a cobot

The primary load-bearing element is the rigid outer frame, constructed from aluminum profiles to withstand typical aerospace drilling and clamping forces. Four linear actuators, each equipped with a suction cup, provide the Z-axis travel and clamping action by pressing the frame upward or downward against the workpiece. For X–Y motion, ACME incorporates a carriage assembly that traverses along belt-driven rails in a CoreXY configuration, ensuring low friction and minimal backlash. The CoreXY mechanism is a parallel kinematic motion system that employs two stationary motors connected by belts in an intertwined configuration, allowing precise, planar motion in two dimensions (X and Y) through coordinated movements of these motors. This arrangement reduces moving mass, preserves rigidity, and enables swift positioning of the drilling head. The synchronized movement of the X and Y carriages thus provides a stable, repeatable platform for drilling hole patterns over a defined workspace, without requiring frequent re-attachments or complex robot motions.

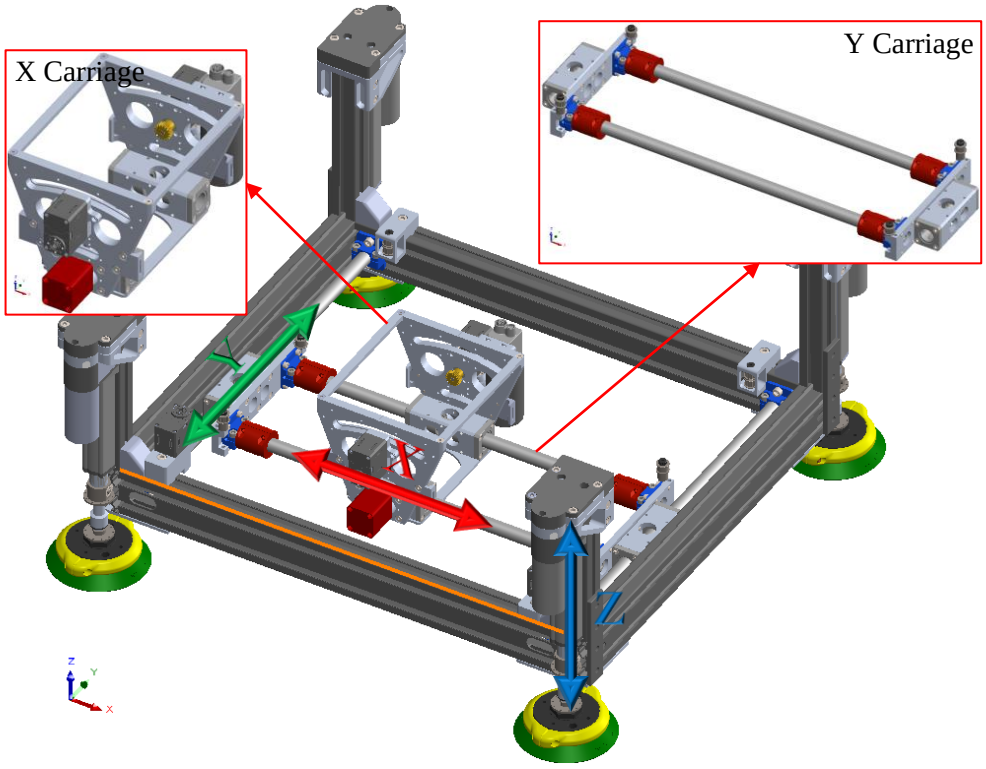

Figure 3-6, X-Y-Z motions are provided by two carriages and 4 synchronized linear actuators

CoreXY Mechanism for X-Y Motion

ACME utilizes a CoreXY mechanism for achieving precise planar (X-Y) positioning of the drilling tool. This arrangement involves two independently controlled motors positioned on the stationary outer frame, connected through a belt-and-pulley transmission. Such a design significantly reduces the inertia of moving parts, enabling faster response times and improved positional accuracy. Due to its advantages, including minimal backlash, compactness, and high positional precision, the CoreXY configuration is prevalent in systems requiring accurate planar movements, such as 3D printers, CNC machines, and advanced robotic applications. Advantages of CoreXY for ACME:

- **Reduced moving inertia:** Motors mounted on the stationary frame enhance responsiveness and accuracy.
- **Minimized backlash:** The belt-driven mechanism ensures precision and repeatability.
- **Efficient use of space:** Compact structure facilitating ease of maintenance and integration into constrained workspaces.
- **Simple synchronization:** The coordination of two motors simplifies planar positioning, allowing precise diagonal, linear, and single-axis movements with ease.

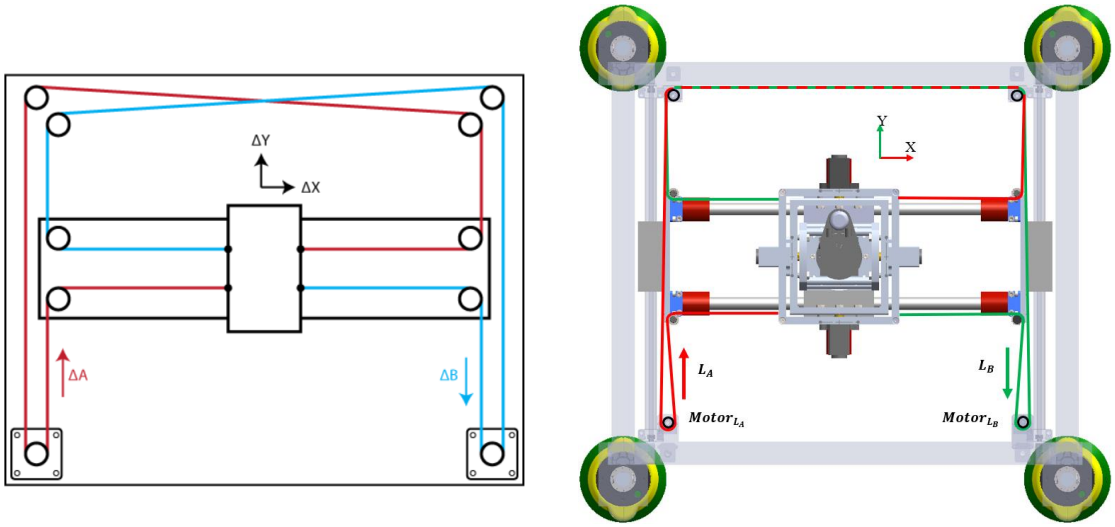

Figure 3-7, (left) Schematic of the CoreXY mechanism [38], (right) CoreXY mechanism in ACME

Directly at the drilling head, two rotational axes (pitch and yaw, respectively labelled A and B) enable the end-effector to accommodate variations in surface curvature. These axes are housed in a compact gimbal-like mechanism located on the X carriage. Depending on the design constraints, they may be driven either actively (using servo motors for precise tilt control) or passively (through reaction forces and mechanical linkages). The goal is to maintain the normality of the drilling bit relative to contoured surfaces, thus improving hole quality and reducing taper or out-of-round defects. Each axis provides a ±10° tilt range of axes A and B to compensate for normality on double-curvature aerospace panels.

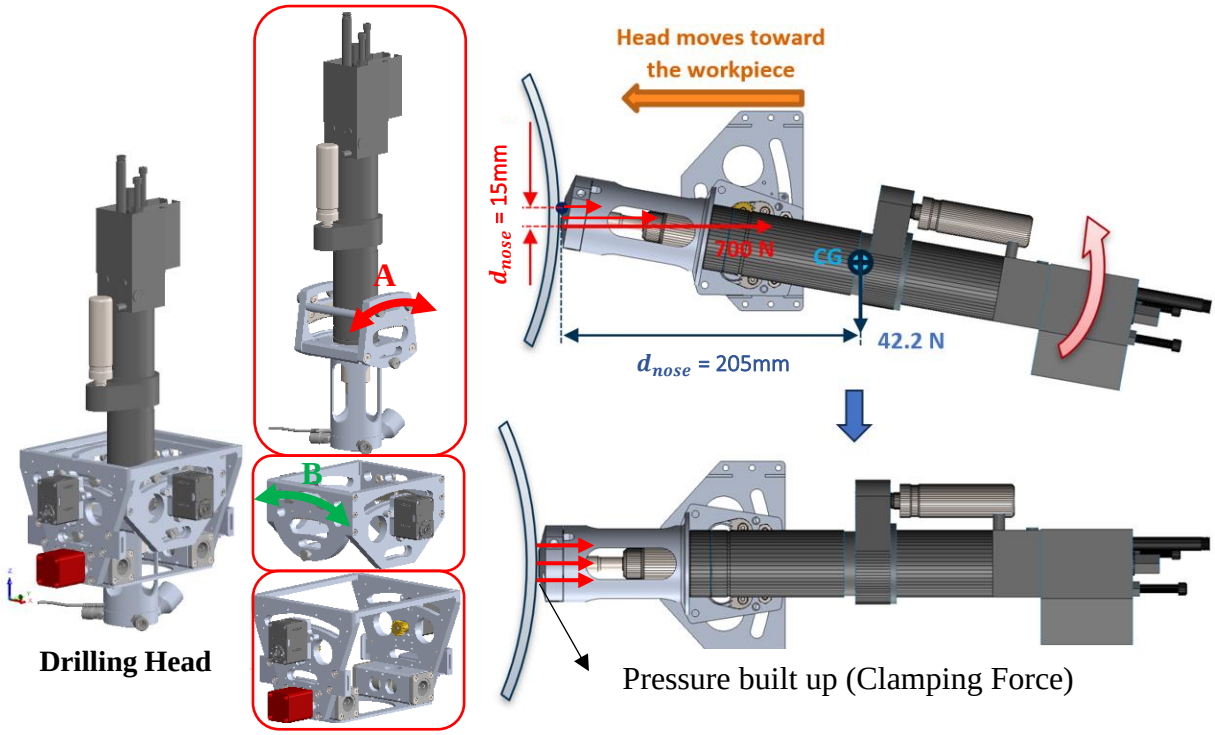

Figure 3-8, Auto self-normalization of the nose to compensate for the normality on double curvature surfaces

For the passive normalization to occur, the torque induced by the reaction of the clamping force at the drilling nose must overcome the gravitational moment (worst case) acting on the drilling unit, thus causing the unit to rotate and align itself perpendicularly to the drilling surface. The

equilibrium equation for passive normalization can be described by equating the moments about the center of rotation:

$$\sum M = 0 \tag{3.1}$$

In this system, two primary moments are acting around the pivot point. Gravitational Moment (M_g), acting to rotate the drilling unit away from normal orientation. Reaction moment from clamping force (F_{clamp}), acting through the drilling nose, causing the system to align with the surface normal.

These moments can be expressed as:

$$M_{gravity} = m.g.d_{com} \tag{3.2}$$

$$M_{clamp} = F_{clmap}.d_{nose} \tag{3.3}$$

Where m is the mass of the drilling unit (4.22kg), g is the gravitational acceleration ($9.81\ m/s^2$), d_{com} is the horizontal distance between the pivot (center of rotation) and the center of mass of the drilling unit (205 mm), F_{clmap} is the reaction force at the drilling nose (applied clamping force), and d_{nose} is the distance from the center of rotation to the location where the clamping force is applied at the nose (15 mm, half of the nose diameter of 30 mm). For the passive normalization mechanism to initiate rotation, the torque from the reaction of clamping forces at the drilling nose must at least equal the gravitational torque acting on the system:

$$F_{clmap}.d_{nose} \geq m.g.d_{com} \tag{3.4}$$

Rearranging the equation to find the minimum required clamping force (F_{min}):

$$F_{min} = \frac{m.g.d_{com}}{d_{nose}} \tag{3.5}$$

Thus, substituting known values, the minimum required clamping force (F_{min}) to achieve passive normalization will be 565.77N.

At the final stage of the mechanical assembly, the drilling head, a 0.50 HP pneumatic auto-feed aerospace standard drilling unit, is mounted onto the A–B tilting mechanism. This pneumatic drill operates at standard shop air pressures (about 90 psi), providing a feed range of up to 32 mm (1-1/4 inch) and torque suitable for multi-layered aluminum stacks. A through-hole load cell is aligned concentrically with the drill bit to measure thrust and clamping force in real-time, enabling closed-loop force control and uniform hole quality. The assembly is deliberately lightweight to accommodate typical cobot payloads yet sufficiently robust to handle drilling in reinforced composites and aluminum stacks. Secure integration of the drilling unit, combined with the system's load-sensing capability, ensures consistent, high-precision performance across a wide range of aerospace drilling conditions.

3.4 Electronics and Sensors

The ACME system integrates multiple electronic components to enable precise actuation, sensing, and control for aerospace drilling applications. A Raspberry Pi board serves as the central processor, managing sensor inputs and actuation commands. It interfaces with peripheral devices such as load cells, actuator encoders, and vacuum sensors, ensuring accurate data acquisition for force and position control. Commands are sent via serial communication to actuators and relays to control electrical actuators and pneumatic components. The actuator control board coordinates and synchronizes the movement of four Z-axis linear actuators based on real-time clamping force monitoring and feedback by a load cell (amplified by an HX711 module). Additionally, an HDMI-connected touchscreen functions as the primary user interface (like a robot teach pendant), displaying system status and allowing direct operator control.

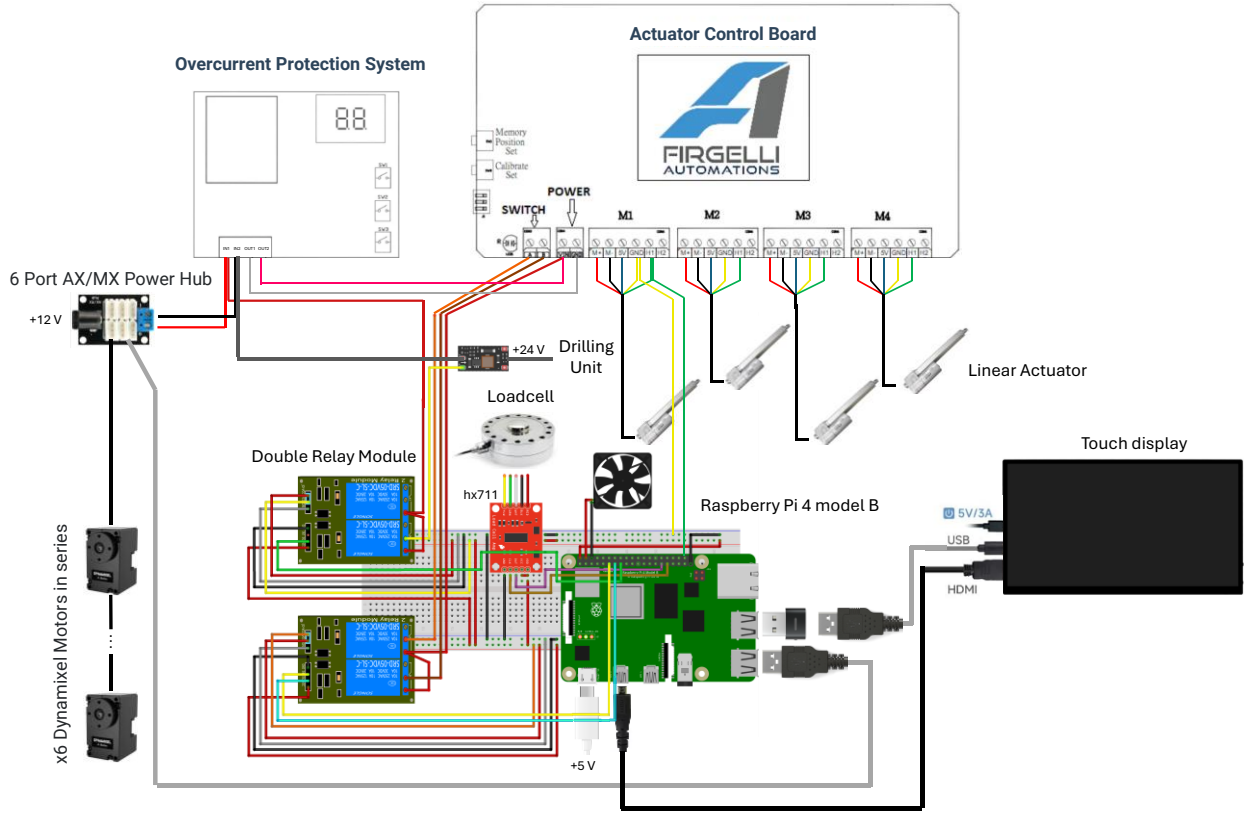

Figure 3-9 Electronics connections layout

The schematic in Figure 3-9 illustrates the hierarchical structure and connections of these components, showing power distribution, control systems, and sensor integration. The wiring strategy ensures that high-current actuation circuits remain isolated from low-power signal lines, reducing electromagnetic interference and improving system reliability. This integration of embedded computing, modular actuation, and real-time feedback enables ACME to maintain precise drilling operations while ensuring operator safety and system longevity.

3.5 Pneumatic System

Figure 3-10 shows the schematic of ACME's pneumatic components. This system employs a Venturi-based vacuum generator to create negative pressure using a 6-bar compressed air supply, enabling secure attachment to workpieces. Polyurethane suction cups (100–120 mm diameter) with integrated cleats adapt to curved surfaces while vacuum security valves prevent sudden detachment by blocking airflow if a seal is lost. Solenoid valves that regulate air supply to both the pneumatic drill motor and the Venturi generator, ensuring vacuum stability before drilling and allowing rapid venting for repositioning. This system enhances clamping reliability, compensating for the cobot's limited payload and ensuring consistent attachment of the device on the surface and safety during operation.

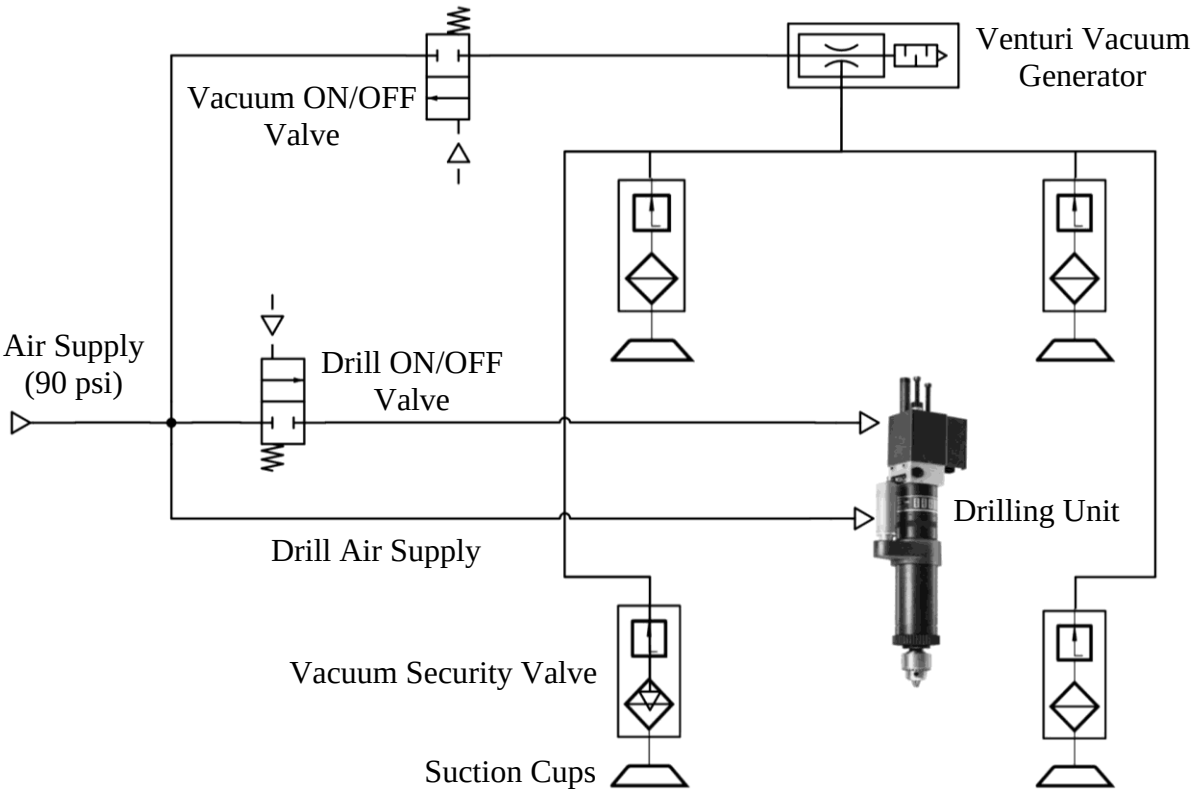

Figure 3-10, Schematic of the ACME pneumatic system

3.6 Task Sequence and Control

The operational logic of ACME is designed to facilitate reliable, repeatable, and fast drilling on aerospace components. To ensure process robustness and user safety, the task sequence is governed by a state-based control strategy that includes both automated and user-supervised steps. Figure 3-11 presents the flow chart of ACME's operation, beginning from system initialization to the completion of all designated drilling poses.

The sequence begins with initialization, where drilling poses, defined as (X, Y, Z, A, B) coordinates, are either uploaded via a graphical user interface (GUI) or imported from a predefined text file. These drilling poses specify the Cartesian position and orientation of the tool center point (TCP) required to achieve normality on the surface. Concurrently, ACME performs a homing routine to reset the actuators to their default positions, aligning the Z-axis upward and zeroing all prismatic and rotational axes. Following homing, the operator manually positions the ACME end-effector on the intended surface location using the cobot. Once the system is placed in approximate contact with the work surface, the suction system is activated, generating negative pressure to initiate clamping. Attachment confirmation is achieved through feedback from vacuum sensors and suction retention thresholds. If the attachment is unsuccessful (e.g., due to leakage or surface misalignment), the system prompts the operator to reposition and retry. Upon successful attachment, the system transitions into autonomous operation.

Each drilling task is indexed from i = 1 to N, where N represents the total number of poses. For each index, ACME moves to the corresponding drilling location and adjusts its TCP orientation to align with the desired surface normal. Once the pose is achieved, the Z-axis actuators drive the end-effector downward, pressing the device against the surface and building up clamping force. The real-time load cell monitors the generated force to ensure it exceeds the required threshold

(typically >700 N). Once the clamping force exceeds the specified threshold, the drilling operation is initiated. The drilling head is powered on via a solenoid-regulated pneumatic supply, and the auto-feed spindle begins the drilling process. A time-based or sensor-based logic is employed to determine the end of drilling, after which the Z-axis returns to its home position, releasing surface pressure. The loop then increments to the next pose, repeating the above steps until all N drilling positions have been processed. Once the final hole is completed, the system enters the termination state, returning the actuators to the home configuration and preparing for either shutdown or repositioning for a new task batch.

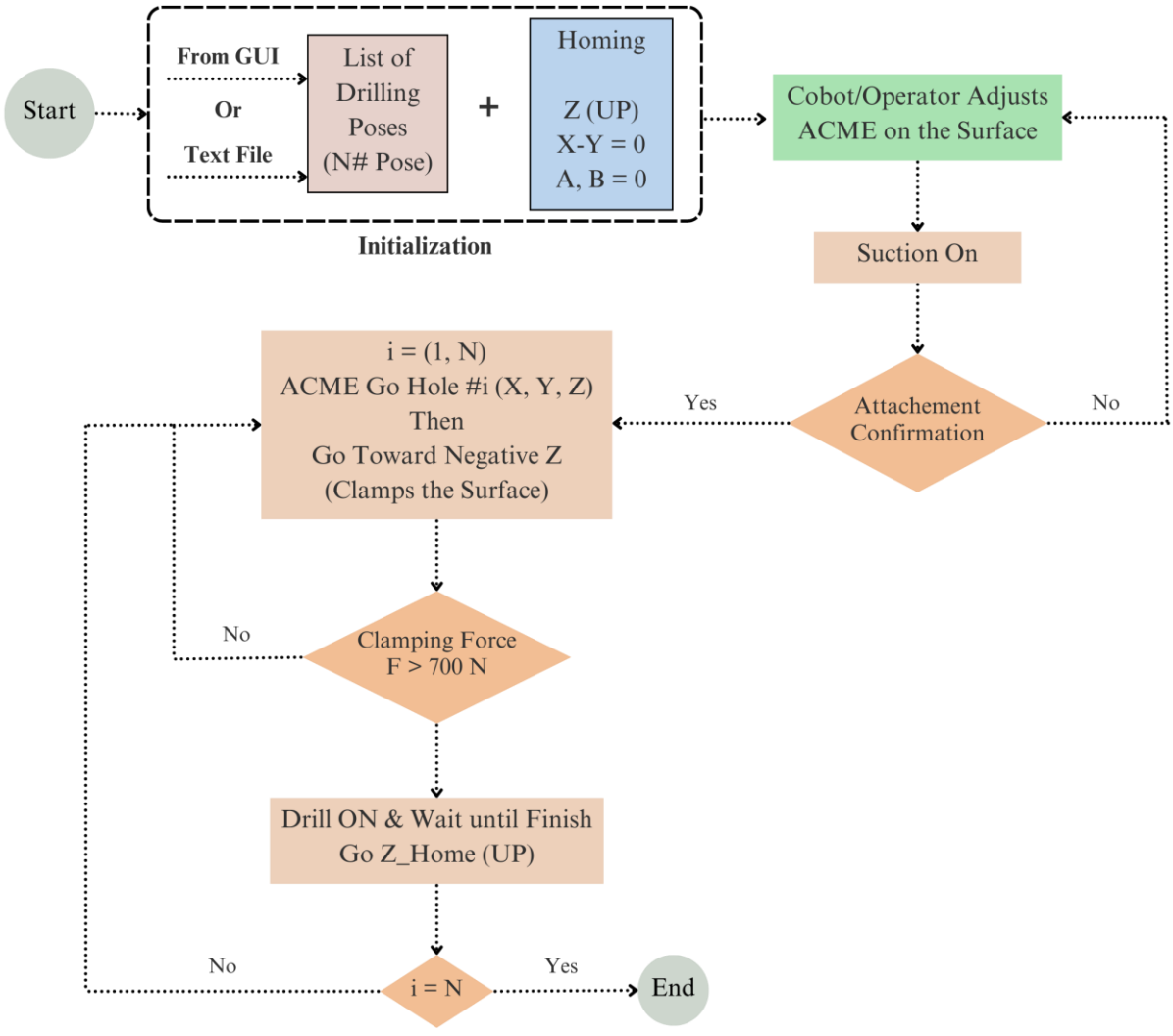

Figure 3-11, Flow chart explaining the task sequence and control for drilling using ACME

This flow-based control sequence ensures high process repeatability, modularity for multi-hole drilling operations, and safety through explicit operator confirmation stages and real-time sensor monitoring. The combination of manual placement and autonomous execution leverages the advantages of collaborative robots while overcoming their inherent limitations in payload and precision.

3.7 Experimental Verification of Performance and Functionality

To verify the performance and functional capabilities of the ACME, a series of experimental tests was conducted using a controlled testbed. These tests aimed to evaluate the system's structural integrity, operational efficiency, achievable workspace, and drilling quality under realistic conditions. The experiments were designed to assess whether the final prototype met the requirements detailed in Section 3.2, particularly in terms of clamping force capacity, drilling cycle duration, workspace coverage, and hole quality metrics.

The experimental setup, depicted in Figure 3-12, positions the ACME prototype horizontally on a flat metallic surface. Drilling instructions were programmed into the system via a graphical user interface (GUI), defining a matrix of target holes to be executed by the automated sequence. Upon initialization, ACME homed its actuators and carried out the drilling cycle autonomously across a predefined pattern.

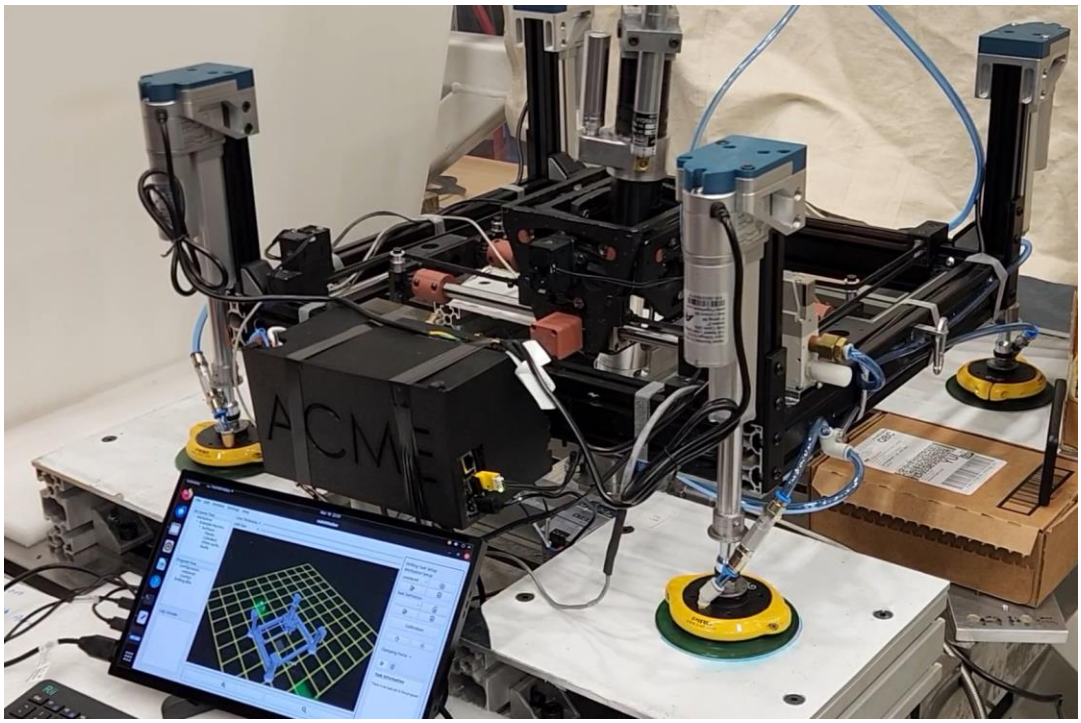

Figure 3-12 Overview of test setup for performance test

To determine the maximum clamping force achievable by the system, the Z-axis actuators were commanded to press the drilling frame against the test surface incrementally until the operator deemed that structural stress approached safe operational limits. Load cell data in Figure 3-13 revealed that the system successfully reached a clamping force of approximately 1000 N, thereby surpassing the design requirement of 700 N and demonstrating the structural integrity and robustness of the end-effector under load.

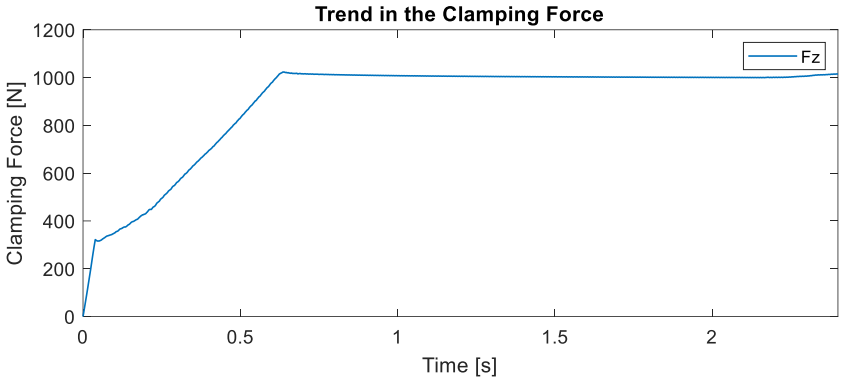

Figure 3-13, Built up of the clamping force reaches its optimal limit

Further performance characterization included measurement of drilling cycle times and actuation speeds. As shown in Figure 3-14, the plunge trajectory and feed velocity of the drilling unit were recorded during a typical operation. The positioning and clamping phases consumed approximately 7 seconds, and the drilling process itself required a minimum of 5 seconds to prevent jamming or bit deflection. Therefore, the complete cycle duration for one drilling pose was as short as 12 seconds under optimal conditions.

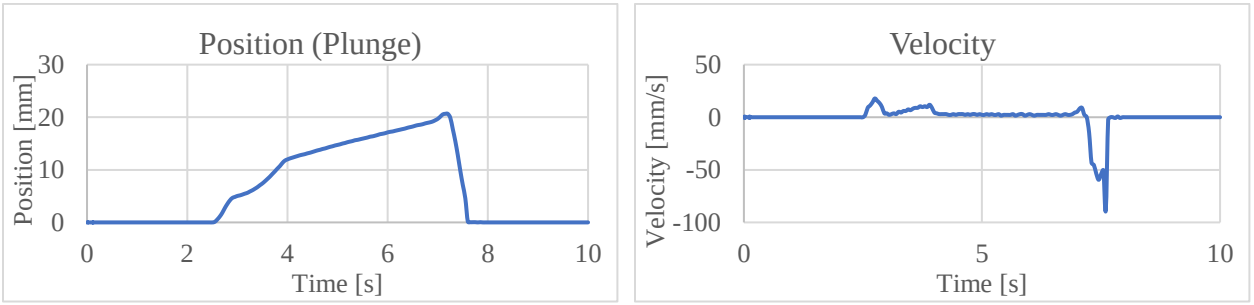

Figure 3-14, Position (plunge) and velocity diagrams of the ADU in one full cycle of drilling

Linear motion speeds of the individual actuators were also characterized during experimental runs. The CoreXY system enabled horizontal translation at a rate of up to 62 mm/s, while the Z-axis linear actuators achieved speeds ranging from 6 to 10 mm/s, depending on load and current settings. The drilling head, driven pneumatically, attained a maximum feed rate of 20 mm/s, which was suitable for the aluminum test material without exerting excessive forces on the drilling bit or causing tool wear.

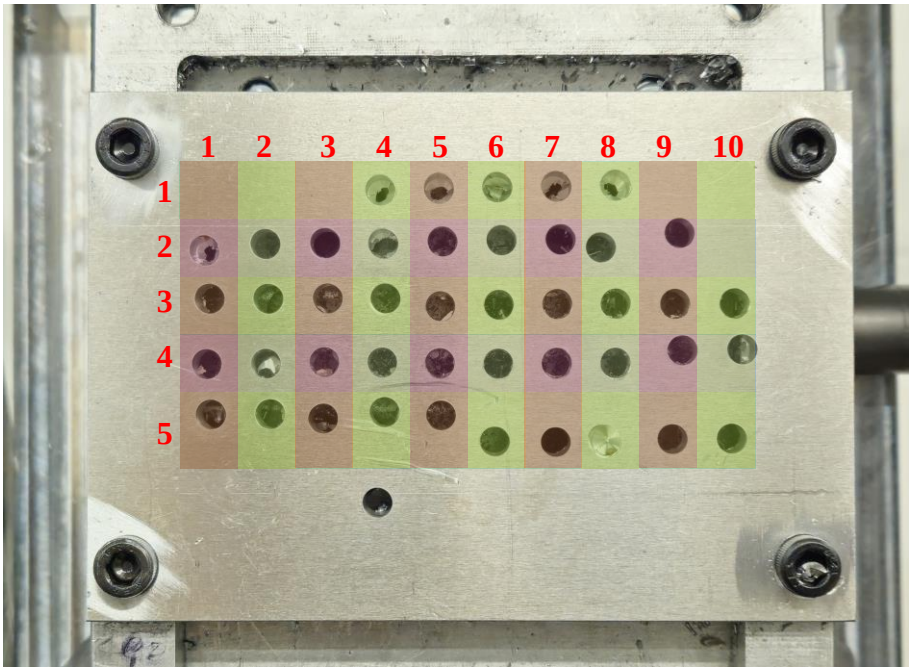

Figure 3-15, Pattern of holes drilled by ACME

Figure 3-15 illustrates the resulting pattern of drilled holes arranged in a 5×10 grid, which served as the testbed for assessing both operational consistency and hole quality. While the majority of holes were successfully executed, a subset near the fixture bolts failed due to insufficient space for proper nose placement or inadequate suction seal. Additional outliers were observed due to minor slippage during prolonged tests, leading to deviations from the original reference frame. Despite these issues, the overall pattern confirms the system's ability to execute multi-hole drilling sequences with acceptable consistency. To further evaluate the quality of holes produced by

ACME, the same aluminum stack was drilled using a CNC machine as a benchmark. Identical material (three sheets of 6061-T6, each 2.5 mm thick) and comparable process conditions were used. Post-drilling, five geometric quality metrics, cylinder diameter, normality error, roundness, concentricity, and circular run-out, were measured using a coordinate measurement machine (CMM), and the results are presented in Table 3-3. Although ACME exhibited slightly higher variability than the CNC reference, particularly in normality error and concentricity, the deviations remained within acceptable limits for the initial prototype. This outcome reflects the trade-off between portability and rigidity inherent to lightweight end-effectors, a limitation that can be mitigated through vibration control strategies discussed in Chapter 5.

Table 3-3, The comparison of the quality of drilling using ACME and CNC machines

Hole #	*Cylinder Diameter*	*Normality Error [deg]*	◯ *Cylinder Roundness*	⊙ *Concentricity*
	Reference (CNC Machine)			
Average	5.02844	0.9274	0.07612	0.155
	ACME			
Average	5.12880	2.661	0.17102	0.403

- Values are in [mm] unless otherwise written.
- ◯ **Roundness:** Roundness deviation is the distance between two concentric circles touching and enclosing the extracted circumferential line at the minimum radial distance to each other. The deviation must not exceed the tolerance value.
- ⊙ **Concentricity:** Concentricity deviation is the maximum radial distance between the calculated center and the datum element center. Twice this amount must not exceed the tolerance value.

ACME's reachable workspace was experimentally confirmed by extending the X, Y, and Z actuators to their mechanical limits while avoiding internal collisions. Figure 3-16 and Figure 3-17 present top and side views of the operational envelope. The measured workspace extends up to

approximately 302 mm in the X direction and 237 mm in the Y direction, resulting in a planar area sufficient for typical aerospace panel drilling operations without frequent repositioning. The Z-axis allows a vertical stroke of approximately 75 mm, accommodating minor variations in panel height. Recommended working limits were conservatively estimated as 267 mm × 202 mm in X–Y to ensure consistent suction seal and actuation reliability during extended operation.

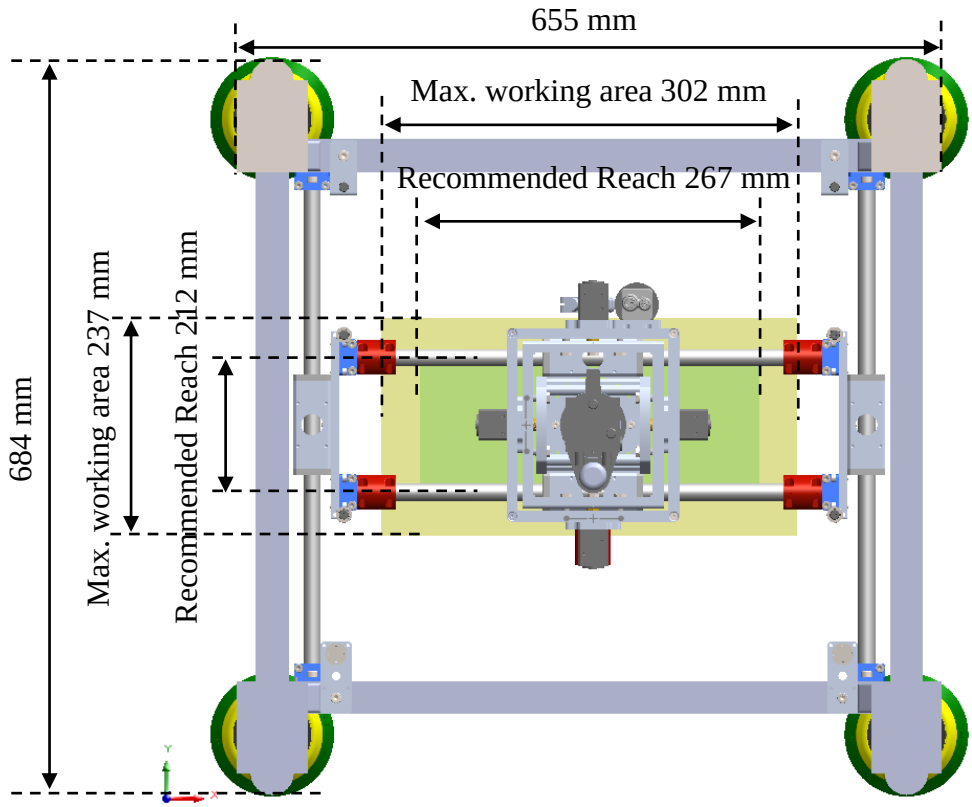

Figure 3-16, Top View: Horizontal workspace, including device dimensions and operational reach

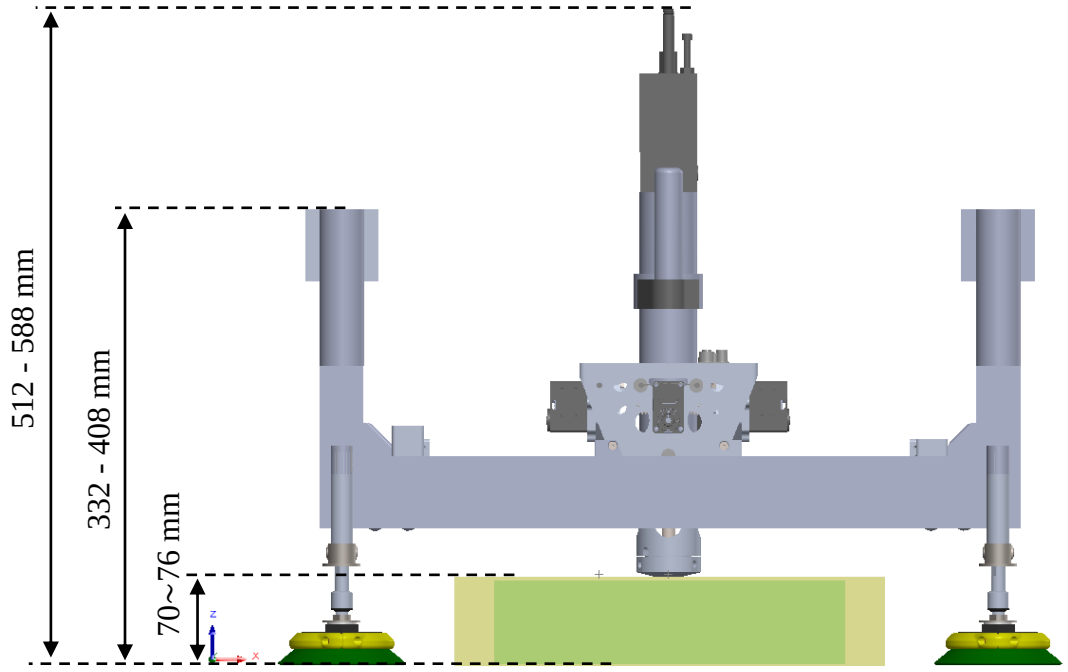

Figure 3-17, Side View: Vertical workspace with clearance, showcasing the Z-axis operational limits

A summary of ACME's verified specifications is presented in Table 3-4. The fully assembled system weighs approximately 18 kg, remaining within the payload limits of most high-end collaborative robots. The active workspace utilizes nearly half of the device's total footprint, maximizing space efficiency. Clamping forces of up to 1000 N were reliably achieved during repeated testing, while the actuators and sensors operated within a standard 12 V DC, 5 A electrical envelope. These results confirm that ACME meets or exceeds the key performance indicators initially outlined in Table 3-2, establishing it as a viable platform for collaborative aerospace drilling operations.

Table 3-4, Summary of general specification of ACME

Specification	***Value***	***Description***
Mass	~18 kg	Weight of the entire ACME unit (Including the drill unit)

Overall Dimensions (L × W × H)	~655 × 684 × 588 mm	Approximate bounding box when the ACME is fully retracted (home pose)
Maximum Workspace (L × W × H)	~302 × 237 × 76 mm	From Figure 3-16 and Figure 3-17. The X–Y carriage has 302 mm of travel per axis, and the Z stroke is ~76 mm
Optimal Workspace (L × W × H)	~267 × 212 × 76 mm	Recommended travel range for consistent performance
Maximum Useful Workspace (%)	~46% along X ~35% along Y	302 / 655 ≈ 46.1% along X and 237 / 684 ≈ 34.6% along Y, of the total device footprint is used as workspace
X-Y Axes Maximum Force	250 N (combined)	Force on the X–Y carriage system
X-Y Axes Maximum Speed	3.7 m/min	Translational speed of the CoreXY mechanism
A-B Axes Maximum Torque	58 N.m	Combined pitch (A) and yaw (B) axes torque around the drill axis
A-B Axes Maximum Speed	5.5 rev/min	Approximate rotation speed of the tilt axes
A-B Rotation Span	±10° each axis	Tilt range about the tool axis (home pose = 0°)
Z-Axis Typical Speed	~6–10 mm/s	Depending on the linear actuator model
Maximum Achievable Clamping Force	~1500–2360 N total	With four actuators at full extension
Maximum Optimal Clamping Force	1000 N	Recommended operating clamping load to ensure longevity and no suction cup detachment
Electrical Supply	12 V DC @ 5 A	Power input for linear actuators, electronics, actuators, relays, display, etc.
Air Pressure Supply	Min. 90 psi (620 kPa)	Required for the drilling unit and suction/vacuum generator
Operating Temperature Range	0–50 °C (nominal)	A typical recommended range for electronics and mechanical components.
Communications Interfaces	USB/TTL, GPIO	Dynamixel TTL bus, Raspberry Pi GPIO for load cell & actuator relays, USB for Pi console

- The *Maximum Achievable Clamping Force* can vary depending on actuator current limits, friction, and the suction cups' maximum hold. A safe, "optimal" clamping load of about 1000 N is recommended for normal operations.
- The listed dimensions reflect the prototype's measured/illustrated geometry in Figure 3-16 and Figure 3-17.
- "Repeatability" or "positioning resolution" (e.g., ±0.2 mm in X–Y) and accuracies can also be included in the specs. However, further tests or characterization are needed for accurate reporting.

3.8 Summary

This chapter presented the comprehensive design and prototyping process of the ACME (Advanced Collaborative Multifunctional End-Effector), developed to address the challenges associated with automated drilling on multi-layered, double-curvature surfaces commonly encountered in aerospace manufacturing. The design was guided by a set of stringent requirements, including high clamping force capacity (≥700 N), lightweight construction (<20 kg), the ability to maintain normality on curved surfaces, and compatibility with collaborative robotic platforms. These requirements were consolidated into a set of technical specifications that shaped the system architecture.

The resulting ACME prototype integrates three prismatic and two rotational degrees of freedom to facilitate planar motion and normality correction. A CoreXY-based mechanism was adopted for efficient and accurate X–Y positioning, while a passive self-normalizing drilling head mounted on a gimbal enables ±10° tilting to align the tool axis with the surface normal. Clamping is achieved through a combination of linear actuators and vacuum-assisted suction cups, providing surface attachment that decouples the end-effector’s operation from the robot's payload limitations. A through-hole load cell ensures real-time monitoring and control of the clamping force during the drilling cycle.

The system’s control architecture, based on a Raspberry Pi microcontroller, integrates sensor feedback, actuator coordination, and a user interface for semi-autonomous operation. A pneumatic system was employed to power the drilling unit and vacuum generation, and its sequence was managed using solenoid valves and sensor-based verification. The task logic was implemented as a state machine, incorporating initialization, pose indexing, force-controlled clamping, drilling, and reset routines to ensure safe and repeatable operation.

Experimental verification confirmed that the ACME prototype exceeded the specified clamping force and met workspace and cycle time targets. A maximum clamping force of 1000 N was reliably achieved, and the system was capable of completing one drilling cycle in approximately 12 seconds. The effective workspace measured 267 mm × 202 mm × 70 mm, suitable for common aerospace panel configurations. Hole quality metrics, assessed against a CNC-drilled reference, demonstrated acceptable precision in terms of diameter and roundness, although greater variability was observed in normality and concentricity due to structural compliance, an issue addressed through vibration modelling and control in subsequent chapters.

These results affirm that the developed prototype meets the critical functional and operational requirements of collaborative aerospace drilling. The design choices and verified performance provide a strong foundation for the kinematic, dynamic, and control modelling discussed in the following chapters.

4 ACME Kinematics and Dynamics Modelling

4.1 Introduction

Accurate modelling of the ACME end-effector's kinematics and dynamics is essential for achieving precise, repeatable, and high-quality drilling operations, particularly within aerospace manufacturing contexts where stringent tolerances are mandatory. Unlike conventional industrial robotic arms, which typically consist of serially connected revolute joints, the ACME drilling device integrates three prismatic (linear) degrees of freedom along the X, Y, and Z axes, combined with two rotational degrees of freedom (A and B). This hybrid configuration enables precise positioning and orientation adjustments required for maintaining normality during drilling operations on double-curvature aircraft panels. Given this distinct kinematic arrangement, developing accurate forward and inverse kinematic models becomes critical. These models must precisely define the positional and orientational relationships among the various prismatic and rotational joints, enabling accurate predictions of the end-effector pose for any given set of joint parameters. The kinematic modelling thus provides the foundation for motion planning, trajectory optimization, and precise control of the drilling process.

In parallel, establishing a comprehensive dynamic model is equally vital due to inherent structural flexibility in the joints and actuators, as well as inertia from moving assemblies. These factors contribute to dynamic behaviors such as vibrations, which, if not adequately addressed, can compromise drilling tolerances and overall precision. Hence, the dynamic model must capture both internal dynamic forces, such as inertia during rapid repositioning, and external disturbances, particularly the drilling thrust forces encountered during machining operations. Incorporating

experimentally identified stiffness and damping parameters for joints and attachment points ensures that the dynamic simulations accurately reflect real-world operational conditions.

A robust dynamic model supports further investigations into active vibration control methodologies (discussed in subsequent chapters), allowing the design and implementation of effective strategies to minimize vibrations such as process vibrations, which directly impact manufacturing quality.

The following sections in this chapter detail the kinematic and dynamic modelling processes: first defining the coordinate frames and associated Denavit-Hartenberg (DH) parameters for ACME's multi-degree-of-freedom arrangement, followed by derivations and verifications of the forward and inverse kinematics, and concluding with the formulation and verification of the dynamic relationships governing ACME's motion under operational drilling loads.

4.2 Frames and DH Parameters

This section introduces the modified Denavit-Hartenberg (DH) parameters for the serial kinematic chain of the ACME. Denavit-Hartenberg parameters, initially proposed by Denavit and Hartenberg (1955), provide a systematic approach to describing the geometric configuration of serial-chain robotic manipulators. These parameters have become widely accepted for performing standard kinematic analyses of robotic arms, as described by Craig (2005). Craig's convention, commonly referred to as "modified DH parameters," differs from the original "standard" interpretation by Paul. The primary advantage of the modified DH parameters is that each coordinate frame aligns directly at its respective joint rather than being located remotely, as in Paul's standard approach.

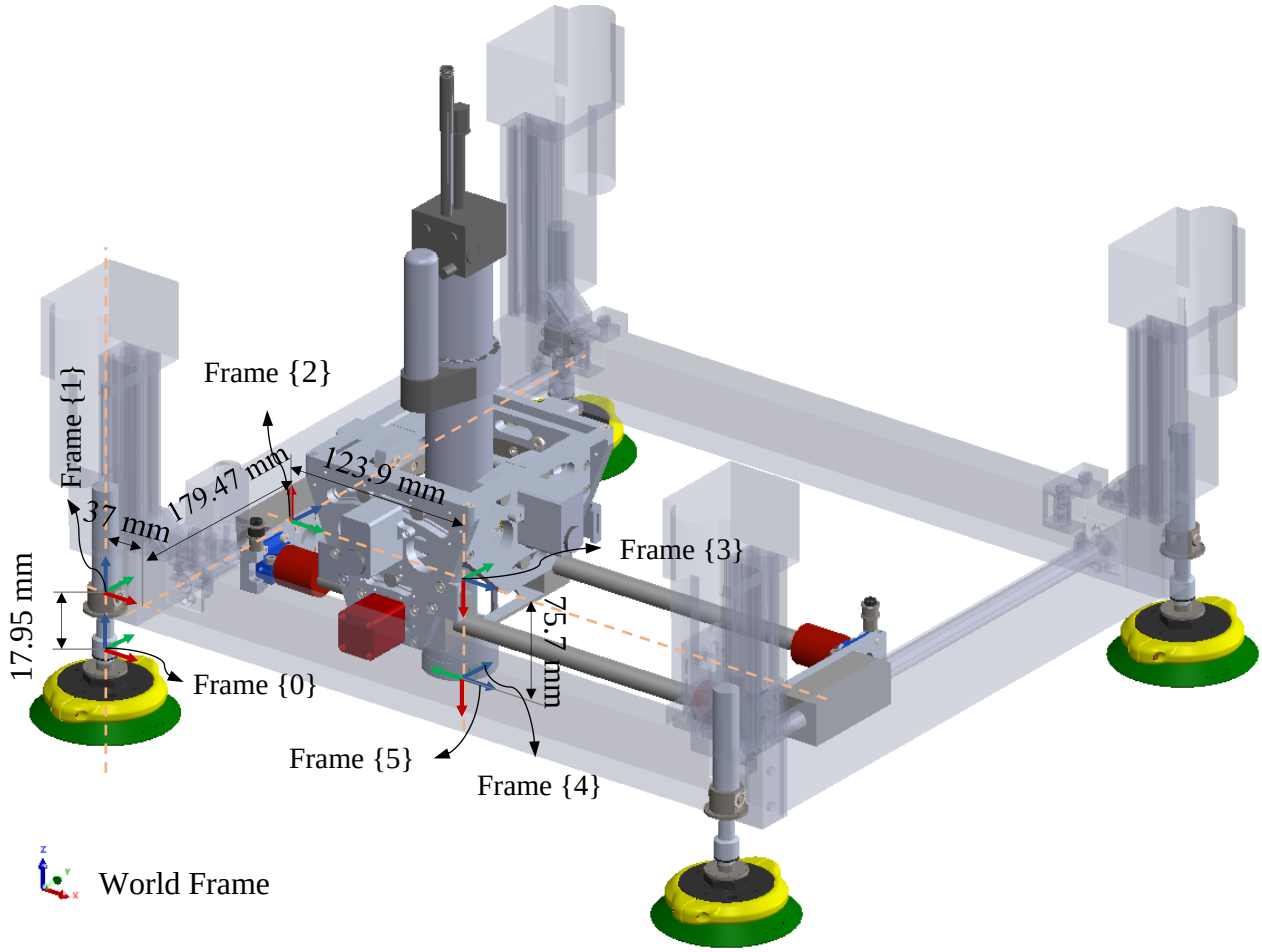

Figure 4-1, The Cartesian coordinate frames definitions for ACME 5-DoF are shown, which give the associated DH parameters

The DH parameters adopted for ACME are based on the approach outlined in [23], which defines spatial relationships between sequential joints. Four parameters characterize each link of the robot:

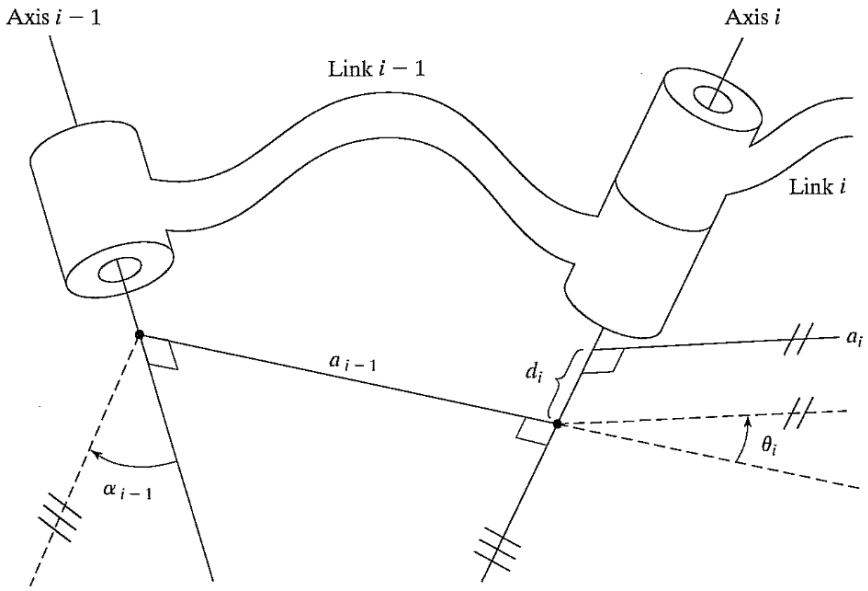

Figure 4-2, Spatial relationships of two consecutive joints in space [23]

a (length): The link length. This is the distance along the x-axis between two consecutive joints.

d (offset): The link offset. It represents the distance along the z-axis from one link to the next.

α (alpha): The link twist. It describes the angle between two consecutive z-axes along the x-axis.

θ (theta): The joint angle. It defines the rotation around the z-axis between two consecutive coordinate frames.

Table 4-1, 5-DoF ACME DH Parameters

	J1 (Z-Axis)	*J2 (Y-Axis)*	*J3 (X-Axis)*	*J4 (B-Axis)*	*J5 (A-Axis)*
a [mm]	0	37	0	75.7	0
d [mm]	$\boldsymbol{d_1}$ + 17.95	$\boldsymbol{d_2}$ + 179.47	$\boldsymbol{d_3}$ + 123.9	0	0
α [rad]	0	-pi/2	-pi/2	-pi/2	pi/2
θ [rad]	0	-pi/2	pi	$\boldsymbol{\theta_4}$ (B) – pi/2	$\boldsymbol{\theta_5}$ (A) + pi/2

For clarity regarding the coordinate frames and associated links, refer to Figure 4-1. Frame {0} is positioned at the midpoint of the ball joints, situated between the suction cup and the linear actuator's end. Specifically, Frame {0} aligns with the ball joint nearest to Dynamixel motor #5.

Frame $\{1\}$ and its corresponding displacement (d_1) represent the vertical (Z-axis) translation. Frames $\{2\}$ and $\{3\}$ correspond to the motion of the Y and Z carriages, respectively. Lastly, Frames $\{4\}$ and $\{5\}$ define the B and A rotational joints, located at the tip of the drilling nose, precisely at the interface with the drilling surface.

4.3 ACME Kinematics Modelling

Kinematic modelling provides a fundamental understanding of robot motion by defining geometric relationships independent of time. For the ACME drilling end-effector, kinematic analysis establishes the relationship between joint parameters, including linear displacements and rotational angles, and the resulting position and orientation of the tool center point (TCP) relative to a defined reference frame. The principal aim of kinematic modelling is thus to derive mathematical expressions capable of predicting the spatial configuration of the TCP based solely on the joint variables of the robotic mechanism. Kinematic analysis is generally classified into two interconnected yet distinct problems:

Forward Pose Kinematics (FPK): This approach calculates the end-effector's position and orientation from known joint parameters (linear extensions and angular rotations). Essentially, given specific joint variables, the objective is to determine precisely where the TCP is located and how it is oriented within the world coordinate frame.

Inverse Pose Kinematics (IPK): Conversely, this analysis solves the reverse problem. Given a desired spatial configuration (position and orientation) of the TCP, inverse kinematics computes the joint parameters necessary to achieve that particular end-effector pose. In robotic drilling applications, IPK is particularly crucial for accurately guiding the tool along planned trajectories or specific drill locations.

In the following subsections, the detailed derivations and verifications for both forward and inverse pose kinematics models of the ACME robotic system are presented. These analyses provide mathematical foundations essential for subsequent dynamic modelling, trajectory planning, and precise control of drilling operations.

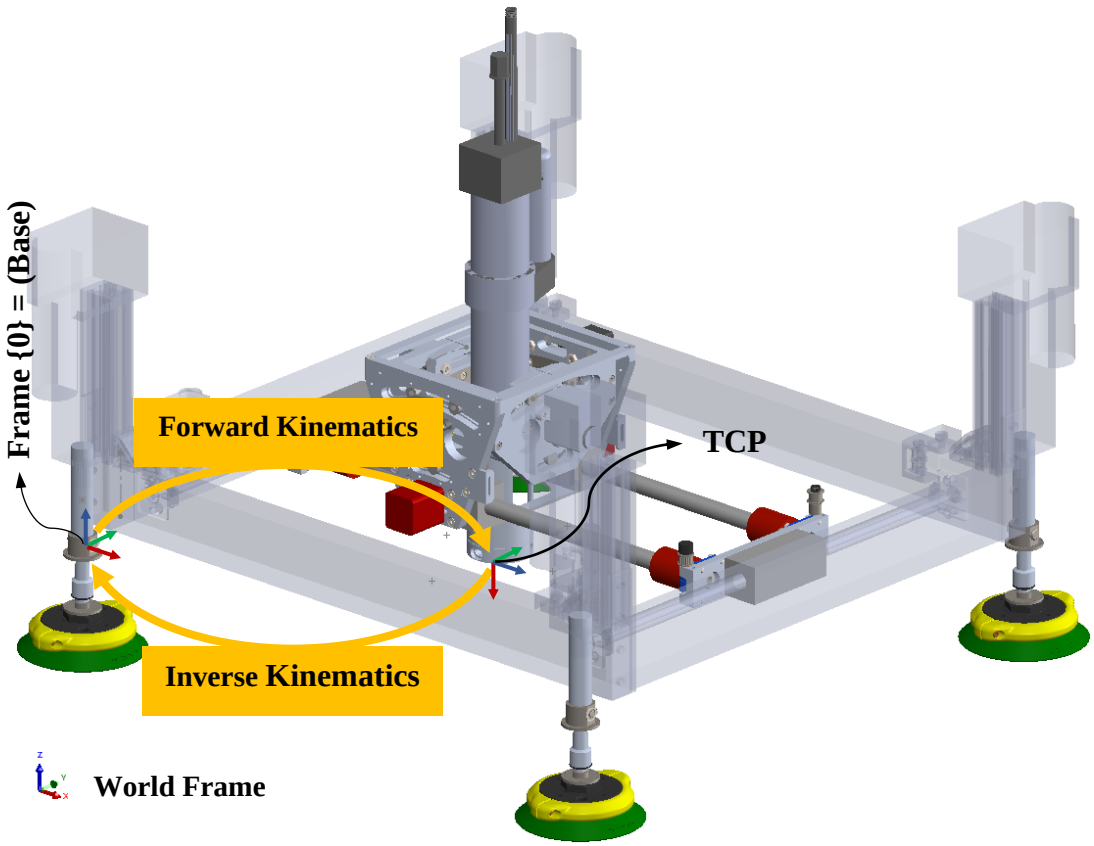

Figure 4-3, Forward and inverse kinematics relating the joint and world space

4.3.1 ACME Forward Pose Kinematics (FPK)

The Forward Pose Kinematics (FPK) of a serial robotic manipulator involves determining the spatial configuration, specifically, the position and orientation, of the end-effector given a set of known joint parameters. In serial-chain robotic systems, solving the FPK is typically straightforward and systematic. It involves using the established Denavit-Hartenberg (DH) parameters (provided earlier in Table 4-1) to describe each link in the robot's serial structure.

The general solution process relies on sequentially substituting the DH parameters for each joint into the homogeneous transformation matrix formulation. Specifically, the transformation from one frame $\{i-1\}$ to the next adjacent frame $\{i\}$ is calculated using the following standard equation (Craig, 2005):

$$\left[{}_{i}^{i-1}T\right] = \begin{bmatrix} c\theta_i & -s\theta_i & 0 & a_{i-1} \\ s\theta_i c\alpha_{i-1} & c\theta_i c\alpha_{i-1} & -s\alpha_{i-1} & -d_i s\alpha_{i-1} \\ s\theta_i s\alpha_{i-1} & c\theta_i s\alpha_{i-1} & c\alpha_{i-1} & d_i c\alpha_{i-1} \\ 0 & 0 & 0 & 1 \end{bmatrix} = \begin{bmatrix} & \left[{}_{i}^{i-1}R\right] & & \left\{{}^{i-1}P_i\right\} \\ 0 & 0 & 0 & 1 \end{bmatrix} \quad (4.1)$$

Where the following abbreviations were used: $c\theta_i = \cos\theta_i$, $s\theta_i = \sin\theta_i$, $c\alpha_i = \cos\alpha_i$, and $s\alpha_i = \sin\alpha_i$.

This homogeneous transformation matrix systematically defines both the geometric and kinematic relationships between consecutive coordinate frames. Specifically, it provides the fundamental building block needed to derive the complete transformation from the robot's base reference frame to the tool center point (TCP).

The homogeneous transformation matrix shown above expresses the pose (position and orientation) of frame $\{i\}$ with respect to frame $\{i-1\}$. The upper-left 3×3 submatrix, denoted as $\left[{}_{i}^{i-1}R\right]$ represents the orientation of frame $\{i\}$ with respect to frame $\{i-1\}$, expressed in frame $\{\ i-1\ \}$'s coordinates. The upper-right 3×1 vector $\left\{{}^{i-1}P_i\right\}$ describes the translational displacement, or position vector, from the origin of frame $\{i-1\}$ to the origin of $\{i\}$, likewise expressed in $\{i-1\}$ coordinates.

By multiplying these sequential transformation matrices throughout the entire kinematic chain, the final pose of the robot's end-effector frame with respect to the fixed base reference frame can be determined. This procedure completes the forward pose kinematics (FPK) analysis for any given serial-chain robotic system.

Formally, the forward kinematics problem for the ACME end-effector, which features a 5-degree-of-freedom (5-DoF) serial-chain arrangement, can be described as follows:

Given a set of known joint variables $(d_1, d_2, d_3, \theta_4, \theta_5)$ the objective is to compute the transformation matrices $[{}^0_5T]\ and\ [{}^B_{TCP}T]$ where:

- (d_1, d_2, d_3) represent linear joint displacements along the prismatic axes, and (θ_4, θ_5) correspond to rotational joint angles.
- $\{TCP\}$denotes the tool center point reference frame, and $\{B\}$signifies the stationary base frame of the robot (illustrated in Figure 4-3).
- The coordinate frames are defined following a right-handed Cartesian coordinate system, indicated by curly brackets { }. The ACME mechanism comprises a total of six defined frames labelled {0}, {1}, … {5}. Here, frame {0} is fixed, serving as the base frame, while frames {1} through {5} are movable frames, each associated with a specific active joint.

To obtain the forward kinematic solution for ACME, each set of Denavit-Hartenberg parameters from Table 4-1 is systematically substituted into the general homogeneous transformation equation (Eq. (4.1)). This yields five consecutive transformation matrices, each expressed explicitly in terms of the respective joint variables, fully characterizing the spatial configuration of the ACME end-effector.

$$[{}^0_1T] = \begin{bmatrix} 1 & 0 & 0 & 0 \\ 0 & 1 & 0 & 0 \\ 0 & 0 & 1 & d_1 + 17.95 \\ 0 & 0 & 0 & 1 \end{bmatrix}, [{}^1_2T] = \begin{bmatrix} 0 & 1 & 0 & 37 \\ 0 & 0 & 1 & d_2 + 179.47 \\ 1 & 0 & 0 & 0 \\ 0 & 0 & 0 & 1 \end{bmatrix}$$

$$[{}^2_3T] = \begin{bmatrix} -1 & 0 & 0 & 0 \\ 0 & 0 & 1 & d_3 + 123.9 \\ 0 & 1 & 0 & 0 \\ 0 & 0 & 0 & 1 \end{bmatrix}, [{}^3_4T] = \begin{bmatrix} \cos(\theta_4 - pi/2) & -\sin(\theta_4 - pi/2) & 0 & 75.7 \\ 0 & 0 & 1 & 0 \\ -\sin(\theta_4 - pi/2) & -\cos(\theta_4 - pi/2) & 0 & 0 \\ 0 & 0 & 0 & 1 \end{bmatrix} (4.2)$$

$$[{}^4_5T] = \begin{bmatrix} \cos(\theta_5 + pi/2) & -\sin(\theta_5 + pi/2) & 0 & 0 \\ 0 & 0 & -1 & 0 \\ \sin(\theta_5 + pi/2) & \cos(\theta_5 + pi/2) & 0 & 0 \\ 0 & 0 & 0 & 1 \end{bmatrix}$$

The forward pose kinematics (FPK) solution for the ACME end-effector is derived by sequential multiplication of homogeneous transformation matrices, each corresponding to individual joint variables.

$$[{}^0_5T(d_1, d_2, d_3, \theta_4, \theta_5)] = [{}^0_1T(d_1)]\,[{}^1_2T(d_2)]\,[{}^2_3T(d_3)]\,[{}^3_4T(\theta_4)]\,[{}^0_1T(\theta_5)] \tag{4.3}$$

$$[{}^0_5T(d_1, d_2, d_3, \theta_4, \theta_5)] = \begin{bmatrix} -c_4 s_5 & -c_4 c_5 & s_4 & d_3 + 160.9 \\ c_5 & -s_5 & 0 & d_2 + 179.47 \\ s_4 s_5 & c_5 s_4 & c_4 & d_1 - 57.75 \\ 0 & 0 & 0 & 1 \end{bmatrix} \tag{4.4}$$

Where the following shorthand notations are introduced for convenience and clarity: $c_i = \cos\theta_i$, $s_i = \sin\theta_i$ for $i = 4, 5$.

Considering the ACME structure, frames {2} and {3} correspond to the planar CoreXY mechanism, while frames {4} and {5} correspond to the rotational joints (A and B axes) located at the pivotal point on the drilling nose. Given these structural characteristics, the full FPK transformation from the base frame to the end-effector is grouped logically as follows:

$${}^0_5T(d_1, d_2, d_3, \theta_4, \theta_5) = {}^0_1T(d_1)\ {}^1_3T(d_2, d_3)\ {}^3_5T(\theta_4, \theta_5) \tag{4.5}$$

In this expression, $[{}^0_1T(d_1)]$ was previously defined, while ${}^1_3T(d_2, d_3)$ and ${}^3_5T(\theta_4, \theta_5)$ are obtained through sequential matrix multiplication and subsequent algebraic simplifications.

$$[{}^1_3T(d_2, d_3)] = \begin{bmatrix} 0 & 0 & 1 & d_3 + 160.9 \\ 0 & 1 & 0 & d_2 + 179.47 \\ -1 & 0 & 0 & 0 \\ 0 & 0 & 0 & 1 \end{bmatrix}, [{}^3_5T(\theta_4, \theta_5)] = \begin{bmatrix} -s_4 s_5 & -c_5 s_4 & -c_4 & 75.7 \\ c_5 & -s_5 & 0 & 0 \\ -c_4 s_5 & -c_4 c_5 & s_4 & 0 \\ 0 & 0 & 0 & 1 \end{bmatrix} \tag{4.6}$$

This separation serves a practical purpose; it isolates the transformation matrix ${}^1_3T(d_2, d_3)$ directly representing the CoreXY planar kinematic subsystem. This arrangement allows targeted analysis

and integration of the specialized kinematic equations governing CoreXY-based linear motion, facilitating a clearer understanding and more precise control of the end-effector movements.

CoreXY Kinematic Equations

The X-Y motion of ACME is based on the CoreXY mechanism (detailed previously in Chapter 3). From a kinematic perspective, this mechanism couples the linear displacements of two independently actuated motors to achieve precise planar movements.

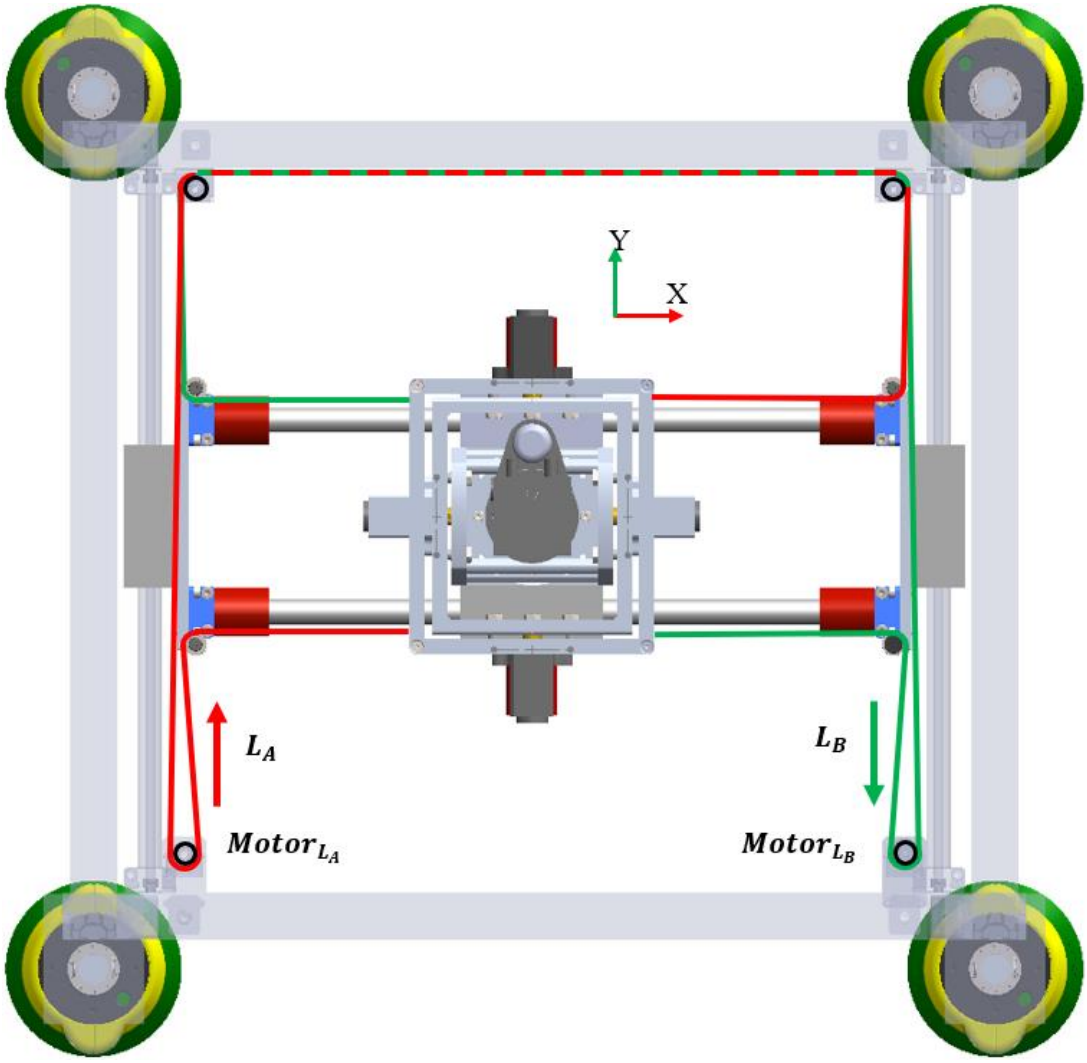

Figure 4-4, Configuration of CoreXY mechanism in ACME structure

The resulting displacement of the end-effector in Cartesian coordinates, described by joint variables d_3 (X-axis) and d_2 (Y-axis), is given by:

$$d_3 = X = 1/2\ (L_A\ +\ L_B) \tag{4.7}$$

$$d_2 = Y = 1/2\ (L_B\ -\ L_A) \tag{4.8}$$

Where L_A and L_B represent the respective linear displacements of Motors A and B. Conversely, when given desired Cartesian coordinates for the tool center point (TCP), the required motor displacements can be derived as follows:

$$L_A = -X + Y = -d_3 + d_2 \tag{4.9}$$

$$L_B = X + Y = d_3 + d_2 \tag{4.10}$$

Thus, the transformation matrix $[{}^1_3T(L_A, L_B)]$, representing the CoreXY-driven planar displacement, can be expressed explicitly in terms of motor displacements L_A and L_B:

$$[{}^1_3T(L_A, L_B)] = \begin{bmatrix} 0 & 0 & 1 & \frac{1}{2}(L_A\ +\ L_B) + 160.9 \\ 0 & 1 & 0 & \frac{1}{2}(L_B\ -\ L_A) + 179.47 \\ -1 & 0 & 0 & 0 \\ 0 & 0 & 0 & 1 \end{bmatrix} \tag{4.11}$$

With ${}^1_3T(L_A, L_B)$ now defined, the complete forward kinematics solution, ${}^0_5T$, is obtained by performing successive matrix multiplications:

$${}^0_5T = {}^0_1T(d_1)\ {}^1_3T(L_A, L_B)\ {}^3_5T(\theta_4, \theta_5) \tag{4.12}$$

$$[{}^0_5T(d_1, L_A, L_B, \theta_4, \theta_5)] = \begin{bmatrix} r_{11} & r_{12} & r_{13} & {}^0x_5 \\ r_{21} & r_{22} & r_{23} & {}^0y_5 \\ r_{31} & r_{32} & r_{33} & {}^0z_5 \\ 0 & 0 & 0 & 1 \end{bmatrix}$$

$$= \begin{bmatrix} -c_4 s_5 & -c_4 c_5 & s_4 & \frac{1}{2}(L_A + L_B) + 160.9 \\ c_5 & -s_5 & 0 & \frac{1}{2}(L_B - L_A) + 179.47 \\ s_4 s_5 & c_5 s_4 & c_4 & d_1 - 57.75 \\ 0 & 0 & 0 & 1 \end{bmatrix} \quad (4.13)$$

From this resulting matrix, the rotation and position components can be extracted separately. The rotation matrix elements, defining the orientation of frame {5} with respect to the base frame {0}, are:

$${}^0_5R(\theta_4, \theta_5) = {}^0_1R\ {}^1_3R\ {}^3_5R(\theta_4, \theta_5) = \begin{bmatrix} r_{11} & r_{12} & r_{13} \\ r_{21} & r_{22} & r_{23} \\ r_{31} & r_{32} & r_{33} \end{bmatrix} \quad (4.14)$$

The orthonormal rotation matrix elements for this FPK result are:

$$\begin{aligned} r_{11} &= -c_4 s_5 \\ r_{21} &= c_5 \\ r_{31} &= s_4 s_5 \\ r_{12} &= -c_4 c_5 \\ r_{22} &= -s_5 \\ r_{32} &= c_5 s_4 \\ r_{13} &= s_4 \\ r_{23} &= 0 \\ r_{33} &= c_4 \end{aligned} \quad (4.15)$$

The translational components of the FPK solution, which represent the coordinates of the origin of frame {5} with respect to frame {0}, are expressed by the following position vector:

$${}^0_5P(d_1, L_A, L_B) = {}^0_1R\ {}^1_3P(L_A, L_B) + {}^0_1P(d_1) = \begin{Bmatrix} {}^0x_5 \\ {}^0y_5 \\ {}^0z_5 \end{Bmatrix} \quad (4.16)$$

The translational matrix elements for this FPK result are:

$$^{0}x_5 = \frac{1}{2}(L_A + L_B) + 160.9 \tag{4.17}$$

$$^{0}y_5 = \frac{1}{2}(L_B - L_A) + 179.47 \tag{4.18}$$

$$^{0}z_5 = d_1 - 57.75 \tag{4.19}$$

Since frames {4} and {5} share a common origin at the drilling nose (TCP), the position components are solely functions of the prismatic joint variables (d_1, L_A, L_B), whereas the rotation matrix elements depend exclusively on the rotational joint angles (θ_4, θ_5). This clear separation significantly simplifies the inverse pose kinematics (IPK) analysis presented in the following sections.

Additional Fixed Transformations - TCP and Base Frames

To finalize the forward pose kinematics (FPK) solution and establish the transformation from the robot base frame {B} to the tool center point (TCP) frame {TCP}, two additional fixed transformations are required:

$$[{}^{B}_{TCP}T] = [{}^{B}_{0}T][{}^{0}_{5}T(d_1, L_A, L_B, \theta_4, \theta_5)][{}^{5}_{TCP}T] \tag{4.20}$$

These transformations ($^{B}_{0}T$ and $^{5}_{TCP}T$) are fixed and do not correspond to any joint variable; hence, they are not derived from the DH parameter table. Instead, they are determined through direct inspection based on the chosen locations and orientations of the base and the TCP frames.

For ACME, the base frame ({B}) coincides exactly with frame {0}, and the TCP frame aligns with the endpoint of the final rotational joint (frame {5}). As such, both fixed transformations are identity matrices, simplifying the overall kinematic expression:

$$[{}^{B}_{0}T] = \begin{bmatrix} 1 & 0 & 0 & 0 \\ 0 & 1 & 0 & 0 \\ 0 & 0 & 1 & 0 \\ 0 & 0 & 0 & 1 \end{bmatrix}, \qquad [{}^{5}_{TCP}T] = \begin{bmatrix} 1 & 0 & 0 & 0 \\ 0 & 1 & 0 & 0 \\ 0 & 0 & 1 & 0 \\ 0 & 0 & 0 & 1 \end{bmatrix} \tag{4.21}$$

$$[{}^{B}_{TCP}T] = [{}^{0}_{5}T] \tag{4.22}$$

This simplification results from strategic frame placement, which streamlines calculations for both forward and inverse kinematics solutions.

4.3.2 Verification of the FPK

To verify the accuracy and reliability of the developed FPK model for the ACME system, three distinct kinematic verification scenarios were studied:

1. **Zero Joint Angles Scenario:** All joint parameters were set to zero, providing a clear baseline for verification.
2. **General Pose Scenario:** Arbitrary nonzero joint parameters were chosen to demonstrate the kinematic solution under typical operational conditions.
3. **Home Pose Scenario:** Joint parameters corresponding to the defined "home" position of the ACME robot were examined to ensure correct model alignment.

Each scenario was simulated in MATLAB Simulink, enabling a visual representation of the ACME system's poses. These simulations provided a practical verification of the computed forward kinematics results, verifying the consistency and correctness of the transformation equations across various joint configurations.

In addition to these static verifications, a dynamic FPK trajectory analysis was conducted. This simulation illustrated how the tool center point (TCP) position and orientation evolved through

steps under continuous joint movements, further confirming the integrity and accuracy of the forward kinematic equations. All positional displacements were consistently presented in meters for clarity. Following MATLAB simulation results and visual snapshots for the three verification cases and the subsequent dynamic trajectory example are presented.

Examples #1

Given zero joint values: $\{d_1, L_A, L_B, \theta_4, \theta_5\} = \{0, 0, 0, 0, 0\}$

The FPK result: $[{}^0_5T] = \begin{bmatrix} 0 & -1 & 0 & 0.1609 \\ 1 & 0 & 0 & 0.1795 \\ 0 & 0 & 1 & -0.0577 \\ 0 & 0 & 0 & 1 \end{bmatrix}$

Simulation result: $[{}^0_5T] = \begin{bmatrix} 0 & -1 & 0 & 0.160900 \\ 1 & 0 & 0 & 0.179405 \\ 0 & 0 & 1 & -0.057595 \\ 0 & 0 & 0 & 1 \end{bmatrix}$

Examples #2

Given general joint values: $\{d_1, L_A, L_B, \theta_4, \theta_5\} = \{0.02, -0.02, 0.094, 5, -5\}$

The FPK result: $[{}^0_5T] = \begin{bmatrix} -0.2720 & -0.0805 & -0.9589 & 0.1979 \\ 0.2837 & -0.9589 & 0.0000 & 0.2365 \\ -0.9195 & -0.2720 & 0.2837 & -0.0377 \\ 0 & 0 & 0 & 1 \end{bmatrix}$

Simulation result: $[{}^0_5T] = \begin{bmatrix} -0.2720 & -0.0805 & -0.9589 & 0.197913 \\ 0.2837 & -0.9589 & 0.0000 & 0.236405 \\ -0.9195 & -0.2720 & 0.2837 & -0.037596 \\ 0 & 0 & 0 & 1 \end{bmatrix}$

Examples #3

Given the Home joint values: $\{d_1, L_A, L_B, \theta_4, \theta_5\} = \{0.076, 0.0275, 0.2395, 0, 0\}$

The FPK result: $[{}^0_5T] = \begin{bmatrix} 0 & -1 & 0 & 0.2944 \\ 1 & 0 & 0 & 0.2855 \\ 0 & 0 & 1 & 0.0183 \\ 0 & 0 & 0 & 1 \end{bmatrix}$

Simulation result: $[{}^{0}_{5}T] = \begin{bmatrix} 0 & -1 & 0 & 0.294400 \\ 1 & 0 & 0 & 0.285405 \\ 0 & 0 & 1 & 0.018405 \\ 0 & 0 & 0 & 1 \end{bmatrix}$

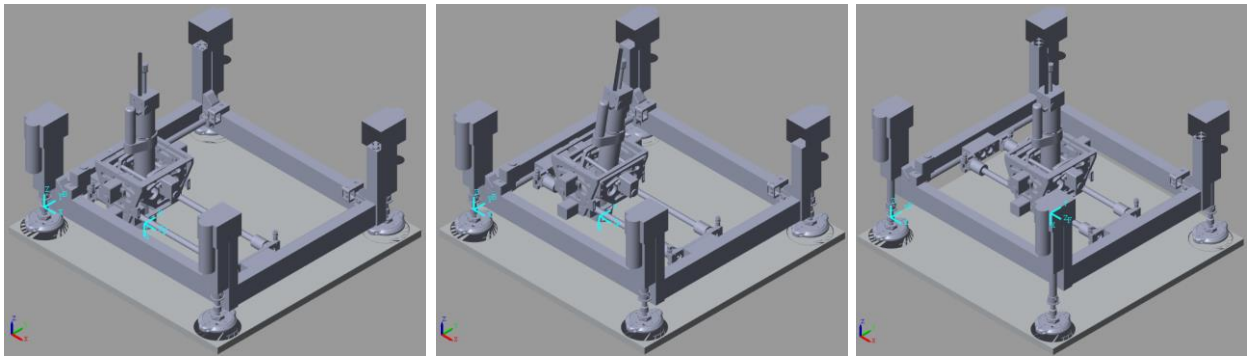

Example #1 *Example #2* *Example #3*

Figure 4-5, TCP pose in the simulation environment for each FPK example

The verification of the Forward Pose Kinematics (FPK) model for the ACME robotic system was successfully carried out using all three previously defined scenarios. In each scenario, the numerical results obtained from the simulation were found to be consistent with the derived symbolic solution for $[{}^{0}_{5}T]$, confirming the accuracy of the developed kinematic equations. Specifically, for the Zero Joint Angles and Home Pose cases (Examples 1 and 3), an additional verification step involving direct geometric inspection confirmed that the calculated Cartesian positions and orientations of the Tool Center Point (TCP) frame relative to the base frame {B} precisely matched expectations.

All joints' motion simulation

To further evaluate the model under realistic motion conditions, a synchronized linear trajectory simulation was conducted. Figure 4-6 illustrates the resulting joint trajectories over 100 incremental simulation steps, in which the prismatic joints move uniformly from their minimum (initial) positions to their maximum allowable displacements. Concurrently, the revolute joints were rotated through their complete operational range, specifically from -10° to $+10^{\circ}$. This

visualization clearly demonstrates the sequential and synchronized motion profiles for each joint throughout the simulation period.

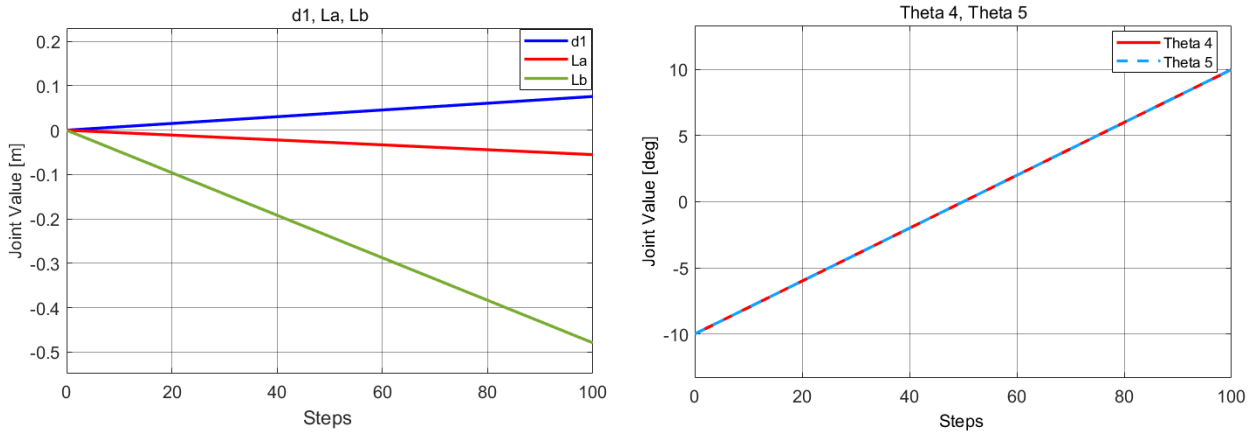

Figure 4-6, Joint value by steps [0-100]

Subsequently, Figure 4-7 shows the resulting Tool Center Point (TCP) pose evolution across the same simulation steps (0–100). In this analysis, the TCP's positional coordinates and orientation, expressed through Euler angles (α,β,γ), were tracked with reference to the ACME base coordinate frame. The TCP trajectory data aligns closely with the anticipated operational workspace, confirming the validity and reliability of the FPK model. These outcomes provide a comprehensive understanding of the ACME system's expected behaviour, offering valuable insights into its positional accuracy and orientational consistency during typical operational scenarios.

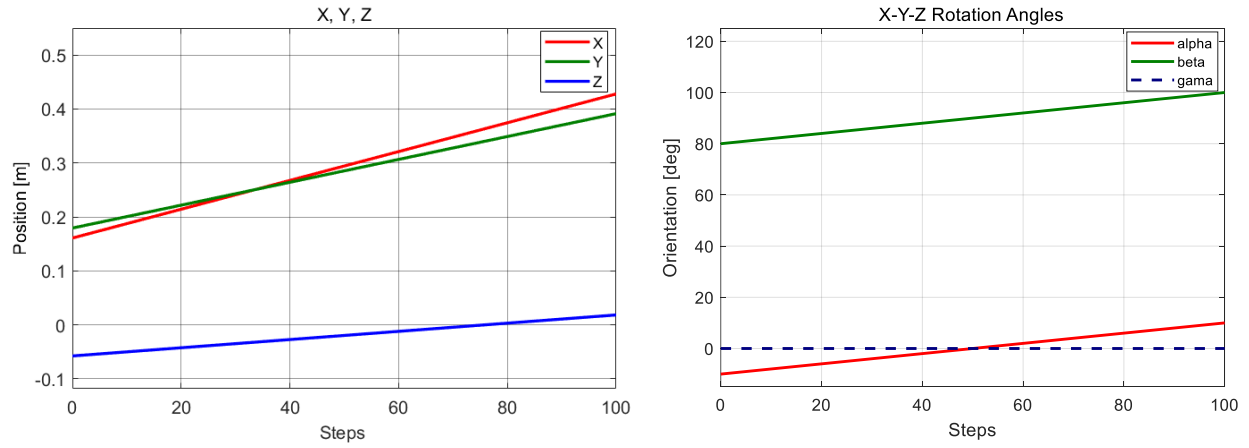

Figure 4-7, TCP pose through steps [0-100]

4.3.3 ACME Inverse Pose Kinematics (IPK)

Inverse Pose Kinematics (IPK) analysis is used to calculate the joint variables necessary to position and orient the robot's end-effector at a specified pose. According to Pieper's criterion, an analytical solution for inverse kinematics is assured for a 6-degree-of-freedom (6-DoF) serial manipulator if at least three consecutive joint axes intersect at a common point, forming a spherical wrist configuration. For ACME, this condition is satisfied when considering the TCP frame as an additional sixth degree of freedom placed coincidentally with frames $\{4\}$ and $\{5\}$. This assumption is naturally valid due to the previously established identity transformation $[{}_{TCP}^{5}T]$, effectively creating the required spherical wrist configuration.

Given this configuration, an analytical IPK solution is developed below, ensuring a precise and computationally efficient method for determining ACME's joint parameters.

ACME Analytical Six-DoF IPK Solution

The Inverse Pose Kinematics problem statement for the ACME robotic system (with the kinematic configuration previously described in Figure 4-1) can be formalized as follows:

- **Given:** The constant DH parameters (as provided in Table 4-1) and a desired end-effector pose expressed as the homogeneous transformation matrix ${}_{TCP}^{0}T$.
- **Calculate:** The corresponding joint parameters $(d_1, L_A, L_B, \theta_4, \theta_5, \theta_{TCP})$ required to achieve the specified end-effector pose.

In practical applications, the end-effector pose is usually provided in terms of the general transformation matrix ${}_{TCP}^{B}T$. To initiate the analytical IPK solution, it is necessary to determine the intermediate transformation matrix ${}_{5}^{0}T$ from the given pose using the known constant transformations. This is accomplished through the relation:

$$[{}^{B}_{TCP}T] = [{}^{B}_{0}T][{}^{0}_{5}T][{}^{5}_{TCP}T] \quad (4.23)$$

$$[{}^{0}_{5}T] = [{}^{B}_{0}T]^{-1}[{}^{B}_{TCP}T][{}^{5}_{TCP}T]^{-1} \quad (4.24)$$

The constant homogeneous transformation matrices ${}^{B}_{0}T$ and ${}^{5}_{TCP}T$, previously discussed, are identity matrices by design and not derived from the Denavit-Hartenberg parameter table. These matrices were defined based on geometric considerations of the robot's base and TCP placement. Thus, the inverse pose kinematics (IPK) equations for ACME are directly derived from the forward pose kinematics (FPK) expressions, significantly simplifying the solution compared to typical six-revolute-joint manipulators due to the clear separation of translational and rotational joint parameters.

In theory, the IPK solution involves 16 equations arising from the 4×4 homogeneous transformation matrix. However, the last row [0 0 0 1] provides no useful information, leaving 12 meaningful equations. Among these, three equations pertain to translational components, with the vertical position element (${}^{0}z_5$) depending solely on the prismatic joint displacement d_1. This simplified dependency is consistent with ACME's mechanical design, where the vertical position of the tool center point (TCP) is exclusively controlled by the vertical linear actuator's extension. Consequently, the remaining nine equations represent the rotation matrix terms, of which only three equations are independent due to the constraints of orthogonality. This structured reduction of complexity significantly streamlines the analytical IPK solution process.

$$[{}^0_5T(d_1, L_A, L_B, \theta_4, \theta_5)] = \begin{bmatrix} r_{11} & r_{12} & r_{13} & {}^0x_5 \\ r_{21} & r_{22} & r_{23} & {}^0y_5 \\ r_{31} & r_{32} & r_{33} & {}^0z_5 \\ 0 & 0 & 0 & 1 \end{bmatrix}$$

$$= \begin{bmatrix} -c_4s_5 & -c_4c_5 & s_4 & \frac{1}{2}(L_A + L_B) + 160.9 \\ c_5 & -s_5 & 0 & \frac{1}{2}(L_B - L_A) + 179.47 \\ s_4s_5 & c_5s_4 & c_4 & d_1 - 57.75 \\ 0 & 0 & 0 & 1 \end{bmatrix} \quad (4.25)$$

So d_1 can be identified as follows:

$$d_1 = {}^0z_5 + 57.75 \quad (4.26)$$

L_A and L_B are determined using the equations for ${}^0x_5$ and ${}^0y_5$.

$${}^0x_5 = 0.5 \times (L_A + L_B) + 160.9 \quad (4.27)$$

$${}^0y_5 = 0.5 \times (L_B - L_A) + 179.47 \quad (4.28)$$

Rearrange these equations to isolate the L_A and L_B.

$$\left.\begin{matrix} L_A + L_B = 2 \times {}^0x_5 - 321.8 \\ L_B - L_A = 2 \times {}^0y_5 - 358.94 \end{matrix}\right\} \rightarrow \begin{matrix} L_B = {}^0x_5 + {}^0y_5 - 340.37 \\ L_A = {}^0x_5 - {}^0y_5 + 18.57 \end{matrix} \quad (4.29)$$

To determine the joint angles θ_4 and θ_5, the quadrant-specific inverse tangent function (`atan2`) is utilized. This function effectively resolves any ambiguity associated with standard inverse trigonometric calculations, ensuring unique and unambiguous solutions for both angles.

$$\theta_4 = \text{atan2}(r_{13}, r_{33}) = \text{atan2}(s_4, c_4) \quad (4.30)$$

$$\theta_5 = \text{atan2}(-r_{22}, r_{21}) = \text{atan2}(s_5, c_5) \quad (4.31)$$

4.3.4 Verification of the IPK

To verify the accuracy and robustness of the analytical IPK model developed for ACME, three representative verification scenarios were evaluated:

1. **Zero Joint Angles Scenario:** All joint parameters are set to zero, providing a simple baseline verification.
2. **General Pose Scenario:** Arbitrarily selected nonzero joint parameters, representing typical operational conditions.
3. **Home Pose Scenario:** Defined home-position joint parameters, verifying model consistency and alignment.

Each scenario was simulated using MATLAB Simulink to visualize and confirm the correctness of the computed joint parameters relative to the intended poses. These simulations verified the analytical IPK solutions across diverse ACME configurations, ensuring their reliability and accuracy. Detailed simulation results and corresponding visual snapshots for each scenario are presented as follows. All positional displacements are consistently expressed in meters for clarity.

Examples #1

Given the required TPC pose $[{}^{0}_{\mathrm{TCP}}T] = \begin{bmatrix} 0 & -1 & 0 & 0.1609 \\ 1 & 0 & 0 & 0.1795 \\ 0 & 0 & 1 & -0.0577 \\ 0 & 0 & 0 & 1 \end{bmatrix}$

The IPK result: $\{d_1, L_A, L_B, \theta_4, \theta_5\} = \{0, 0, 0, 0, 0\}$

Simulation result: $\{d_1, L_A, L_B, \theta_4, \theta_5\} = \{6.94\mathrm{e}-18, 2.43\mathrm{e}-17, 0, 7.01\mathrm{e}-15, -3.51\mathrm{e}-15\}$

Examples #2

Given the required TPC pose $[{}^{0}_{\mathrm{TCP}}T] = \begin{bmatrix} -0.2720 & -0.0805 & -0.9589 & 0.1979 \\ 0.2837 & -0.9589 & 0.0000 & 0.2365 \\ -0.9195 & -0.2720 & 0.2837 & -0.0377 \\ 0 & 0 & 0 & 1 \end{bmatrix}$

The IPK result: $\{d_1, L_A, L_B, \theta_4, \theta_5\} = \{0.02, -0.02, 0.094, 5, -5\}$

Simulation result: $\{d_1, L_A, L_B, \theta_4, \theta_5\} = \{0.02, -2\mathrm{e}-2, 9.4\mathrm{e}-2, 5, -5\}$

Examples #3

Given the required TPC pose $[{}^{0}_{\mathrm{TCP}}T] = \begin{bmatrix} 0 & -1 & 0 & 0.2944 \\ 1 & 0 & 0 & 0.2855 \\ 0 & 0 & 1 & 0.0183 \\ 0 & 0 & 0 & 1 \end{bmatrix}$

The IPK result: $\{d_1, L_A, L_B, \theta_4, \theta_5\} = \{0.076, 0.0275, 0.2395, 0, 0\}$

Simulation result: $\{d_1, L_A, L_B, \theta_4, \theta_5\} = \{0.076, 2.75\mathrm{e}-2, 2.395\mathrm{e}-1, 1.42\mathrm{e}-14, 0\}$

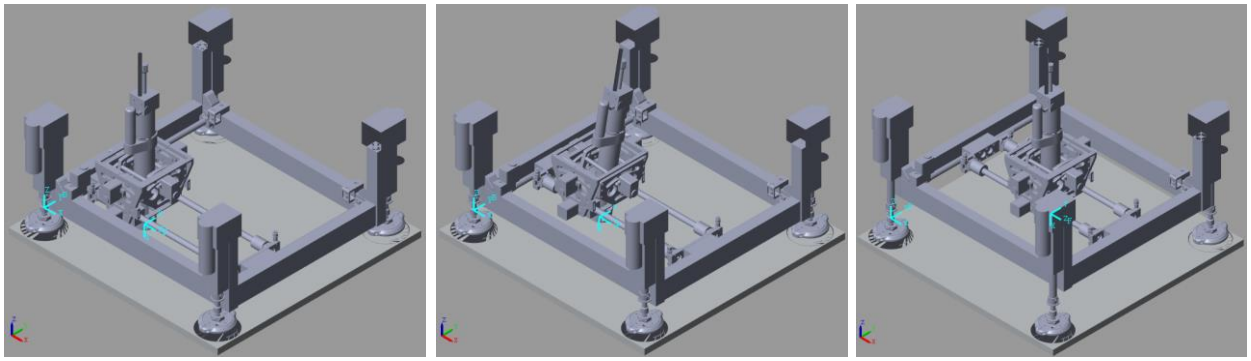

Example #1 *Example #2* *Example #3*

Figure 4-8, TCP pose in the simulation environment for each IPK example

4.4 ACME Dynamics Modelling

While kinematics involves the study of motion without considering the forces that cause it, dynamics explicitly examines the relationship between motion and the forces or torques generating that motion. Dynamics can be approached through two main types of analyses:

- **Forward Dynamics (Simulation):** Given actuator forces or torques (τ), the resulting motion, described by joint positions, velocities, and accelerations $(q, \dot{q}, \ddot{q})$ is computed. This typically involves solving a set of highly coupled and nonlinear ordinary differential equations (ODEs).
- **Inverse Dynamics (Control)**: Conversely, given a desired trajectory expressed in terms of positions, velocities, and accelerations $(q, \dot{q}, \ddot{q})$, inverse dynamics determines the required joint forces or torques (τ) to achieve that specific motion.

Both forward and inverse dynamic analyses rely on equations of motion that are inherently nonlinear and coupled. Two primary methods are widely utilized for deriving these dynamic equations:

- **Newton-Euler Method:** A recursive method based on force and torque equilibrium for each robotic link.
- **Lagrange-Euler Method:** A systematic formulation that derives equations of motion from the kinetic and potential energies of the system.

Dynamic equations incorporate both kinematic terms (e.g., linear acceleration a_i, angular velocity ω_i, and angular acceleration α_i) and kinetic terms (forces and torques). The translational kinetic aspects of motion are governed by Newton's Second Law, applied at the center of mass of each link, whereas the rotational kinetic behaviour follows Euler's equations, applicable to any

reference point on the rigid body. To simplify the dynamic modelling of ACME and avoid excessive complexity, it is initially assumed that all links and joints behave as rigid bodies, thus neglecting elastic deformations and joint compliance.

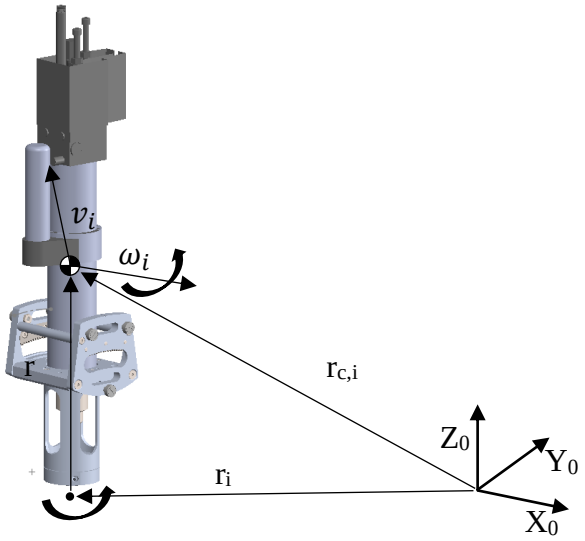

Figure 4-9, Linear and rotational velocities of link i in world frame

The ACME end-effector incorporates five degrees of freedom (DoF), consisting of three prismatic joints providing linear displacements along the X, Y, and Z axes, followed by two revolute joints enabling rotational movements about pitch and yaw axes. For accurately deriving the dynamic equations of motion for ACME, the Newton-Euler recursive method is employed, due to its computational efficiency, systematic approach, and clear physical interpretation.

Initially, the structure is modelled as rigid, with rigid links and joints. Using a forward recursion, linear velocities v_i, linear accelerations a_i, angular velocities ω_i, and angular accelerations $\dot{\omega}_i$ are sequentially computed for each link i. Under the influence of gravity acting downward, the linear velocities and accelerations propagate through the prismatic joints ($i = 1, 2, 3$) as follows:

$$v_i = R_{i-1}^{i} v_{i-1} + \dot{d}_i z_i \tag{4.32}$$

$$a_i = R_{i-1}^{i} a_{i-1} + \ddot{d}_i z_i + \dot{\omega}_{i-1} \times r_{i,i-1} \times \omega_{i-1} \times (\omega_{i-1} \times r_{i,i-1}) \tag{4.33}$$

Here, d_i represents the displacement of the prismatic joints, z_i denotes their axis of linear translation, and $r_{i,i-1}$ is the position vector from joint $i-1$ to joint i. Since these initial three joints are purely translational, their angular velocities remain unchanged:

$$\omega_i = R_{i-1}^{i}\omega_{i-1}\,, \qquad \dot{\omega}_i = R_{i-1}^{i}\dot{\omega}_{i-1} \tag{4.34}$$

For the subsequent revolute joints ($i = 4, 5$), angular velocities and accelerations are updated using:

$$\omega_i = R_{i-1}^{i}\omega_{i-1} + \dot{\theta}_i z_i, \qquad \dot{\omega}_i = R_{i-1}^{i}\dot{\omega}_{i-1} + \ddot{\theta}_i z_i + \omega_{i-1} \times \dot{\theta}_i z_i \tag{4.35}$$

Next, a backward recursion is performed, starting from the terminal link n (Tool Center Point, TCP) toward the base frame. In this step, the reaction forces and torques are calculated sequentially:

For the terminal link ($i = n$):

$$f_n = m_n a_n \tag{4.36}$$

$$\tau_n = I_n\dot{\omega}_n + \omega_n \times (I_n\omega_n) \tag{4.37}$$

For each intermediate link $i < n$, these quantities are propagated backward using:

$$f_i = R_{i+1}^{i} f_{i+1} + m_i a_i \tag{4.38}$$

$$\tau_i = R_{i+1}^{i}\tau_{i+1} + I_i\dot{\omega}_i + \omega_i \times (I_i\omega_i) + r_{c,i} \times (m_i a_i) + r_{i+1,i} \times (R_{i+1}^{i} f_{i+1}) \tag{4.39}$$

These computations yield the required joint forces and torques, fully characterizing the dynamic behaviour of ACME.

4.4.1 System Identification and Introducing Joint Flexibility

The equations presented previously (Eq. 38 and 39) describe the rigid-body dynamics of ACME's moving components. However, practical robotic systems exhibit inherent flexibility, particularly due to mechanical compliance introduced by transmission elements and joints. Such compliance significantly affects the dynamic response of the robot, making a flexible-joint model more realistic. To effectively represent motor and joint compliance in ACME, they are modelled as a spring-damper system. Specifically, prismatic joints (joints 1–3) are modelled using linear spring-damper elements, while revolute joints (joints 4–5) employ torsional spring-damper elements.

Let q_i represent the actual joint displacement or rotation, and q_{mi} denote the corresponding motor displacement or rotation. The joint dynamics can be expressed as follows:

$$J_m \ddot{q}_{\mathrm{mi}} + C_m \dot{q}_{mi} + K_{p\,or\,r}\,(q_{mi} - q_i) = \tau_m(t) \tag{4.40}$$

In this equation:

- K_p and K_r represent the linear and rotational stiffness matrices of the joints, respectively.
- J_m and C_m are the diagonal matrices of motor inertia and motor damping, respectively.
- $\tau_m(t)$ is the vector of applied motor forces or torques.

Additionally, gear ratios (R_g), if applicable, can be incorporated into the motor-side parameters as diagonal matrices, adjusting for mechanical transmission effects.

To complement the motor-side model, the dynamics of the link side of the joint is modelled as follows:

$$M_l \ddot{q} + D_l \dot{q} + K\,(q - q_m) = \tau_{ext} \tag{4.41}$$

Where:

- M_l and D_l are the link-side inertia and damping matrices,
- τ_{ext} represents external forces or torques applied to the link (e.g., drilling thrusts or reaction loads),
- $K\ (q - q_m)$ is the restoring force or torque due to the joint stiffness.

These representations capture both the actuator-side and link-side dynamics, allowing for accurate simulation of structural dynamic interactions. Incorporating both equations ensures the model accounts for deflection between motor command.

While these equations adequately capture the flexibility of ACME's internal joints, the attachment mechanism, employing suction cups beneath the linear actuators introduces significant additional compliance (see Figure 4-10). Specifically, this compliance manifests as twelve extra degrees of freedom (four planar joints, each with three degrees of freedom), arising from the interaction between the suction cups and contact surfaces. An analytical solution that explicitly incorporates all these degrees of freedom would be excessively complex and impractical.

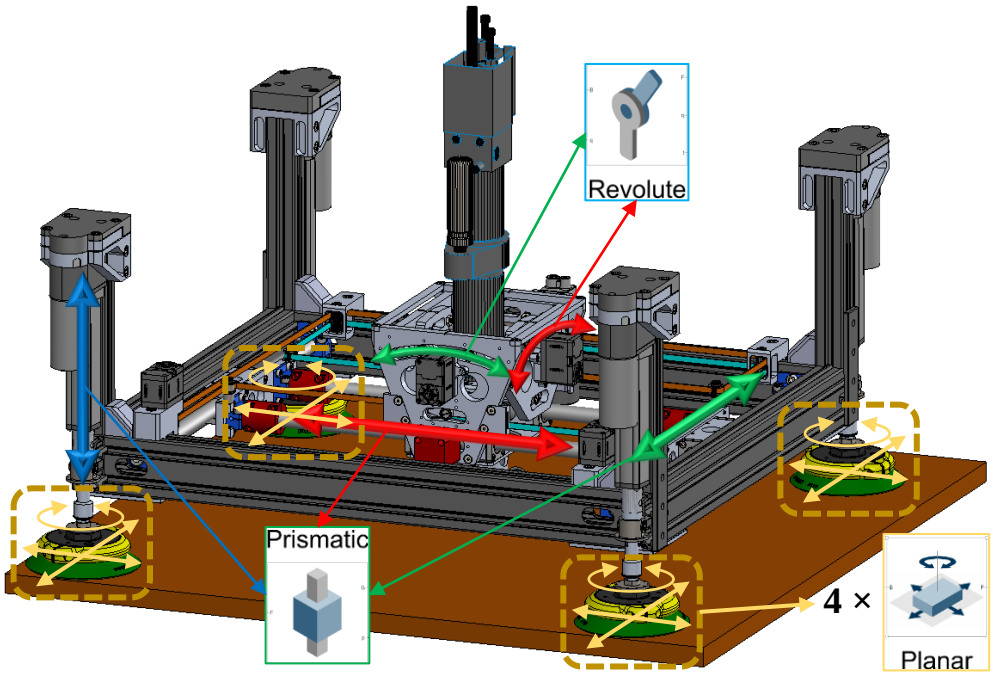

Figure 4-10, Dynamic representation of the device consists of several flexible joints

Therefore, a comprehensive numerical simulation model that fully integrates all internal joint flexibilities and these additional compliant degrees of freedom was developed using MATLAB Simulink. This numerical dynamic model effectively accounts for the complex interactions and compliance present in ACME. Such a detailed simulation approach provides a robust foundation for subsequent vibration analysis, system identification, and the development of precise vibration control strategies for the ACME robotic system.

Accurate identification of dynamic parameters is crucial for developing reliable dynamic simulations. These parameters substantially influence both the fidelity of the simulation outcomes and the robustness of subsequent analyses, such as vibration response and control strategy design. The key dynamic parameters required for ACME include lumped masses, locations of the centers of mass (CoM), moments of inertia for each link, as well as stiffness and damping coefficients associated with the joints.

To obtain these dynamic parameters, a detailed CAD model of ACME was employed. Mass properties, including lumped mass, CoM positions, and moments of inertia, were directly extracted from the geometric and material data provided by this CAD model. Specifically, the mass of each individual link was calculated based on its geometric volume and known material density. The CoM locations were precisely determined through geometric analysis, taking into account the mass distribution of each link. For computational efficiency and simplicity, each link was approximated as a rigid body with simplified geometry to compute its moments of inertia.

The resulting parameters, summarized in Table 4-2, provide essential input data for the numerical simulations conducted in MATLAB Simulink. Accurate representation of these parameters ensures realistic predictions of ACME's dynamic behaviour, thereby forming a robust foundation

for validating and refining vibration analysis, controller design, and overall system performance assessments.

Table 4-2, Mass and inertia parameters of ACME components

Link	*Mass [kg]*	*CoM [m]*	*Moments of Inertia [kg.m²]*
Main Body (Frame)	10.398	[0.2947,0.2882,0.0856]	[0.7296,0.8512,1.4088]
Y Carriage	2.154	[0.0008,0.2574,0.0000]	[0.0829,0.0077,0.0756]
X Carriage	1.432	[−0.0418,−0.0077,−0.0032]	[0.0122,0.0044,0.0130]
B Rotation	1.046	[−0.1455,−0.0000,0.0000]	[0.0062,0.0036,0.0037]
A Rotation (Including ADU)	4.196	[−0.2445,−0.0039,0.0000]	[0.0032,0.0511,0.0513]

Precise determination of joint stiffness is crucial for the realistic modelling of ACME's dynamic response. The stiffness identification process involves applying controlled incremental forces or torques to each joint and accurately measuring the resulting displacements or angular deflections. As illustrated in Figure 4-11, forces (F) are applied along the specific direction of joint motion, and the corresponding displacement (δ) is recorded using precise measurement tools, such as a Leica laser tracker. These measurements provide reliable datasets for stiffness characterization.

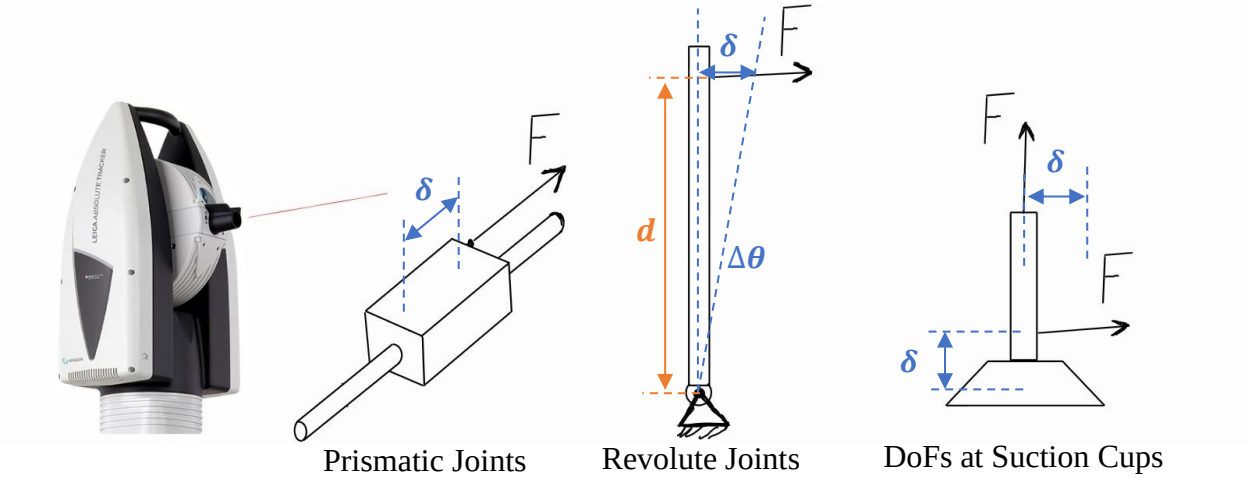

Figure 4-11, Experimental joint stiffness identification using known applied force and laser tracker sensor

Once data collection is complete, linear regression analysis is performed to derive the joint stiffness parameters. Specifically, linear joint stiffness is obtained by analyzing the slope of the force-versus-displacement curves, while rotational stiffness values are derived from torque-versus-angular displacement relationships. The rigour of this experimental approach ensures robust and accurate stiffness values, significantly enhancing the fidelity of subsequent dynamic simulations.

The linear and rotational joint stiffness parameters are determined through experimental characterization using carefully measured force-displacement and torque-angle relationships. The stiffness of prismatic (linear) joints is computed from:

$$K_i = \frac{F_i}{\delta_i} \tag{4.42}$$

Where F_i is the applied linear force (N), and δ_i is the corresponding linear displacement (m). Similarly, rotational stiffness for revolute joints is calculated as:

$$K_r = \frac{\tau}{\theta} \tag{4.43}$$

Where τ is the applied torque (Nm), θ represents the measured angular displacement (rad). The experimentally determined joint stiffness and damping parameters are summarized comprehensively in Table 4-3.

Table 4-3, Joint stiffness and damping coefficient values

Joint	*Stiffness [N/m]*	*Damping Coefficient [N/(m/s)]*
Suction cups (Planar joint) – along the X and Y axes	2.25e5	15
Suction cups (planar joint) – rotational stiffness	2.5e6	15
Suction cups (Prismatic joint) – normal stiffness	3.37e6	15
X-axis of the carriage (Clamped)	4.51e5	15
Y-axis of the carriage (Clamped)	1.73e5	15

A & B Axis	1.74e5	15

For the initial simulations, damping coefficients for each joint were estimated based on practical engineering judgment and experience with similar mechanical systems. Although exact damping values strongly influence the amplitude of structural vibrations, the precise identification of joint stiffness is particularly critical because it directly dictates the natural frequencies of the system. Inaccuracies in damping estimates primarily manifest as variations in the amplitude of the vibration peaks rather than their frequencies. Therefore, an initial informed guess provides a reasonable starting point. Once simulations and initial experiments are conducted, these damping parameters can be iteratively refined to better align simulated results with experimental observations. Such a structured approach ensures reliable dynamic simulations and provides a robust basis for detailed vibration analysis and control-system design.

The dynamic simulation model of ACME, implemented in MATLAB Simulink, comprises four interconnected components as illustrated in Figure 4-12.

- **Forward Kinematics Block:** Computes the position and orientation of the end-effector from given joint variables, essential for validating the accuracy of motion trajectories.
- **Inverse Kinematics Block:** Determines the required joint configurations to achieve specified end-effector positions, ensuring operational precision during task execution.
- **System Dynamics Block:** Captures detailed physical interactions and mechanical properties, including masses, inertias, joint stiffness, and damping coefficients, thereby accurately modelling ACME's dynamic responses.
- **Operational Force Block:** Applies realistic forces to the robot's drilling nose.

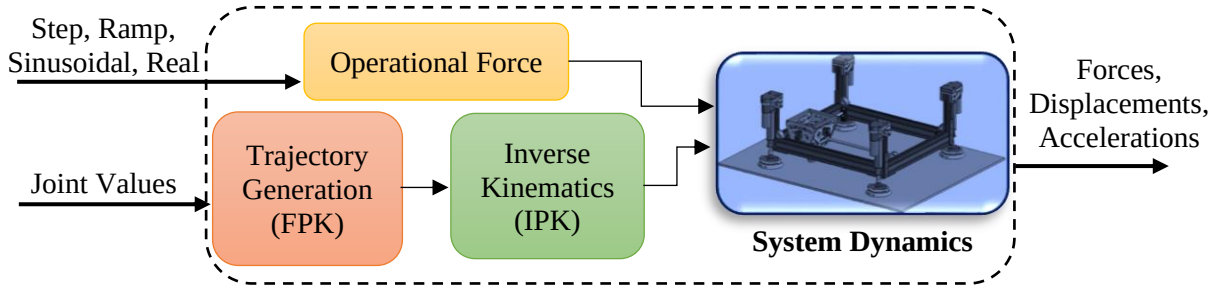

Figure 4-12, Schematic of the Simulink model (for more details, see screenshots in Appendix D0)

Comprehensive simulation provides essential insights into joint forces, structural vibrations, and positional deflections at critical points throughout the robotic structure. These outputs are fundamental for validating the fidelity and reliability of the developed dynamic model, ensuring robust performance predictions for ACME in real operational scenarios.

4.4.2 Verification of the Dynamics Model

As mentioned, due to the complex and nonlinear characteristics of the ACME system, obtaining an analytical, closed-form solution for its dynamic behaviour is impractical. Therefore, numerical simulation techniques using MATLAB Simulink were implemented to accurately analyze ACME's dynamics. However, before leveraging this numerical model for advanced applications, such as active vibration control or real-time system analyses, it is crucial to verify the fidelity of the dynamic model against realistic physical behaviours. This section outlines several verification methods performed, including quasi-static verification, frequency response function (FRF) verification, parameter sensitivity analysis, and verification under realistic dynamic loading conditions.

Quasi-Static Verification

A quasi-static verification test is performed initially to ensure the developed dynamics model conforms to fundamental mechanical principles, especially concerning static stiffness and deformation behaviour. In this test, a precisely controlled and gradually increasing ramp force, applied at a rate of 1 N/s, was introduced at ACME's drilling nose within the MATLAB Simulink simulation environment. The force was incrementally increased linearly from zero to a predefined maximum value, as depicted clearly in Figure 4-13 (b). Such controlled ramp-loading provides a methodical approach for isolating and assessing structural compliance and joint stiffness while substantially minimizing dynamic effects associated with rapid force applications.

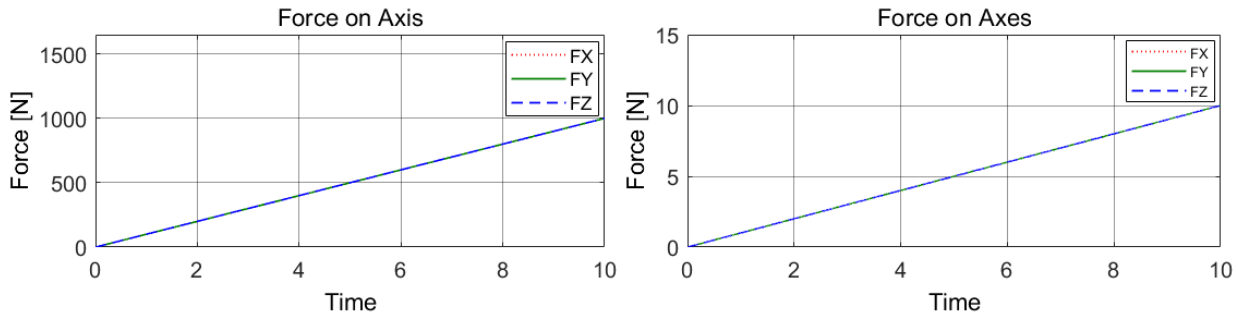

(a) *(b)*

Figure 4-13, Simulated ramp force (a) dynamic (rate of 100 N/s) (b) quasi-static (rate of 1 N/s) applied on the drilling nose at each axis

For comparative clarity, it is useful to first examine a dynamic scenario. When forces are applied abruptly (e.g., rapid loading), inertial and damping effects play prominent roles, resulting in nonlinear relationships between force and deflection, as exemplified in Figure 4-14 (a). Conversely, under controlled quasi-static loading conditions, dynamic and inertial contributions become negligible. Therefore, the resultant displacement primarily reflects structural compliance (mainly joint stiffness), allowing a straightforward verification of the sanity of the stiffness parameters.

The resulting force-versus-displacement graph from the quasi-static test, illustrated in Figure 4-14 (b), shows a clear and well-defined linear relationship between the applied force and the measured joint deflections. The observed linearity demonstrates that the developed dynamic model behaves consistently with expectations under both quasi-static and dynamic loading conditions, thereby confirming the model's general validity. However, it should be noted that this quasi-static verification alone does not guarantee the absolute accuracy of the model or its parameters in fully representing the real system behaviour.

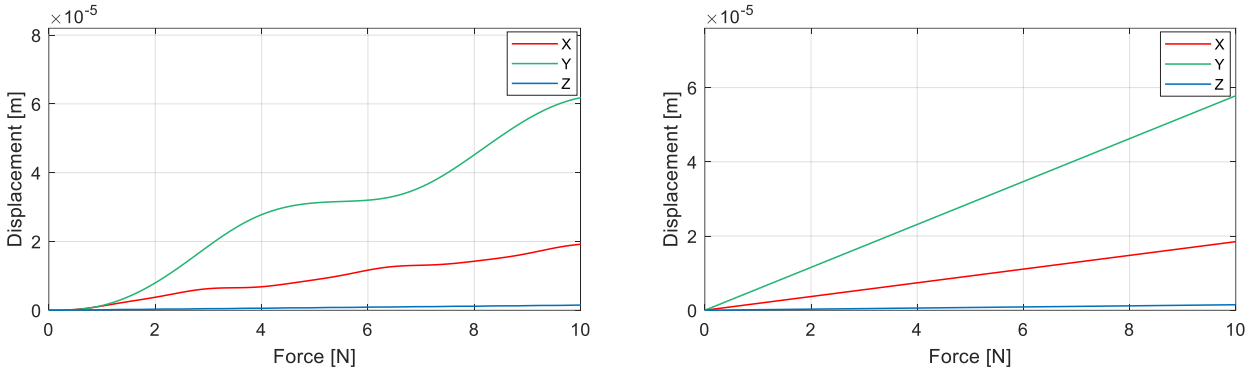

Figure 4-14, Simulated Force-Displacement relationship, (a) dynamic, (b) Quasi-static

Additionally, vibration amplitudes measured at the drilling nose throughout this quasi-static simulation remained extremely low, consistently below $6\times10e{-}4\ m/s^2$, as clearly shown in Figure 4-15. Such minimal vibration amplitudes substantiate the claim that inertial effects are negligible in the quasi-static test, further verifying the static accuracy and consistency of the numerical model. To quantitatively evaluate the accuracy of the dynamic model in the quasi-static scenario, the collected force-displacement data were analyzed using linear regression techniques. By performing this regression analysis, the inverse slope of the resulting linear fit directly provides the structural stiffness estimate for the joint. Additionally, the maximum deviation of measured data points from the linear regression line quantitatively indicates the degree of nonlinearity in the

response. Through this detailed analysis, the linearity deviations remained consistently below ±5%. This excellent agreement between the simulation results and fundamental mechanical expectations significantly reinforces confidence in both the precision of stiffness parameter identification and the structural integrity of the developed numerical dynamics model.

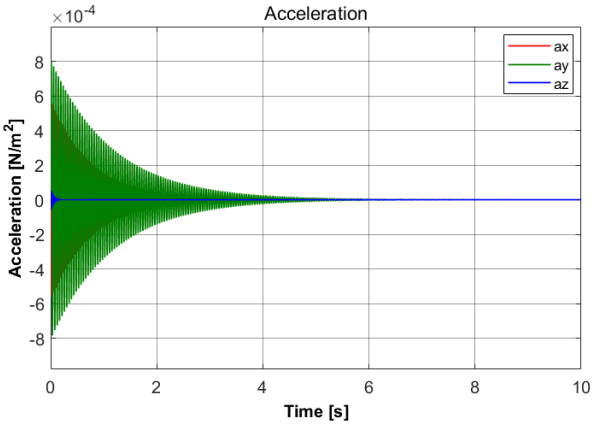

Figure 4-15, Simulated vibration resulting from quasi-static motion

Frequency Response Verification

Frequency response functions (FRFs) serve as a fundamental tool for characterizing the dynamic behaviour of mechanical systems. Given that a comprehensive analytical solution is impractical due to the inherent complexity of the ACME structure, frequency response simulations were employed to evaluate the system's dynamic characteristics. In this approach, sinusoidal forces were systematically applied within a frequency range from 0.1 Hz to 300 Hz, specifically chosen to encompass and closely examine the expected resonance regions of the system. Owing to ACME's structural composition, which includes relatively large and high inertia components, resonance frequencies within a low-frequency range (approximately 0.1 to 200 Hz) are anticipated.

The simulated frequency response functions, presented as amplitude-versus-frequency plots (see Figure 4-16), allow for the identification of critical resonance frequencies and the evaluation of damping characteristics. Peaks observed in these simulated FRFs indicate frequencies at which the

structural response amplifies significantly, corresponding directly to natural vibration modes dictated by stiffness and mass properties. Accurate matching of these resonance peaks to predicted structural behaviours serves as direct evidence of model fidelity and the correctness of identified structural parameters.

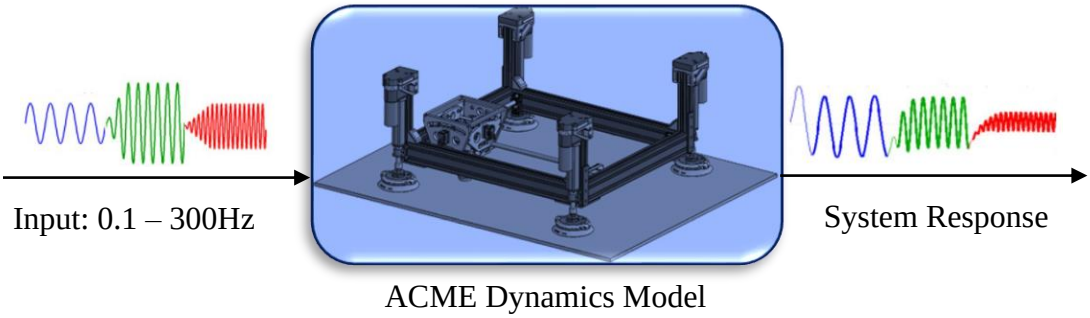

Figure 4-16, Schematic of the simulated FRF

The dynamic response is further clarified by using Bode diagrams, widely employed in vibration and control systems analysis, which represent system behaviour in terms of magnitude (gain) and phase shift against excitation frequency on logarithmic scales. Such representations provide valuable insights, highlighting resonance frequencies, evaluating system stability, and supporting vibration mitigation and control strategies.

Specifically, Figure 4-17 (a-c) depicts the Bode diagrams representing simulated FRFs along ACME's primary Cartesian axes (X, Y, and Z). The diagrams clearly illustrate distinct resonance peaks occurring at certain excitation frequencies, pinpointing conditions at which vibration amplitudes notably increase:

- **X-direction:** Prominent resonance peaks appear at approximately 31.5 Hz and 64.5 Hz. These peaks reflect frequencies at which minimal damping leads to significantly amplified displacement responses, indicating higher sensitivity to external excitations in this direction.

- **Y-direction:** Similar resonance behaviours are evident at approximately 20.8 Hz and 51.3 Hz, showing structurally sensitive vibration modes along the Y-axis.
- **Z-direction:** A distinct and higher resonance frequency peak around 134 Hz is present, reflecting greater stiffness along the vertical (Z-axis) direction compared to the lateral axes. Consequently, the resonance peak in the Z-direction exhibits noticeably higher frequency and amplitude relative to those observed in the X and Y directions.

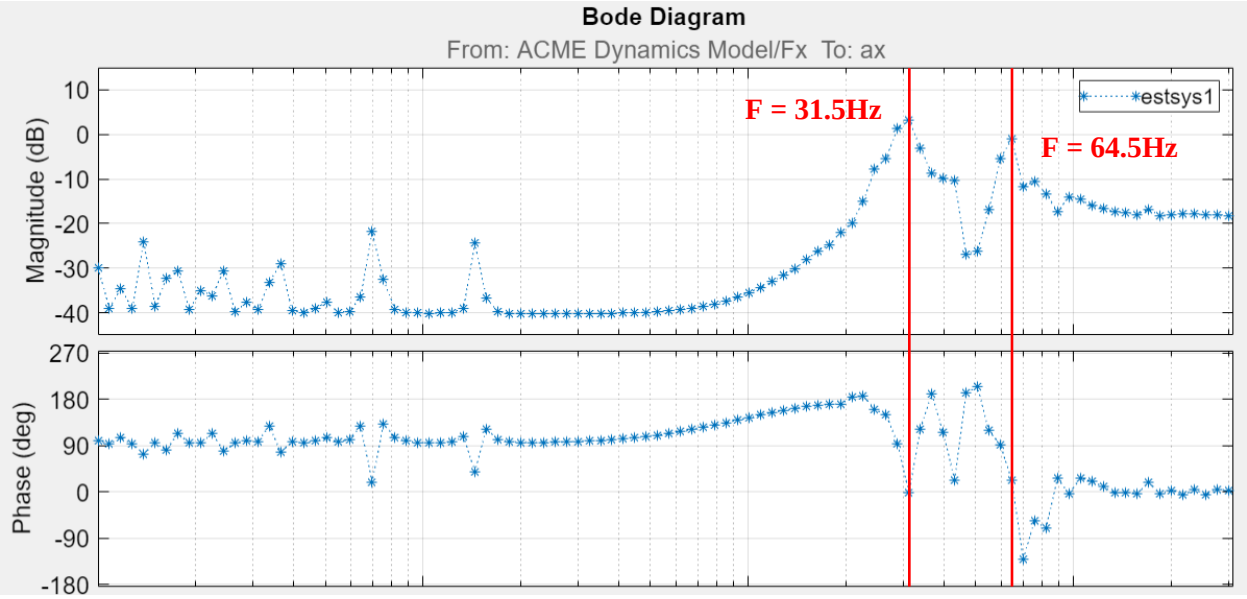

(a)

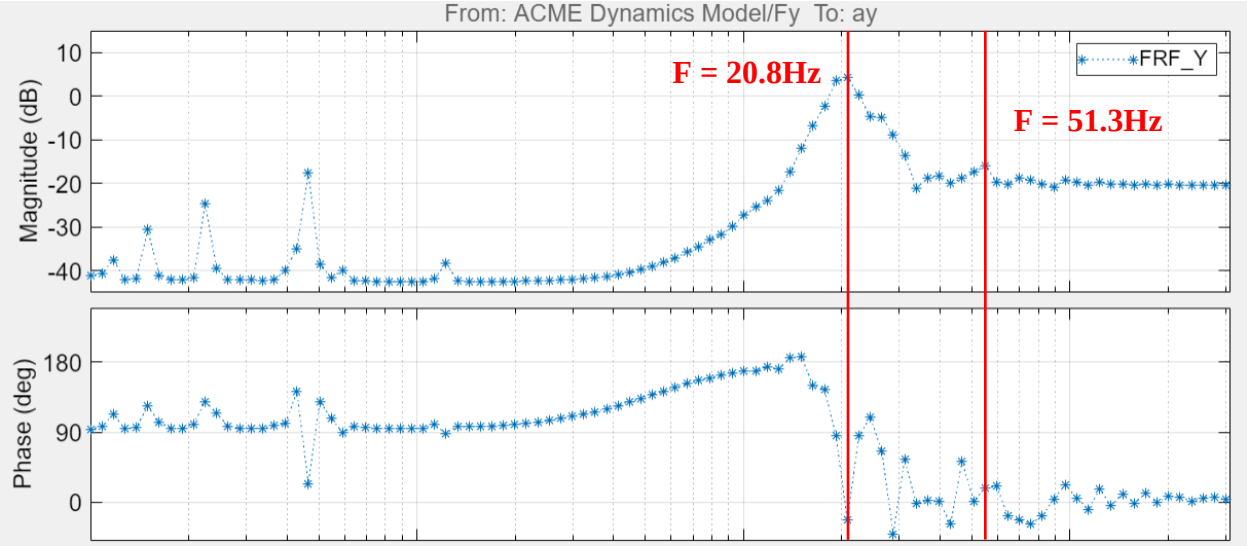

(b)

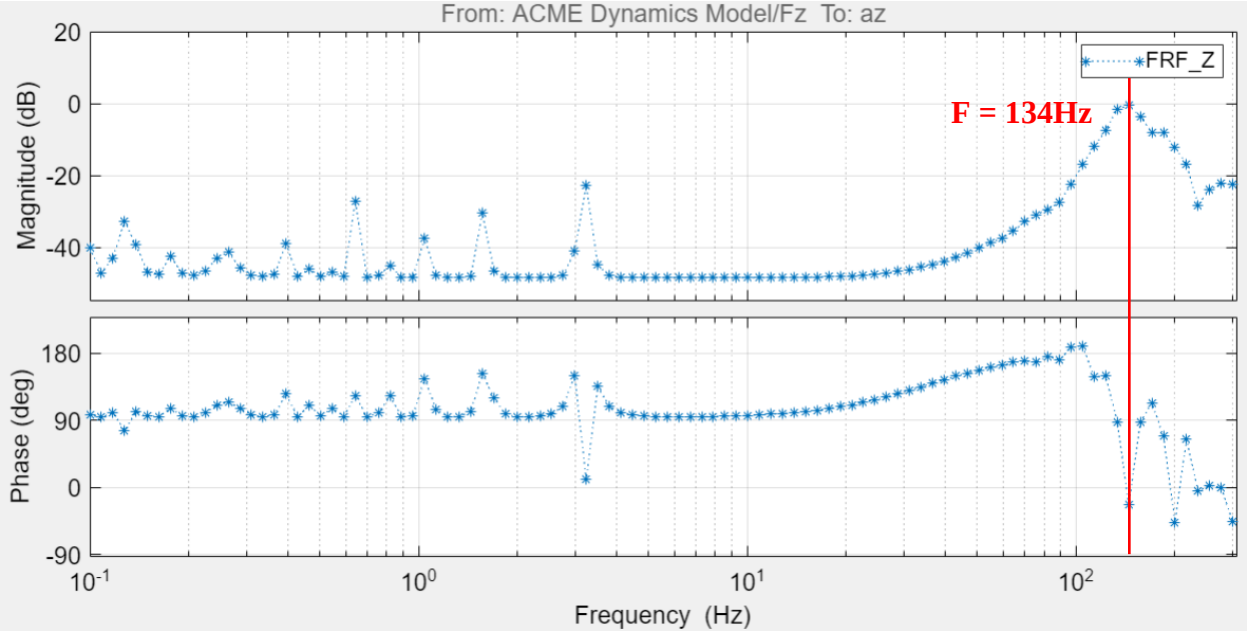

(c)

Figure 4-17, Bode diagram on the simulated FRF analysis along (a) X, (b) Y, and (c) Z axis

Accurate identification of these resonance frequencies is crucial not only for dynamic modelling but also for designing effective active vibration control (AVC) strategies, implementing vibration suppression methodologies, and defining operational guidelines that prevent the excitation of these resonance conditions. A thorough understanding of the system's FRFs ensures precision and reliability during operational tasks, especially critical in high-precision robotic drilling operations such as those performed by ACME.

To further verify the simulated FRFs and confirm the accuracy of the developed dynamic model, experimental impact tests (commonly known as hammer tests) were conducted. The test setup, illustrated in Figure 4-18, included:

- **PCB Triaxial ICP accelerometer** for vibration measurement at the drilling nose.
- **Four-component Kistler 9272 dynamometer** to capture reaction forces and moments.
- **Kistler multichannel charge amplifier** for signal conditioning.

- **Kistler impulse hammer** for generating controlled impact excitation.
- **Siemens SCADAS data acquisition system (8-channel)** to synchronize and simultaneously record hammer impact signals (1 channel), accelerations (3 channels: X, Y, Z), and force signals (4 channels: Fx, Fy, Fz, Mz).

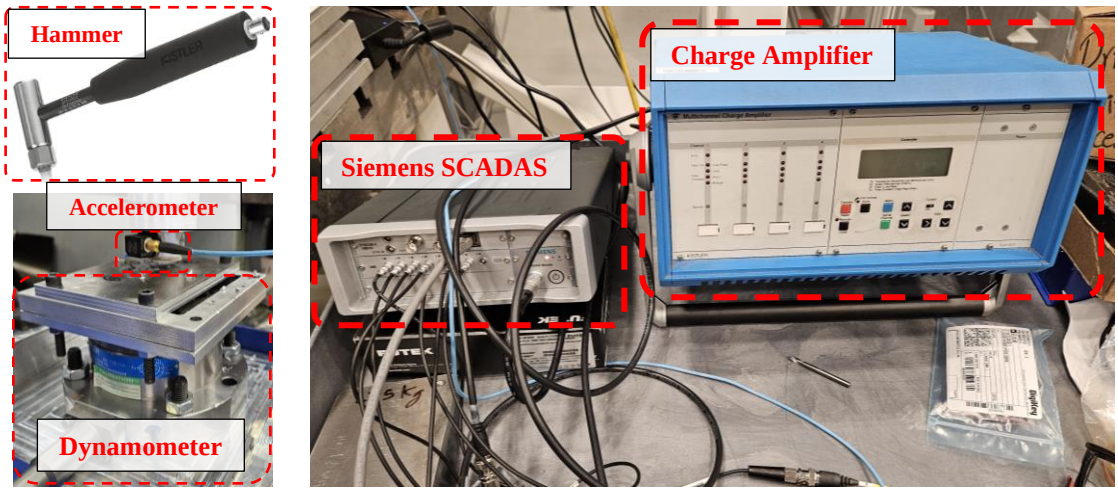

Figure 4-18, Experimental setup and instrumentation

Comprehensive tests involved systematically applying three impact excitations along each primary axis (X, Y, and Z), resulting in nine independent test scenarios. Figure 4-19 illustrates the experimentally measured FRFs alongside their corresponding simulation results. Comparisons indicate that the primary resonance peaks identified in the simulation appear clearly in the experimental FRFs, with discrepancies generally within ±20% of each simulated natural frequency. These minor deviations confirm that the identified joint stiffness parameters in the dynamic model lie well within an acceptable range of accuracy.

Additionally, the experimentally obtained FRFs exhibit more peaks, especially noticeable at higher frequencies. These additional peaks are attributed to secondary degrees of freedom and structural flexibilities not explicitly represented in the simplified dynamic simulation model. Experimental data consistently revealed closer similarities in resonance behaviours between the X and Y

directions, while the Z-axis exhibited slightly reduced coherence among repeated tests. This reduced coherence is attributed mainly to inherent variations and potential inaccuracies associated with experimental hammer impacts along the vertical direction.

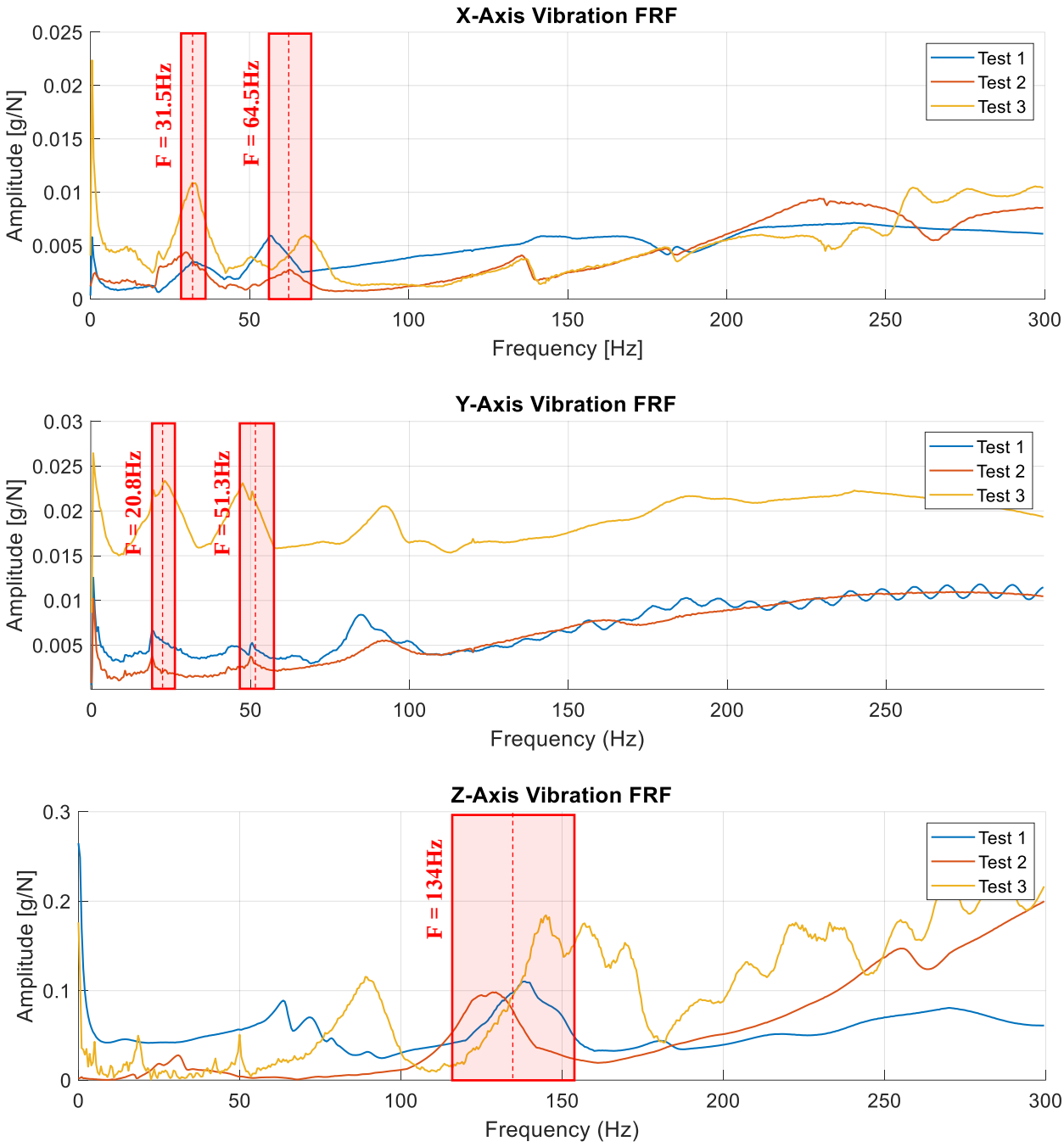

Figure 4-19, Experimental FRF of ACME

Overall, the simulated FRFs distinctly capture critical resonance frequencies, including those around the expected operational frequency (~83 Hz, correlating to a spindle speed of 5000 RPM). Close alignment between these simulation outcomes and experimentally observed resonance peaks confirms the dynamic model's accuracy and its capacity to reliably represent ACME's actual physical behaviour.

Parameter Sensitivity Checks

The robustness and reliability of the dynamic model heavily depend on accurately identified parameters such as joint stiffness, damping coefficients, and inertial properties. Given that these parameters directly affect the dynamic response of ACME, it is essential to conduct a thorough sensitivity analysis. Such an analysis systematically examines the influence of variations in these parameters within realistic ranges to determine the extent to which they impact simulation outcomes. The primary objective of parameter sensitivity checks is to confirm whether changes in model parameters result in physically consistent and predictable variations in dynamic behaviour. For instance, decreasing joint stiffness generally increases joint deflections and vibration amplitudes, whereas increasing the damping coefficient reduces vibration amplitudes and can shorten settling time, although excessive damping may lead to slower system response.

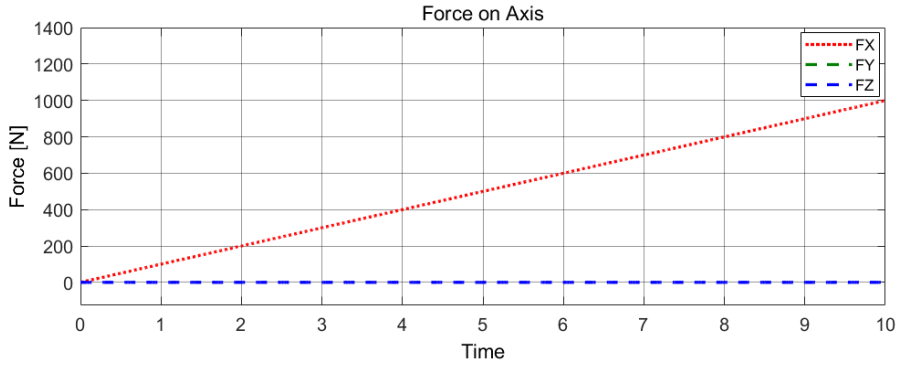

Figure 4-20, Simulated ramped force of 100 N/s along the X-axis

To rigorously evaluate the dynamic model's sensitivity, controlled simulations were performed using the Simulink model, where parameter variations were intentionally introduced, and the resulting system responses were carefully monitored. Specifically, a ramp force increasing linearly at a rate of 100 N/s was applied along the X-axis at ACME's drilling nose, as illustrated in Figure 4-20. During this simulated scenario, critical parameters, including the joint stiffness and damping coefficients for the X-axis, were systematically varied around their nominal values. The resulting impact of these variations on joint deflection (force-displacement relationship) and vibrational response (amplitude and settling characteristics) was comprehensively analyzed and is shown in Figure 4-21 and Figure 4-22.

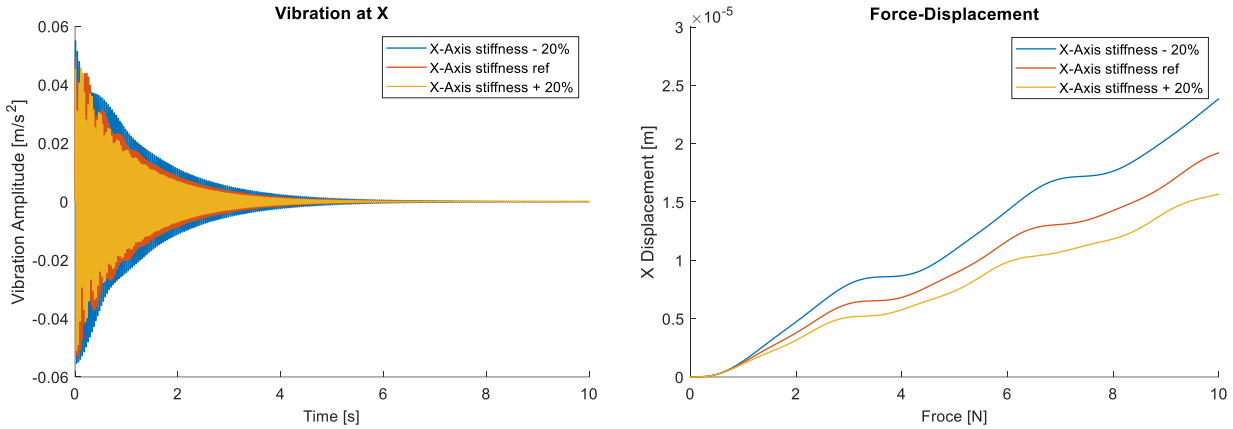

(a) *(b)*

Figure 4-21, Simulated (a) vibration amplitude, (b) force-displacement, both based on axis stiffness

Figure 4-21(a) clearly demonstrates how modifying the X-axis joint stiffness directly influences the vibration amplitude at the drilling nose. When the joint stiffness was reduced by 20% from its nominal value, an increased vibration amplitude was observed, indicating greater compliance and responsiveness of the joint. Conversely, increasing the stiffness by 20% resulted in a noticeable reduction of vibration amplitude, as expected due to higher rigidity and reduced responsiveness. Additionally, Figure 4-21(b) provides insight into the force-displacement behaviour under varying

stiffness conditions. This plot explicitly shows that higher joint stiffness leads to smaller deflections at equivalent force levels, consistent with fundamental mechanical principles

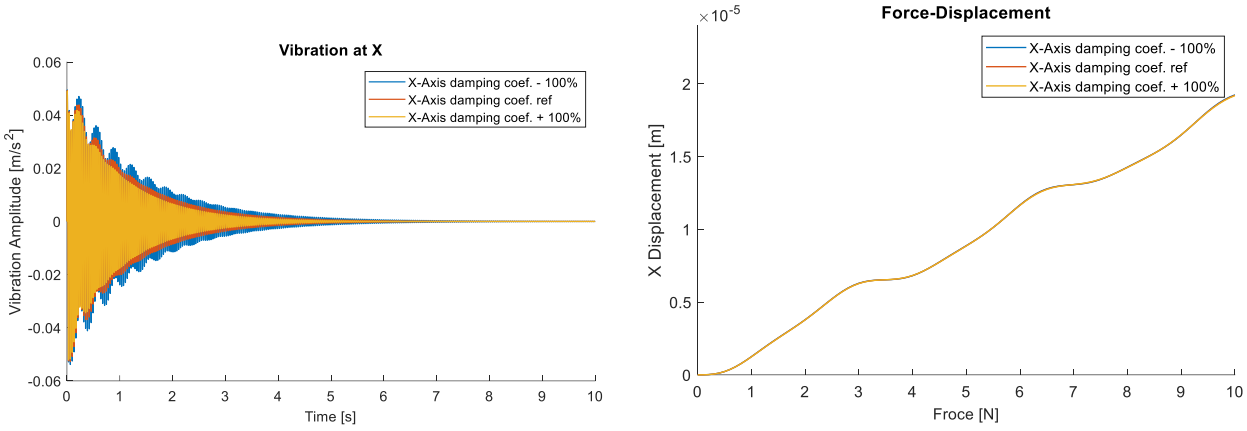

(a) *(b)*

Figure 4-22, Simulated (a) vibration amplitude, (b) force-displacement, both based on the axis damping coefficient

Similarly, Figure 4-22(a) illustrates the influence of variations in the X-axis damping coefficient on the system's vibrational behaviour, particularly regarding settling time. Doubling the damping coefficient from its initial value (+100%) significantly enhanced the system's damping capability, allowing the induced vibrations to settle rapidly to equilibrium after the initial transient response induced by the applied ramp force. Conversely, reducing the damping coefficient to zero (a 100% reduction) prolonged the vibration's settling time substantially, reflecting minimal energy dissipation. Figure 4-22(b) confirms that the damping coefficient variation primarily affects vibrational transient behaviour (system response and amplitude decay) rather than the static force-displacement relationship. Indeed, the force-displacement curve remained essentially unchanged because static deflections are predominantly governed by stiffness rather than damping parameters.

Overall, the outcomes of the sensitivity analysis affirm that the ACME dynamic model responds predictably to parameter changes, aligning closely with fundamental mechanical expectations.

These findings indicate that the selected parameters provide a robust foundation for accurate dynamic simulations and serve as reliable indicators for potential parameter refinements in future experimental studies or calibration procedures.

Realistic Dynamic Scenarios

Considering that the primary function of ACME is precise robotic drilling, thorough dynamic verification requires evaluating the model's response under realistic operational scenarios. To achieve this, practical drilling forces reflective of typical operational conditions were applied within the MATLAB Simulink environment. This detailed approach helps ensure that the model reliably predicts the system’s dynamic response under realistic working conditions.

Step Force Input on the Drilling Nose: An essential operational scenario to evaluate is the sudden engagement and disengagement of the drilling unit as it contacts and withdraws from the workpiece surface. Such sudden impacts occur frequently during drilling tasks, leading to abrupt changes in force at the drilling nose. To model this realistically, a simultaneous step force of 6 N was applied to all three Cartesian axes (X, Y, and Z) of the ACME drilling nose, as illustrated clearly in Figure 4-23 (a).

In response to this sudden loading, the dynamic model exhibited a transient vibration behaviour representative of the system's structural characteristics as expected. Specifically, vibration amplitude responses correlate closely with the system’s joint stiffness parameters, exhibiting smaller vibration amplitudes in stiffer axes such as the Z-axis, and relatively higher amplitudes in axes with lower stiffness. Additionally, the settling time after the initial transient vibration should

primarily depend upon the damping coefficients assigned to the system's joints, which were set uniformly across the model for initial testing.

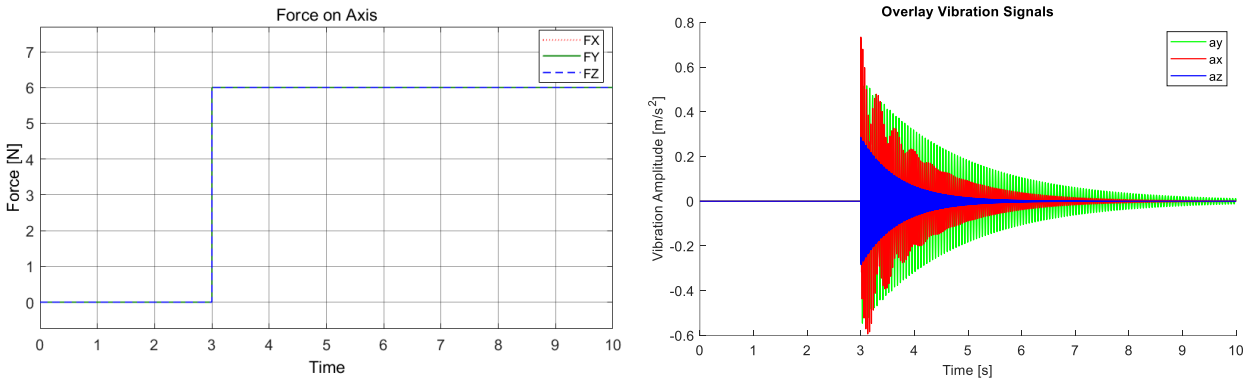

(a) *(b)*

Figure 4-23, Simulated (a) Applied step force of 6 N on each axis at t = 3 sec, (b) Resulting vibration in the model

Figure 4-24 depicts the frequency content (FFT spectrum) of vibrations induced by the step-force input. As expected, the system response is dominated by vibrations occurring precisely at the previously identified natural frequencies. Specifically, five distinct resonant frequencies (18.28, 27.78, 48.08, 58.57, and 127.54 Hz) were clearly observed, closely aligning with the peaks obtained earlier from both simulated and experimental frequency response function (FRF) analyses. Such consistency underscores the reliability and accuracy of the model's dynamic representation.

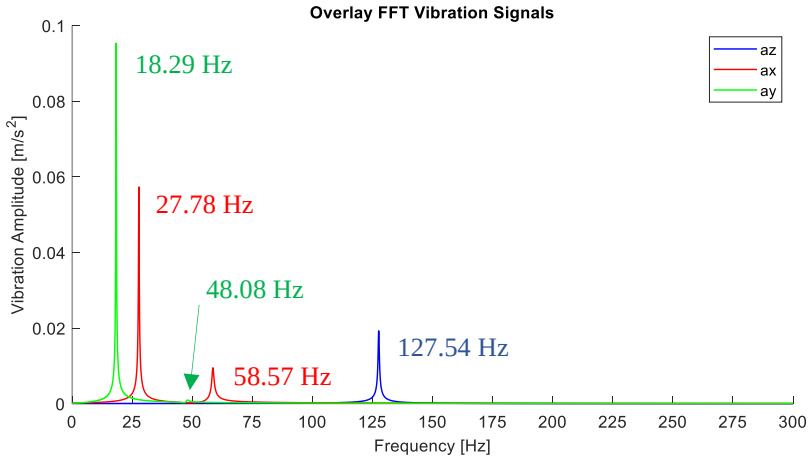

Figure 4-24, System vibration frequency response under Simulated step force inputs

Pure Sinusoidal Drilling Forces: Drilling operations inherently involve periodic excitation forces arising from the rotating drill bit. To assess how the model captures these periodic forces, sinusoidal force inputs corresponding directly to typical drilling conditions were simulated. Specifically, a sinusoidal force with an amplitude of 6 N at a frequency of 83 Hz, corresponding to the nominal spindle speed of approximately 5000 RPM, was applied at the drilling nose, as clearly illustrated in Figure 4-25 (a).

The resulting vibrations at the drilling nose are recorded in Figure 4-25 (b). The system response shows clear periodic behaviour at the excitation frequency, as anticipated. Further analysis of the frequency spectrum of these vibrations (see Figure 4-26) reveals a prominent high-amplitude peak at 83 Hz, matching precisely the applied excitation frequency. Additional lower amplitude peaks at the system's previously identified natural frequencies confirm that the model effectively captures not only the primary excitation frequency but also the secondary resonant responses associated with the system's inherent dynamic characteristics. These results further confirm the predictive capability of the dynamic model under controlled periodic excitations representative of realistic drilling conditions.

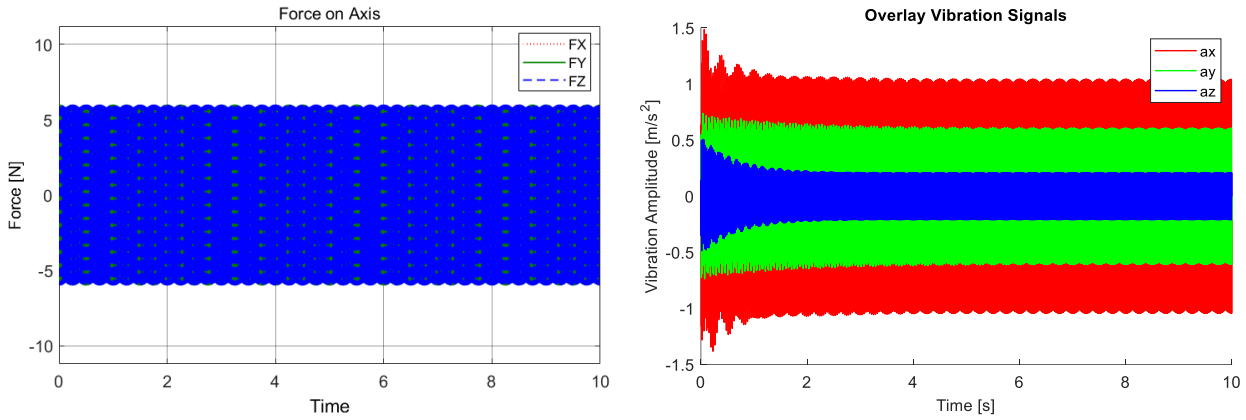

(a) *(b)*

Figure 4-25, Simulated (a) Applied sinusoidal forces with the amplitude of 6N and 83Hz and (b) Resulting simulated vibration in the dynamic model at the nose

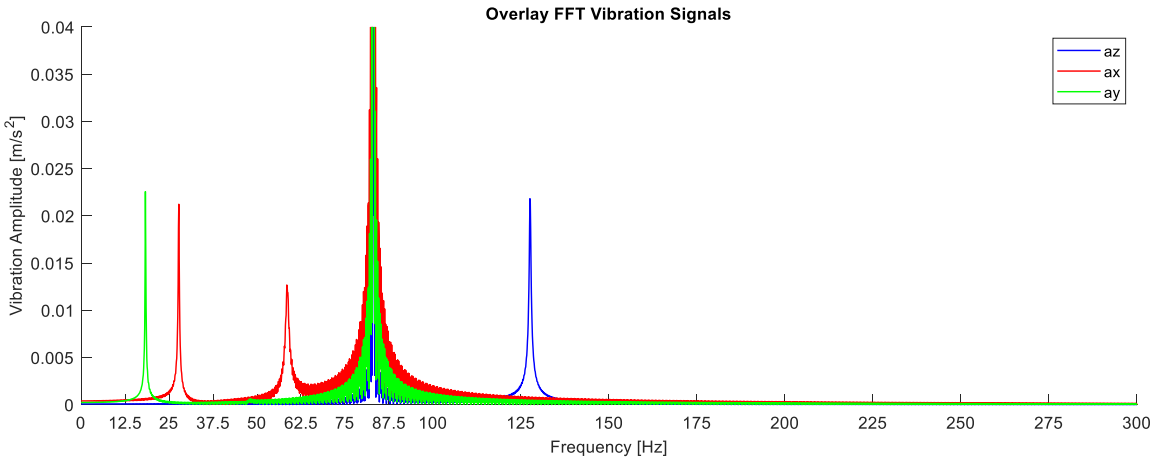

Figure 4-26, Simulated system vibration frequency response under sinusoidal force inputs

Actual Drilling Forces Measured by Dynamometer: To provide further verification under genuinely realistic conditions, experimental drilling tests were conducted to measure actual forces and vibrations experienced by ACME during practical drilling operations. A three-axis accelerometer and a three-channel Kistler dynamometer were employed for this real-time data acquisition, replicating the setup previously used for impact hammer tests (as shown in Figure 4-18). The dynamometer measured forces in three Cartesian directions (Fx, Fy, Fz), while the

accelerometer simultaneously captured vibrations at the drilling nose (ax, ay, az). All experimental data were collected at a sampling rate of 1000 Hz with a resolution of 0.5 Hz.

The experimentally measured drilling forces are presented in Figure 4-27. Initially, at approximately 4 seconds, the drilling unit started operation, subsequently engaging the workpiece at around 8 seconds. The drilling process continued for roughly 16 seconds, after which the drill retracted. The recorded forces along the Z-axis displayed a notable offset (~700 N), corresponding directly to the predefined clamping force exerted by ACME to secure the drilling unit normal to the workpiece surface.

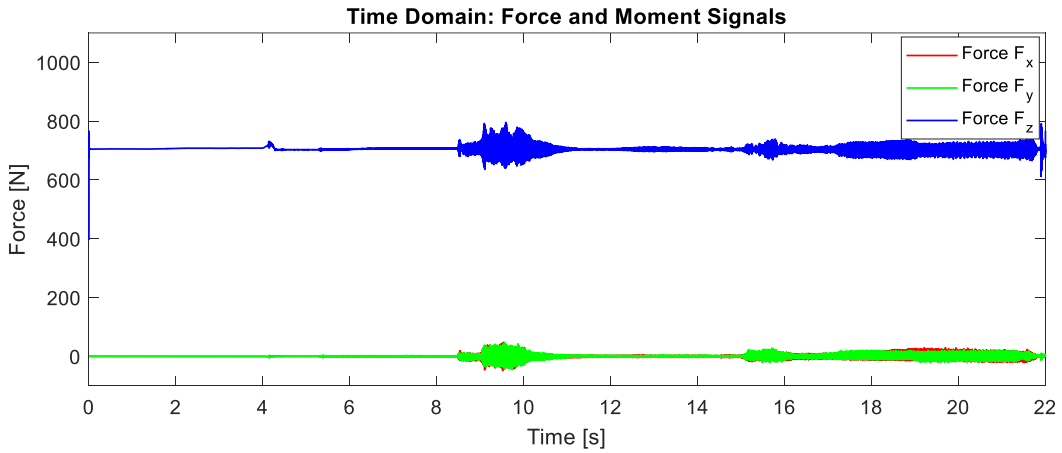

Figure 4-27, Experimental drilling forces recorded for actual drilling using ACME

Vibrations captured experimentally at the drilling nose during this real drilling scenario are presented in Figure 4-28(a), with frequency analysis depicted in Figure 4-28(b). The measured frequency spectrum prominently highlights a strong vibration peak at approximately 70.18 Hz, translating to an effective operational speed of around 4200 RPM, slightly lower than the nominal 5000 RPM spindle speed. This discrepancy is attributable to practical limitations, including minor pneumatic inefficiencies and air leakage within the drilling unit's components. Crucially, clear resonance peaks were also observed at approximately 16.54 Hz and 26.04 Hz, consistent with the model's previously identified natural frequencies in both simulation and experimental impact tests.

An additional resonance peak at approximately 127 Hz similarly matches previously established system resonance characteristics. Harmonics related to the primary drilling frequency were also evident within the experimental spectrum, further confirming the realistic nature of the recorded vibrations.

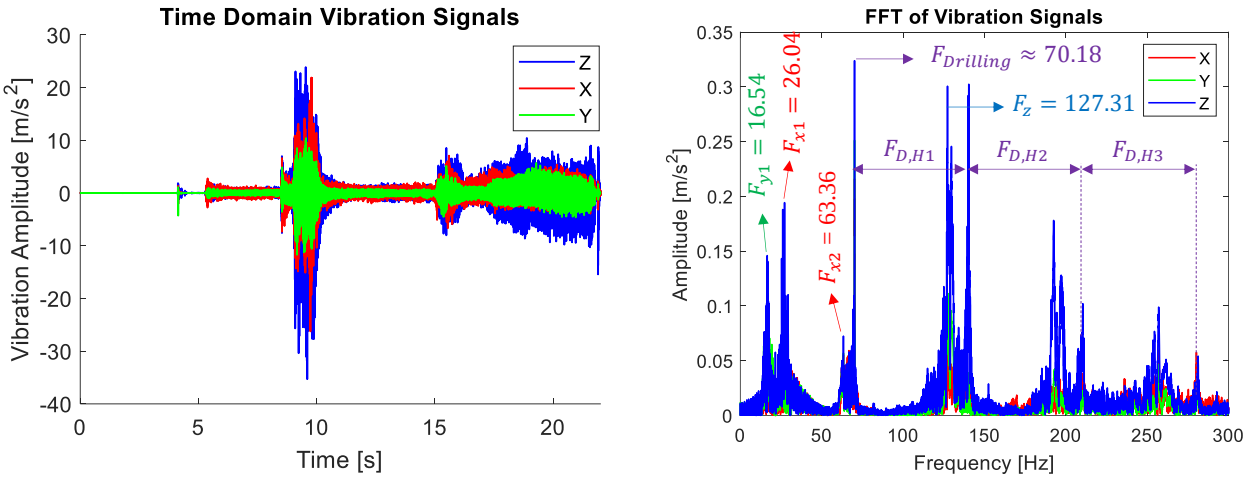

Figure 4-28, Experimental (a) process-induced vibration and (b) the existing frequencies (FFT)

For further verification, these experimentally measured drilling forces were directly applied as inputs to the MATLAB Simulink model. Simulated vibration amplitudes under these real-world conditions were lower compared to experimentally measured amplitudes (Figure 4-29(a)). This discrepancy likely arises from initially overestimated damping coefficients, resulting in excess energy dissipation within the simulation model. However, despite this difference in amplitude, the frequency content of simulated vibrations closely matched experimental observations, clearly demonstrating accurate stiffness parameter identification and overall frequency domain fidelity of the model (Figure 4-29(a)).

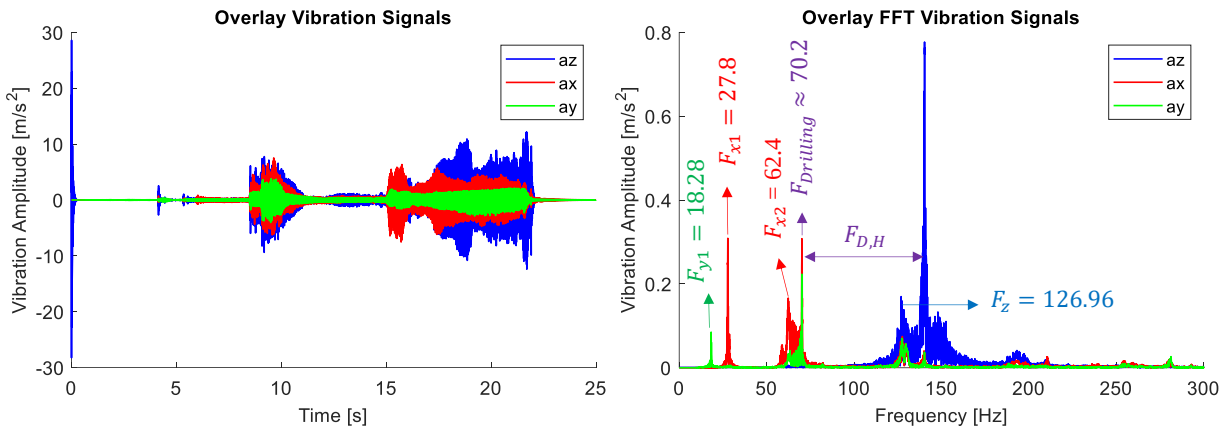

(a) *(b)*

Figure 4-29, Simulated (a) Dynamics model vibration under experimental drilling forces. (b) Simulated frequencies in the model under real drilling forces

All these realistic dynamic scenario simulations confirm expected behaviours, including step force applications that yield predictable transient deflections followed by stabilizing vibrations. Sinusoidal drilling force inputs demonstrate appropriate resonance behaviours at the system's natural frequencies, validating vibration amplitude predictions. Real drilling situation that exhibits the same vibration behaviour as expected by the model and shared peaks in the frequency domain, ensuring realistic modelling of system and operational conditions.

Verifications for the simulation outcomes show alignment with physical intuition, basic theoretical predictions and some experimental results. The verification procedures substantiate that the dynamic model developed in MATLAB Simulink is an accurate representation of the physical characteristics and operational dynamics of the ACME system and further confirms the system identification process. The model is confirmed to be sufficiently reliable and robust for use in subsequent dynamic analyses and control strategy development for robotic drilling applications.

4.5 Summary

In this chapter, the kinematic and dynamic models of the ACME drilling end-effector were comprehensively developed and verified, establishing a solid theoretical foundation essential for predicting its operational performance during robotic drilling tasks. Initially, coordinate frames and modified Denavit-Hartenberg parameters were clearly defined, facilitating systematic mathematical derivations. The forward pose kinematics (FPK) were analytically derived, explicitly integrating the CoreXY planar mechanism for the end-effector's X-Y positioning. Verification through multiple simulation scenarios and dynamic trajectory confirmed the accuracy and robustness of the developed forward kinematics equations and demonstrated reliable predictions of the tool center point (TCP) motion over realistic operational trajectories. An analytical inverse pose kinematics (IPK) solution was also established, leveraging the spherical wrist configuration inherent in the design, simplifying computations significantly. Rigorous verification using representative test scenarios ensured reliability in computing required joint parameters for precise end-effector positioning.

Furthermore, a detailed dynamic model was developed in MATLAB Simulink. Realistic joint flexibility was modelled by incorporating linear and rotational spring-damper elements. Dynamic parameters, including link masses, inertia properties, joint stiffness, and damping coefficients, were accurately identified through detailed CAD analyses and experimental verification. Extensive dynamic model verification was performed through quasi-static loading tests, simulated and experimentally obtained frequency response functions (FRFs), parameter sensitivity analyses, and realistic operational conditions. Simulations consistently matched experimental observations, validating resonance frequencies and confirming amplitude predictions under various loading

scenarios. Minor discrepancies in vibration amplitudes highlighted opportunities for refining damping parameter estimations.

Overall, the developed and verified kinematic and dynamic models provide a robust analytical and computational framework that accurately captures ACME's behaviour. This foundation is critical for subsequent active vibration control studies, controller design, and the reliable implementation of ACME in high-precision robotic drilling applications.

5 Active Vibration Controller using VCA

5.1 Introduction

Precision drilling operations in aerospace manufacturing demand stringent vibration control to prevent process-induced quality deterioration. Even minor vibrations in the drilling end-effector can negatively affect hole quality and machining tolerances, leading to poor surface finish, accelerated tool wear, and potential violations of strict dimensional requirements. The problem grows more pronounced when dealing with high-strength materials or multi-layer stacks commonly used in aerospace components. Small increases in vibration amplitude can result in significant deviations in hole roundness, position, and surface integrity. Consequently, maintaining optimal drilling performance requires a reliable vibration suppression approach.

Active Vibration Control (AVC) methods present a promising solution in these high-precision scenarios. Unlike passive or semi-active strategies, AVC leverages real-time sensor data and actively adjusts control signals to counteract vibrations as they occur. This real-time responsiveness allows for swift adaptation to variations in drilling conditions, such as changes in material composition, drilling feed rate, or cutting speed. Effective AVC implementation can minimize process vibration and enhance surface finish, thus reducing tool wear and contributing to longer tool life. Figure 5-1(a) depicts a conceptual overview of an active vibration damper interacting with a flexible mechanical system, illustrating how an actuator is driven by a controller that processes vibration feedback data. Figure 5-1(b) highlights how the main components, including the actuator, sensors, and local electronics, are virtually arranged on the ACME drilling nose to form an integrated AVC system in the simulation environment.

Among available AVC strategies, voice coil actuators (VCAs) have emerged as a suitable option for drilling applications. VCAs are electromechanical devices capable of producing direct linear forces proportional to input current, allowing for highly precise and rapid force control. Because of their inherently low moving mass and high bandwidth, VCAs excel at mitigating the medium- to high-frequency vibrations associated with cutting processes in aerospace drilling. This precision and fast response makes them especially attractive for damping unwanted oscillations in real-time. The compact form factor and straightforward integration of VCAs also reduce the mechanical complexity of attaching an active damper to a drilling end-effector.

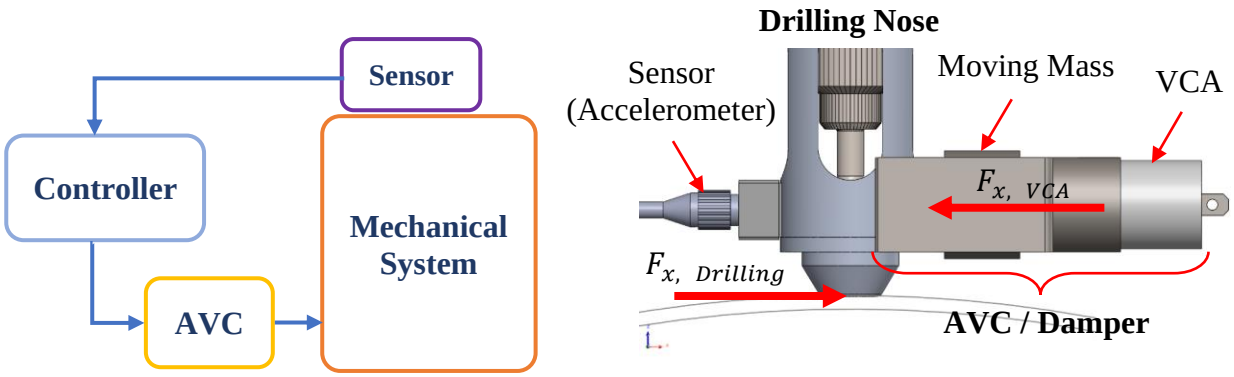

(a) *(b)*

Figure 5-1, Fundamentals of Active Vibration Control

Despite these benefits, a voice coil actuator can only generate unidirectional force along its primary axis at any given moment. This chapter therefore focuses on the vibration suppression along the X-axis, assuming that the actuator is oriented in a horizontal direction. The principles described for selecting and modelling a unidirectional VCA are transferable to other axes by modifying orientation or adding additional actuators.

The main objective of this chapter is to examine the feasibility and practicality of integrating a VCA-based active vibration control system into the ACME end-effector. Although a physical

testbed is not immediately available for full-scale experimental verification, virtual analyses and simulations offer valuable insight into system performance under various operational conditions. Preliminary steps include identifying the theoretical requirements for choosing a suitable VCA, particularly force capacity, stroke length, and the weight of the moving mass. This initial sizing ensures that the actuator meets the expected force demands without exceeding practical weight or power constraints.

This chapter's organization is as follows. Section 5.2 explains the rationale for selecting the voice coil actuator (VCA) and outlines the theoretical criteria, such as force capacity, stroke length, and system mass, that guided the choice of actuator specifications. Section 5.3 describes the integration of the chosen VCA into a virtual test environment, including the modelling assumptions, sensor-actuator arrangements, and controller design required for effective simulation. Section 5.4 reports key simulation results, evaluates the proposed control algorithms, and presents a sensitivity study on how parameter variations affect performance. Finally, Section 5.5 summarizes the findings, discusses practical challenges in implementing an active vibration controller within the ACME drilling nose, and proposes future experimental verification.

5.2 Voice Coil Actuator: Theory and Selection

Voice coil actuators (VCAs) are electromagnetic devices that convert electrical energy directly into linear mechanical motion through the Lorentz force principle. A coil placed within a permanent magnetic field generates a force proportional to the current magnitude, offering minimal friction, negligible hysteresis, and rapid frequency response. Compared to piezoelectric actuators, VCAs typically provide longer stroke lengths, higher force outputs for their size, and more straightforward control schemes. These attributes make them especially appealing for active vibration control in aerospace drilling, where real-time force regulation and a compact form factor are essential.

5.2.1 Force and Stroke Requirements

To effectively select a VCA for integration into the ACME system, it is critical to accurately estimate the required actuator force and stroke length. These parameters are derived based on the dynamic modelling conducted in Chapter 4, which identified dominant vibration amplitudes and frequencies during simulated drilling operations and real operational tests (drilling).

Based on simulation outcomes, typical vibration amplitudes at the tool center point (TCP) were quantified under representative drilling conditions, indicating a maximum expected displacement amplitude on the order of millimetres. To adequately counteract these vibrations actively, the VCA must produce a reaction force that can overcome the dynamic inertial forces involved, calculated from the mass of the actively controlled payload and the measured maximum acceleration observed during simulation.

To determine the force requirements for the VCA, the following analytical formulation was employed. The required peak actuator force ($F_{VCA,peak}$) can be estimated as follows:

$$F_{actuator} = m_{eff} \times a_{max} \quad (5.1)$$

Where $F_{actuator}$ is the actuator's required force output (N), m_{eff} is the effective moving mass (kg), and a_{max} is the maximum acceleration experienced by the moving mass (m/s²).

Considering the estimated effective total moving mass (drilling head, m_{eff}) of approximately 3 kg (including the actuator's moving coil, fixtures, and active end-effector components), and the maximum simulated acceleration (a_{max}) observed during drilling-induced vibrations, approximately 15 m/s², the nominal force requirement is calculated to be 45 N. Another way to estimate the force needed by the VCA is to pay attention to the applied drilling forces. VCA's ultimate goal is to cancel these forces by applying equal forces but in opposite direction to cancel and remove them. As can be seen in Figure 5-2, the operational forces during drilling along the X-axis are within ±45 N, which confirms the same threshold estimated before.

To account for uncertainties such as transient loads, modelling simplifications, and dynamic impacts, and to prevent saturation of the actuator, a safety margin of approximately 40% was included. Therefore, selecting an actuator with a force capacity of at least 60 N ensures robust and reliable active vibration control performance, accommodating potential uncertainties and real-world operational variability.

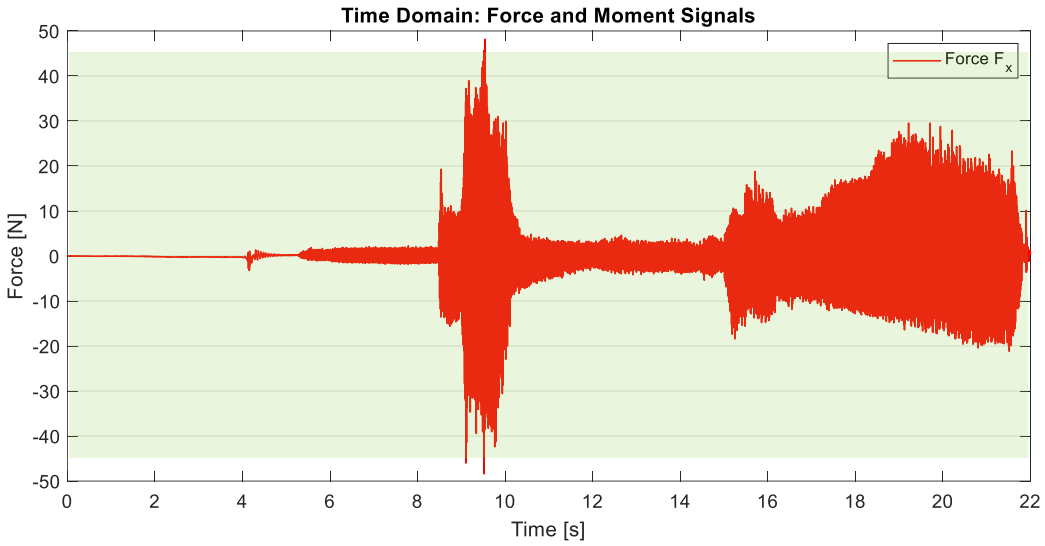

Figure 5-2, Experimental drilling forces on the nose along the X-axis

Stroke length requirements follow from the maximum drilling nose displacement observed in simulations of uncontrolled process vibrations. Typical vibration amplitudes measured around ±0.1 mm, with the damper's moving mass constituting roughly one-tenth (rough initial estimation) of the total moving mass (m_{eff}). Consequently, a stroke of at least ±1 mm is needed for reliable performance. Applying a factor of safety of three yields a recommended stroke range of approximately ±3 mm to accommodate transient overloads and prevent actuator saturation.

5.2.2 Comparative Analysis and Final Selection

Several commercially available VCAs were evaluated to meet the aforementioned force and stroke specifications. Key evaluation criteria included maximum continuous and peak force outputs, effective stroke lengths, frequency response, actuator mass, and size for effectiveness and ease of integration into the existing ACME structure.

Based on these considerations, three candidate VCAs were selected for final comparison:

1. **BEI Kimco LA16-27-000A**: 60 N peak force, 17 N continuous force, 6 mm stroke, 796 Hz response, total mass 310 grams.
2. **H2W Technologies NCM01-19-050-2I**: 66.8 N peak force, 22.3 N continuous force, 6.4 mm stroke, 530.5 Hz frequency response, total mass 417 grams.
3. **SMAC LAL95-050-75-1**: 65 N peak force, 26 N continuous force, 50 mm stroke, 1 kHz response, total mass 2,850 grams.

(a) *(b)* *(c)*

Figure 5-3, (a) BEI Kimco, (b) H2W Technologies, (c) SMAC

The H2W Technologies NCM01-19-050-2I model was selected for this application, primarily due to its balance of force output (especially high continuous force), adequate stroke length, sufficient frequency response, and optimal actuator weight facilitating easy integration into ACME without compromising overall payload constraints.

5.2.3 Selection of the moving mass

It is essential to target a minimum percentage of vibration reduction in order to select the moving mass that the VCA will frequently move to apply forces along the desired axis. To this end, a target vibration reduction of at least 50% along the X-axis is considered to study the feasibility and effectiveness of the VCA. The process of selecting the moving mass is as follows:

1. **Initialize Mass**: The initial weight of the moving mass is set to zero.

2. **Apply Drilling Force**: A sinusoidal force at the nominal frequency of the drilling unit and amplitude of maximum probable force (45N) is applied at the drilling nose.
3. **Apply VCA Force**: Have the VCA generate a sinusoidal force of matching frequency at its nominal continuous force level (22.3 N), offset by 180° in phase. Continuous force rather than peak force is used here because it must be sustained throughout the drilling operation; the peak rating is only meant for short intervals (up to 10% of total working time).
4. **Increase Mass:** The weight of the moving mass is gradually increased, and the maximum displacement of the moving mass and the percentage of vibration reduction are recorded at each increment.
5. **Determine Optimal Mass**: Identify the minimum moving mass that achieves at least 50% vibration reduction without exceeding the VCA's stroke range. Keeping the moving mass as low as possible minimizes the overall weight of the damper.

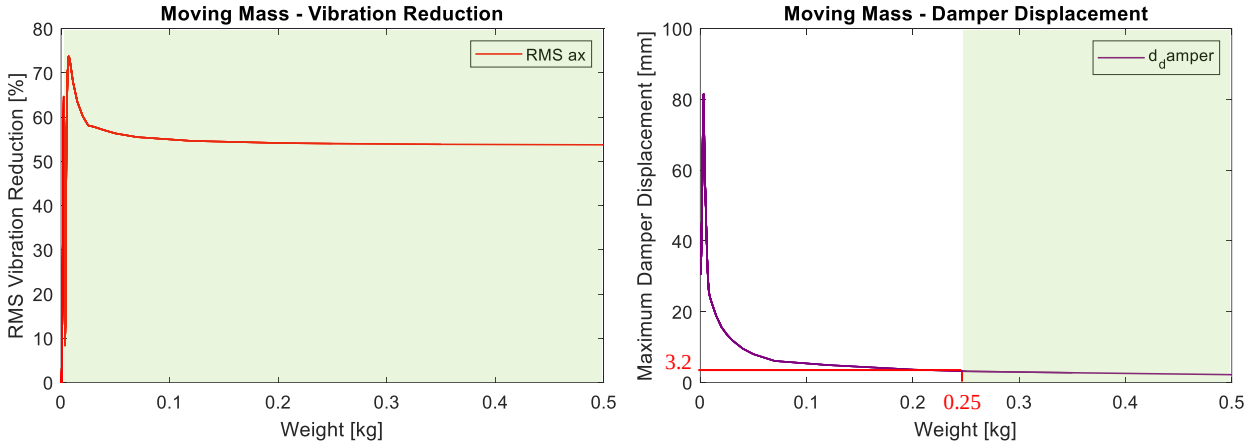

(a) *(b)*

Figure 5-4, Simulated (a) reduction in RMS vibration, (b) Maximum damper displacement, both based on the weight of the moving mass

Figure 5-4(a) illustrates how RMS vibration reduction varies with the weight of the moving mass. Aside from extremely low masses (under 5 g), the 50% vibration reduction target is achieved.

However, Figure 5-4(b) reveals that when the mass is below 0.25 kg, the moving mass displacement exceeds the actuator's stroke, leading to damper saturation. Consequently, any mass lower than 0.25 kg cannot realistically achieve the targeted vibration suppression. Therefore, 0.25 kg is chosen as the minimal moving mass, maintaining both the desired vibration reduction and a low overall damper weight.

The subsequent sections of this chapter focus on the implementation of this damper into the dynamic simulation model, the development of an active vibration control algorithm, and the evaluation of its effectiveness through rigorous simulation-based analyses.

5.3 Dynamic Modeling and Simulation Integration

The dynamic model developed in Simulink in Chapter 4 forms the foundation for assessing AVC effectiveness using the selected VCA. This multi-body model implemented in MATLAB Simulink captures the structural dynamics and vibrations characteristic of ACME during drilling operations. By systematically adjusting actuator inputs and monitoring the resulting system responses, the simulation environment provides insights into optimal control strategies, potential performance trade-offs, and overall system stability prior to any physical implementation.

5.3.1 Integration of the VCA Model into Simulink

The selected VCA was modelled and integrated into the existing Simulink dynamic model to simulate active vibration control effectively. The VCA modelling includes parameters critical to its dynamic response, specifically:

- **Mass and Stroke**: The overall damper assembly, as shown in Figure 5-5, weighs approximately 1.75 kg, comprising the VCA itself, a moving mass, and accompanying casing. Within this total, the moving mass is set at 0.25 kg, while the casing and attached components constitute the remaining 1.5 kg. The moving element travels across a ±3.2 mm stroke range.
- **Damping**: Minimal damping characteristics typical of VCA were included, with a viscous damping coefficient estimated at 1 Ns/m.
- **Stiffness**: The VCA is assumed to have low mechanical stiffness (linear spring), as is typical with electromagnetic actuators and is assumed to be around 800 N/m.

- **Force Characteristics**: The actuator force output is modelled linearly, proportional to the input current provided by the controller.

Assumptions in Simulation:

- The actuator behavior is assumed ideal, neglecting electromagnetic nonlinearity, hysteresis, and friction.
- Mechanical interactions between the actuator and the ACME structure are simplified; rigid attachment points without losses are assumed.
- Thermal effects and electrical losses are neglected due to short operation times typical of vibration suppression tasks.

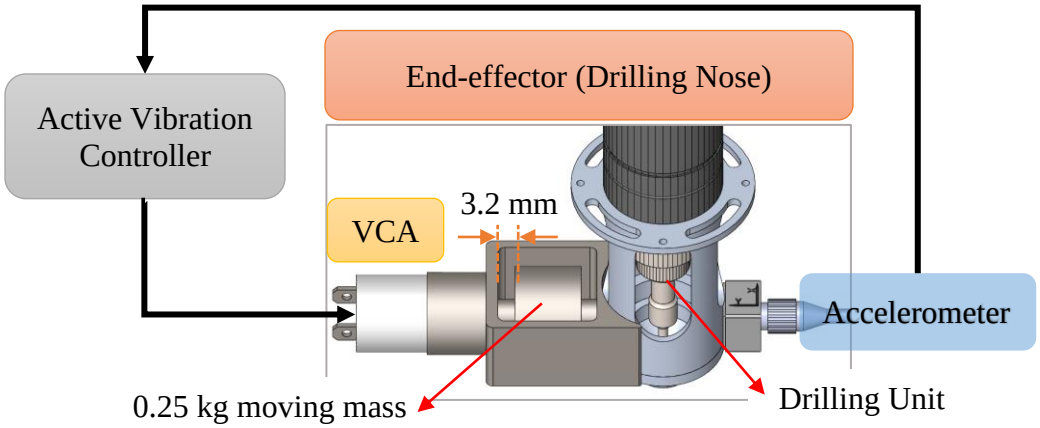

Figure 5-5, Vibration damper virtually placed on the ACME drilling nose

The actuator was virtually placed to apply counteracting forces at the drilling head, where process vibrations are most significant. The placement ensures maximum efficiency in controlling critical vibration modes.

5.3.2 Control Methodology

The adopted active vibration control framework utilizes an acceleration feedback control loop to rapidly counteract drilling-induced vibrations. Real-time acceleration data from the tool center point (TCP) is relayed to the controller, prompting the voice coil actuator (VCA) to apply corrective forces as needed. In addition, displacement of the VCA's internal moving mass is monitored to safeguard against stroke saturation, ensuring that corrective motions remain within operational limits during extended drilling activities.

- **Sensor Feedback**: Accelerations at the tool center point (TCP) were used as real-time feedback inputs.
- **Displacement:** Displacement of the moving mass inside the damper was used to make sure the VCA did not get saturated while cancelling the vibration.

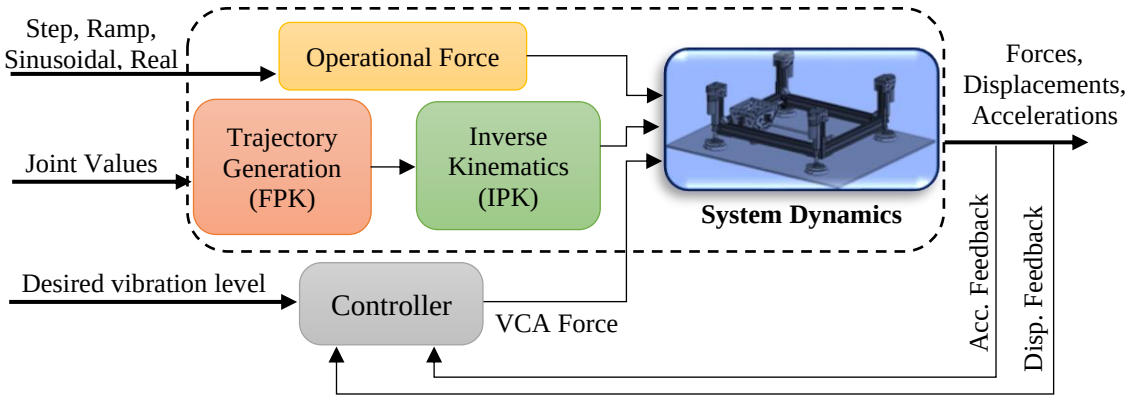

Figure 5-6, Schematic of the Simulink model including vibration controller

The active vibration control strategy employs two proportional (P) controllers in parallel, each fulfilling a specific role in regulating the actuator's output force. Figure 5-7 schematically illustrates the control loops.

Vibration Control Loop: The primary loop focuses on vibration suppression. The measured acceleration, a(t), is fed into a proportional controller that computes a corrective force based on the instantaneous acceleration:

$$F_{vib}(t) = K_{p,vib}\, a(t) \tag{5.2}$$

where $K_{p,vib}$ is the proportional gain for vibration control. This loop counters high-frequency vibrations by directly responding to changes in measured acceleration.

Position Control Loop for Stroke Centring: A second proportional controller maintains the VCA's moving element near its central stroke position, preventing bottoming out or saturation during large vibrations or lengthy transients. Let x(t) denote the measured actuator position (e.g., via internal VCA or external displacement sensor), and x_{ref} be the desired central position. The position control law is formulated as:

$$F_{pos}(t) = K_{p,pos}\,[x_{ref} - x(t)] \tag{5.3}$$

where $K_{p,pos}$ is the proportional gain for positioning. This loop provides a low-frequency corrective force to re-center the actuator and prevent stroke limits from interfering with vibration control.

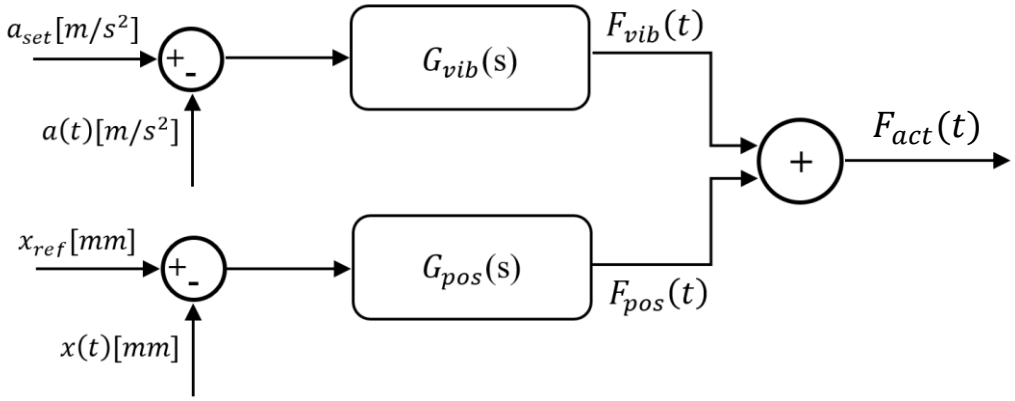

Figure 5-7, VCA controller schematic

Combined Control Output: The final actuator force, $F_{act}(t)$, is the sum of the outputs from these two loops:

$$F_{act}(t) = F_{vib}(t) + F_{pos}(t) \tag{5.4}$$

By separating these two tasks (vibration suppression and stroke centring) into individual P loops, the controller maintains simplicity while allowing each loop to be tuned to its own frequency range. The acceleration loop operates primarily at higher frequencies to address rapid vibrations, whereas the position loop ensures stable, near-midpoint positioning over longer time scales.

Controller Rationale and Implementation

Using two proportional controllers in parallel presents several advantages. The vibration control loop is straightforward to implement and computationally inexpensive, which is important for the high sampling rate required in AVC. Furthermore, since the position control loop does not require derivative or integral action in this application, the risk of noisy or drifting signals is minimized. This structure is also well suited to open-architecture environments where real-time data from both the accelerometer and the actuator position sensor can be processed at high speed.

The gains $K_{p,vib}$ and $K_{p,pos}$ must be empirically tuned. High $K_{p,vib}$ values can cause overshoot or instability if the actuator's mechanical limits are reached, whereas an overly small gain may fail to suppress vibrations effectively. Similarly, $K_{p,pos}$ is chosen to avoid excessive corrective forces that would interfere with vibration suppression. Maintaining the actuator near the center of its stroke is essential to avoid impacts at the stroke limits, which could introduce unwanted impulses and increase wear.

Gain Tuning Procedure

Gain tuning for the two proportional controllers was carried out in multiple stages to balance stability, responsiveness, and noise sensitivity. The process began by obtaining a linearized model of the system around its nominal operating point, using the frequency response function (FRF) data generated in Chapter 4. This linearized model served as a starting point for systematic gain selection. An iterative refinement phase followed, where the initially selected gains were tested in higher-fidelity simulations (including nonlinear effects) and adjusted to optimize performance under realistic operating conditions.

It is important to note that the AVC approach presented in this work and utilizing the two proportional controllers in parallel was chosen primarily for their simplicity, ease of tuning, and effectiveness in demonstrating the feasibility of active vibration suppression within a simulation environment. While this control scheme effectively illustrates the potential for vibration reduction, real-world applications would necessitate more sophisticated control strategies. Controllers incorporating integral or derivative actions, such as proportional-integral (PI) or proportional-integral-derivative (PID), are recommended to effectively address external disturbances, system nonlinearities, and dynamic uncertainties typically encountered during actual aerospace manufacturing operations. The implementation of more advanced controllers would improve robustness, stability, and overall performance of the AVC system in practical scenarios.

5.4 Simulation-Based Verification

To evaluate the effectiveness and robustness of the proposed active vibration control (AVC) strategy, simulation-based verification was conducted under various drilling scenarios representative of operational conditions in aerospace applications. Each scenario included different combinations of drilling force profiles, vibration frequencies, and structural dynamic responses derived from the verified model introduced in Chapter 4. The voice coil actuator (VCA), integrated into the dynamic model as described in Section 5.3, was controlled through an acceleration+position-feedback loop targeting vibration reduction along the X-axis.

In all cases, four key metrics were analyzed: (1) Root Mean Square (RMS) of vibration at the Tool Center Point (TCP), (2) Fast Fourier Transform (FFT) of the vibration signal to reveal frequency-domain improvements, (3) VCA-generated control force over time, and (4) VCA moving mass displacement. These outputs collectively describe both the effectiveness and physical feasibility of the AVC system under variable dynamic conditions.

Case 1 – Low-Frequency Oscillation with Sudden Engagement of Drilling Unit

This scenario emulates a sudden interaction between the drill and the workpiece, modelled as a step input force of 45 N along the X-axis. The applied disturbance represents low-frequency structural excitation with rapid onset, typically observed during drilling entry or abrupt tool engagement. Simulation results indicated a 75% reduction in RMS vibration amplitude when the AVC system was activated (Figure 5-8(a)). Frequency-domain analysis revealed significant attenuation of low-frequency components (Figure 5-8(a)), and the VCA operated well within its stroke and continuous force limits. The actuator displacement remained below ±3 mm (Figure 5-9

(b)), and control forces did not exceed 45 N (Figure 5-9 (a)), confirming stable and effective behaviour in this regime.

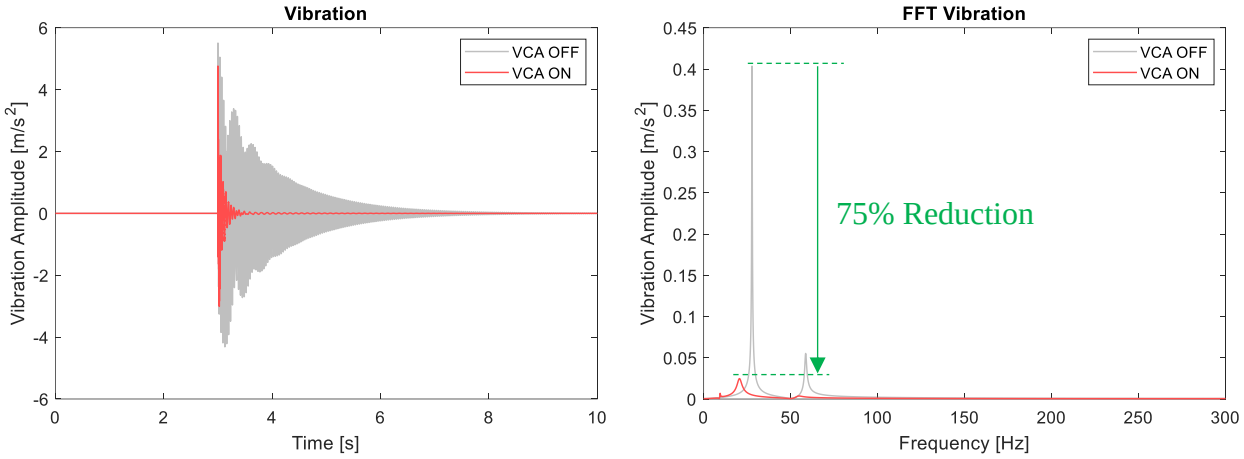

(a) *(b)*

Figure 5-8, Simulated (a) system vibration response and (b) frequencies under step force with and without VCA

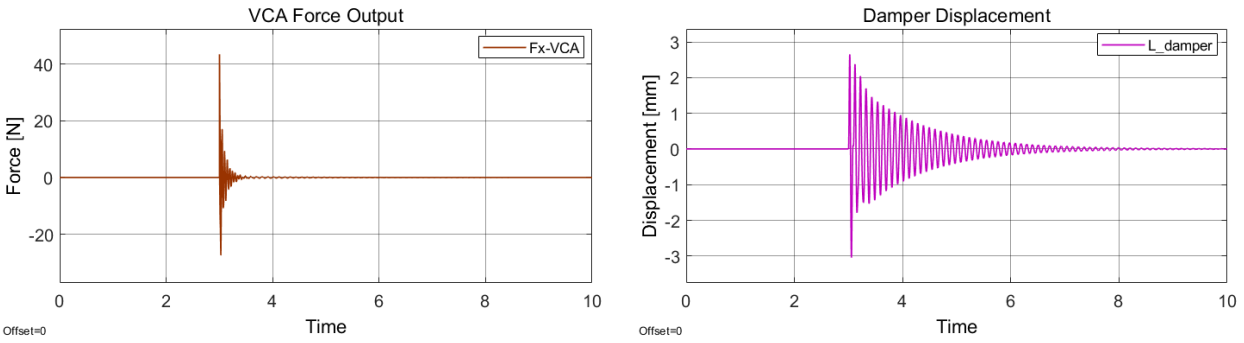

(a) *(b)*

Figure 5-9, Simulated VCA (a) applied forces and (b) displacement within its stroke under step forces input

Case 2 – Nominal Drilling Load with Mid-Frequency Disturbance

In this test, a pure sinusoidal force with an amplitude of 45 N was applied at a frequency corresponding to the nominal speed of the drilling unit, representing mid-frequency process

vibrations characteristic of continuous cutting operations. The AVC system achieved a 60% reduction in RMS vibration amplitude (Figure 5-10(a)), with clear suppression of the dominant excitation frequency in the FFT spectrum (Figure 5-10(b)). Although the actuator force approached the upper end of its continuous rating (Figure 5-11(a)), it remained below the saturation threshold. VCA displacement was constrained within ±2 mm (Figure 5-11(b)), ensuring sufficient operational margin and validating the selected stroke length.

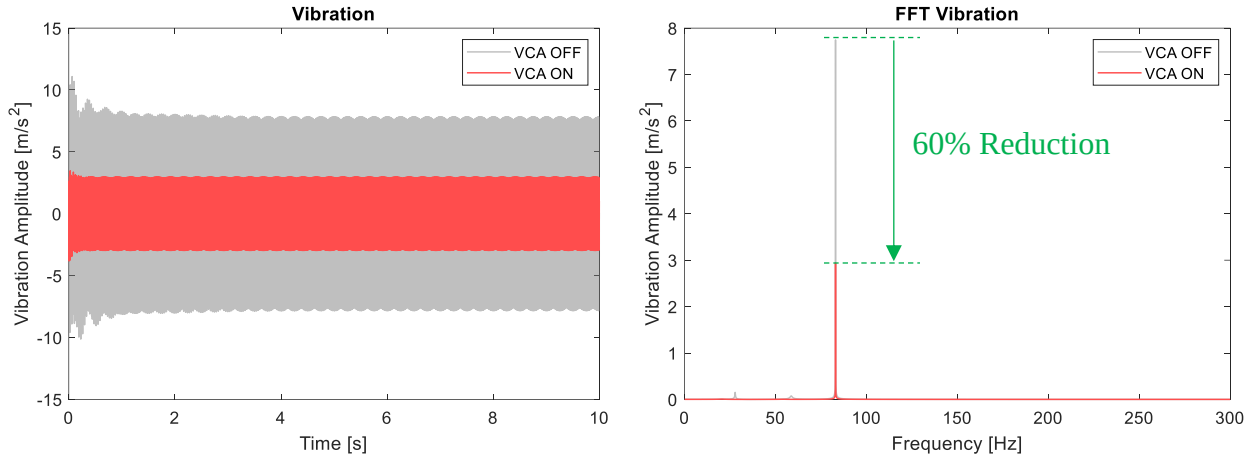

(a) *(b)*

Figure 5-10, Simulated (a) system vibration response and (b) frequencies under pure sinusoidal forces with and without VCA

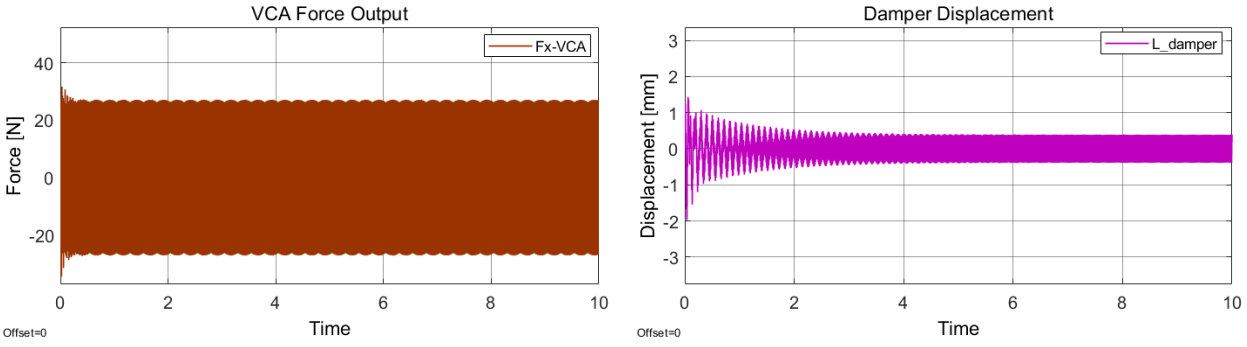

(a) *(b)*

Figure 5-11, Simulated VCA (a) applied force (b) displacement within its stroke under pure sinusoidal force input

Case 3 – Real Measured Drilling Forces

The third and most comprehensive case used real measured drilling force data, containing a spectrum of low, mid, and high-frequency components. This case closely replicates actual operational conditions with their inherent variability and unpredictability. Despite the complexity of the excitation profile, the AVC strategy resulted in a 53% reduction in RMS vibration (Figure 5-12(a)). While the control system successfully attenuated both low- and mid-frequency content, high-frequency components were less effectively suppressed. This limitation is evident in the FFT analysis (Figure 5-12(b)), where residual peaks remain at higher frequencies, likely due to the limited bandwidth of the actuator and the growing demand for higher control forces. Displacement of the VCA moving mass approached ±0.8 mm during transient events (Figure 5-13(b)), significantly less than the actuator's mechanical limit. Nonetheless, actuator performance remained within the defined stroke and continuous force boundaries (Figure 5-13(a)).

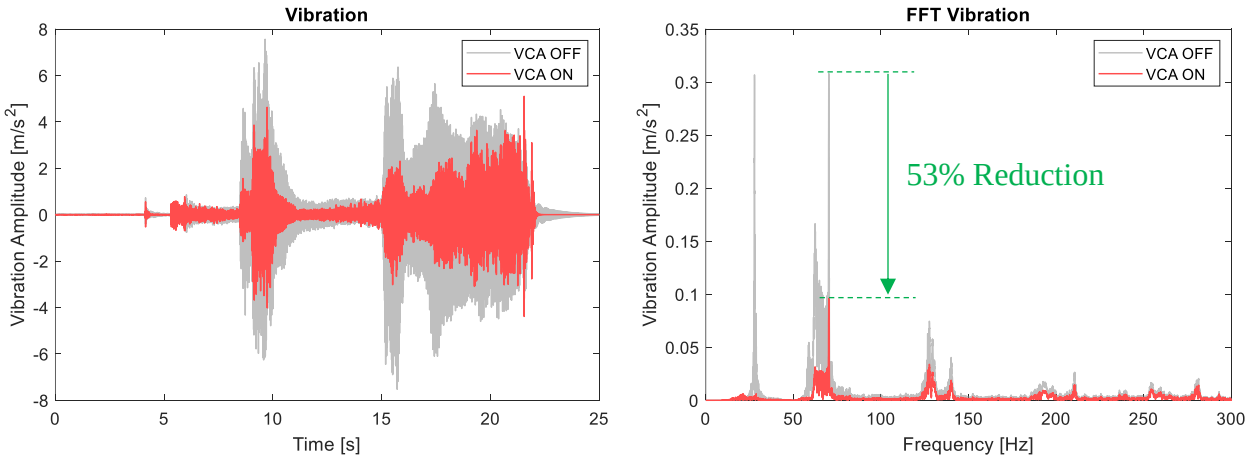

(a) *(b)*

Figure 5-12, Simulated (a) system vibration response and (b) frequencies under real drilling forces with and without VCA

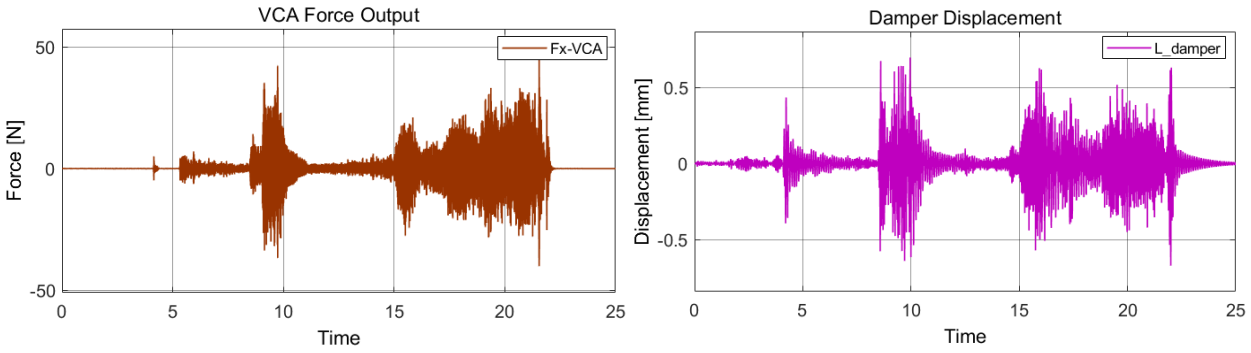

(a) *(b)*

Figure 5-13, Simulated VCA (a) applied force (b) displacement within its stroke under pure sinusoidal force input

Comparative Analysis and Observations

While each test exhibited a marked improvement in vibration levels compared to the uncontrolled baseline, the degree of suppression was strongly dependent on both the disturbance frequency content and the nature of the applied force profile. The actuator demonstrated optimal performance in low- and mid-frequency scenarios, where both the control effort and stroke requirements were well within allowable bounds. In contrast, control efficacy in Case 3, where high-frequency content was present, showed slight degradation due to increased force demand.

Across all cases, the actuator operated safely within its mechanical and electrical limits. These findings verify the initial design decisions, particularly the 40% safety margin in force capacity and the selection of a ±3.2 mm stroke. The control system proved capable of managing diverse operational demands without exceeding design thresholds.

Despite the structural similarity in the output plots (RMS vibration, FFT, actuator force, and displacement), the underlying system dynamics and required control effort varied substantially

with the disturbance profile. These results suggest that while a fixed-gain acceleration-feedback controller is effective across a broad range of operating conditions, future work could benefit from incorporating adaptive gain tuning or feedforward control strategies to improve responsiveness under high-frequency or multi-modal excitation. Such enhancements would further increase the robustness and efficiency of AVC implementation in real-world aerospace drilling tasks.

5.5 Summary

This chapter presented the development and verification of an Active Vibration Control (AVC) system integrated into the ACME end-effector, using a Voice Coil Actuator (VCA) to suppress process-induced vibrations during drilling operations. The control architecture featured two independent feedback loops: one based on acceleration measurements from a sensor mounted near the drilling nose, and another based on the real-time displacement of the VCA moving mass. This dual-feedback approach allowed precise control of the actuator's response to both transient and steady-state disturbances.

Prior to implementation, the required force output, stroke length, and moving mass of the VCA were estimated through dynamic simulations of the ACME system under drilling loads. These estimates guided the selection and configuration of the actuator to ensure compatibility with the dynamic range of expected disturbances. All simulated verifications were conducted with strict adherence to the actuator's physical limitations, including force, stroke, and bandwidth constraints. Verification was performed under step force input, controlled sinusoidal excitations and actual drilling conditions, and the AVC system consistently reduced vibration amplitudes. These results confirmed the effectiveness of the VCA-based AVC strategy in improving the dynamic stability and machining precision of a lightweight, flexible robotic system such as ACME.

6 Conclusion and Future Research Directions

This thesis presented the design, development, and verification of ACME (Advanced Collaborative Multifunctional End-Effector), an innovative robotic drilling tool specifically tailored for aerospace manufacturing. ACME effectively addresses the critical requirements of high precision, flexibility, safety, and cost-efficiency within collaborative robotic environments. Through systematic engineering, it integrates precise linear and rotational movements, robust clamping mechanisms, and advanced vibration control strategies, significantly improving upon existing automated drilling solutions.

The successful development and verification of ACME's prototype demonstrated its capability to achieve targeted performance benchmarks, including a clamping force exceeding 1000 N, rapid drilling cycles, and precise workspace coverage suitable for aerospace components. The implemented CoreXY mechanism allowed for efficient planar movements, while passive normality compensation ensured accurate drilling alignment on double-curvature surfaces. Despite minor variations in hole quality compared to CNC benchmarks, the results remained within acceptable aerospace standards.

The comprehensive dynamic modelling and experimental verifications conducted provided critical insights into the system's structural behaviour, including joint flexibility and vibration response. Moreover, integrating an active vibration control (AVC) system utilizing voice coil actuators (VCAs) effectively mitigated operational vibrations, thereby enhancing precision and reliability in drilling tasks.

Future research directions could significantly enhance ACME’s capabilities and application scope. Potential advancements include refining active vibration control algorithms for more diverse

operational conditions, optimizing structural design for enhanced rigidity without sacrificing payload compatibility, and further developing the digital twin model for real-time predictive control and maintenance. Additionally, exploring multi-sensor integration for improved positional accuracy and adaptive control, as well as extending ACME's functionalities to broader robotic applications beyond aerospace manufacturing, represents promising avenues for continued innovation.

Bibliography

[1] B. Luo, K. Zhang, S. Liu, H. Cheng, and R. Wang, “Investigation on the interface damage in drilling low-stiffness CFRP/Ti stacks,” *Chin. J. Aeronaut.*, vol. 32, no. 9, pp. 2211–2221, Sep. 2019, doi: 10.1016/j.cja.2019.04.017.

[2] M. Aamir, “Simultaneous machining of aerospace structural materials using poly-drills”.

[3] F. Bañon, A. Sambruno, M. Batista, S. R. Fernandez-Vidal, and J. Salguero, “Study of the one-shot drilling of CFRP/Ti6Al4V stacks with a double tip angle cutting-tool geometry,” presented at the PROCEEDINGS OF THE 22ND INTERNATIONAL ESAFORM CONFERENCE ON MATERIAL FORMING: ESAFORM 2019, Vitoria-Gasteiz, Spain, 2019, p. 080010. doi: 10.1063/1.5112618.

[4] C. Lei, C. Li, Y. Bi, and J. Li, “The optimal clamping force option for robotic drilling of stacked aluminum sheets based on shell theory,” *Adv. Mech. Eng.*, vol. 9, no. 3, p. 1687814017695048, Mar. 2017, doi: 10.1177/1687814017695048.

[5] A. Pardo, “Fundamental investigation of the drilling of multi- material aerospace stacks to aid adaptive drilling”.

[6] L. Jie and J. Shu-Hui, “The Study of Design Method for Robotic Drill End Effector,” *Procedia Eng.*, vol. 174, pp. 206–210, 2017, doi: 10.1016/j.proeng.2017.01.120.

[7] Z. Shi, P. Yuan, Q. Wang, D. Chen, and T. Wang, “New design of a compact aero-robotic drilling end effector: An experimental analysis,” *Chin. J. Aeronaut.*, vol. 29, no. 4, pp. 1132–1141, Aug. 2016, doi: 10.1016/j.cja.2015.11.001.

[8] D. Chen, P. Yuan, T. Wang, Y. Cai, and H. Tang, “A Normal Sensor Calibration Method Based on an Extended Kalman Filter for Robotic Drilling,” *Sensors*, vol. 18, no. 10, p. 3485, Oct. 2018, doi: 10.3390/s18103485.

[9] P. Yuan, D. Chen, T. Wang, S. Cao, Y. Cai, and L. Xue, “A compensation method based on extreme learning machine to enhance absolute position accuracy for aviation drilling robot,” *Adv. Mech. Eng.*, vol. 10, no. 3, p. 168781401876341, Mar. 2018, doi: 10.1177/1687814018763411.

[10] W. Tian, W. Zhou, W. Zhou, W. Liao, and Y. Zeng, “Auto-normalization algorithm for robotic precision drilling system in aircraft component assembly,” *Chin. J. Aeronaut.*, vol. 26, no. 2, pp. 495–500, Apr. 2013, doi: 10.1016/j.cja.2013.02.029.

[11] S. Laporte, E. Gueydon, A. Auffret, and C. De Castelbajac, “A New Robotic Vibration-Drilling Process,” *SAE Int. J. Mater. Manuf.*, vol. 8, no. 1, pp. 56–62, Sep. 2014, doi: 10.4271/2014-01-2258.

[12] B. Marguet *et al.*, “Crawler Robots for Drilling and Fastener Installation: An Innovative Breakthrough in Aerospace Automation,” presented at the Aerospace Manufacturing and Automated Fastening Conference & Exhibition, Sep. 2008, pp. 2008-01–2292. doi: 10.4271/2008-01-2292.

[13] P. Cirillo, A. Marino, C. Natale, E. Di Marino, P. Chiacchio, and G. De Maria, “A low-cost and flexible solution for one-shot cooperative robotic drilling of aeronautic stack materials,” *IFAC-Pap.*, vol. 50, no. 1, pp. 4602–4609, Jul. 2017, doi: 10.1016/j.ifacol.2017.08.1013.

[14] “Mini Flextrack 1.0 | MTM Robotics.” Accessed: Jan. 23, 2023. [Online]. Available: https://mtmrobotics.com/our-offerings/products/flextrack-technologies/mini-flextrack-1-0/

[15] A. Bicchi and G. Tonietti, “Design, Realization and Control of Soft Robot Arms for Intrinsically Safe Interaction with Humans”.

[16] R. Weitschat, J. Vogel, S. Lantermann, and H. Hoppner, “End-effector airbags to accelerate human-robot collaboration,” in *2017 IEEE International Conference on Robotics and Automation (ICRA)*, Singapore, Singapore: IEEE, May 2017, pp. 2279–2284. doi: 10.1109/ICRA.2017.7989262.

[17] M. Zinn, B. Roth, O. Khatib, and J. K. Salisbury, “A New Actuation Approach for Human Friendly Robot Design,” *Int. J. Robot. Res.*, vol. 23, no. 4–5, pp. 379–398, Apr. 2004, doi: 10.1177/0278364904042193.

[18] K. Merckaert, A. De Beir, N. Adriaens, I. El Makrini, R. Van Ham, and B. Vanderborght, “Independent load carrying and measurement manipulator robot arm for improved payload to mass ratio,” *Robot. Comput.-Integr. Manuf.*, vol. 53, pp. 135–140, Oct. 2018, doi: 10.1016/j.rcim.2018.04.001.

[19] G. Van de Perre, T. Hubert, T. Verstraten, and B. Vanderborght, “Investigating the potential of flexible links for increased payload to mass ratios for collaborative robotics,” *IEEE Access*, vol. 11, pp. 15981–15995, Feb. 2023, doi: 10.1109/ACCESS.2023.3244402.

[20] N. Doiron and A. Gallant, “Increasing the Payload of a 7DOF Cobot,” 2023, pp. 101–110. doi: 10.1007/978-3-031-29815-8_11.

[21] V. Arakelian, “A COBOTIC AND FLEXIBLE SOLUTION FOR HANDLING OF HEAVY LOADS,” 2022.

[22] H. Jin, M. Luo, S. Lu, Q. He, and Y. Lin, “Design and Analysis of a Novel Variable Stiffness Joint for Robot,” *Actuators*, vol. 12, no. 1, Art. no. 1, Jan. 2023, doi: 10.3390/act12010010.

[23] J. J. Craig, “Mechanics and Control Third Edition”.

[24] Z. Wang and P. Keogh, “Active Vibration Control for Robotic Machining,” in *Volume 2: Advanced Manufacturing*, Tampa, Florida, USA: American Society of Mechanical Engineers, Nov. 2017, p. V002T02A079. doi: 10.1115/IMECE2017-71670.

[25] H. N. Huynh and Y. Altintas, “Modeling the Dynamics of Five-Axis Machine Tool Using the Multibody Approach,” *J. Manuf. Sci. Eng.*, vol. 143, no. 021012, Dec. 2020, doi: 10.1115/1.4048854.

[26] M. F. Zaeh, R. Kleinwort, P. Fagerer, and Y. Altintas, “Automatic tuning of active vibration control systems using inertial actuators,” *CIRP Ann.*, vol. 66, no. 1, pp. 365–368, 2017, doi: 10.1016/j.cirp.2017.04.051.

[27] H. Chen and K. Ahmadi, “Estimating pose-dependent FRF in machining robots using multibody dynamics and Gaussian Process Regression,” *Robot. Comput.-Integr. Manuf.*, vol. 77, p. 102354, Oct. 2022, doi: 10.1016/j.rcim.2022.102354.

[28] L. Zhang, C. Zhao, F. Qian, J. S. Dhupia, and M. Wu, “A Variable Parameter Ambient Vibration Control Method Based on Quasi-Zero Stiffness in Robotic Drilling Systems,” *Machines*, vol. 9, no. 3, p. 67, Mar. 2021, doi: 10.3390/machines9030067.

[29] T. Kumar, R. Kumar, and S. C. Jain, “Numerical Investigation of Semi-active Torsional Vibration Control of Heavy Turbo-generator Rotor using Magnetorheological Fluid Dampers,” *J. Vib. Eng. Technol.*, vol. 9, no. 5, pp. 967–981, Jul. 2021, doi: 10.1007/s42417-020-00276-5.

[30] D. K. Thomsen, R. Søe-Knudsen, O. Balling, and X. Zhang, “Vibration control of industrial robot arms by multi-mode time-varying input shaping,” *Mech. Mach. Theory*, vol. 155, p. 104072, Jan. 2021, doi: 10.1016/j.mechmachtheory.2020.104072.

[31] C. Yue, H. Gao, X. Liu, S. Y. Liang, and L. Wang, “A review of chatter vibration research in milling,” *Chin. J. Aeronaut.*, vol. 32, no. 2, pp. 215–242, Feb. 2019, doi: 10.1016/j.cja.2018.11.007.

[32] N. Martinez, J. Chambers, M. Gegel, E. Schmierer, and A. Scheinker, “Drill Vibration Suppression Through Phase-Locked Loop Control,” in *Experimental Techniques, Rotating Machinery, and Acoustics, Volume 8*, J. De Clerck, Ed., Cham: Springer International Publishing, 2015, pp. 11–20. doi: 10.1007/978-3-319-15236-3_2.

[33] A. Rashid and C. M. Nicolescu, “Design and implementation of tuned viscoelastic dampers for vibration control in milling,” *Int. J. Mach. Tools Manuf.*, vol. 48, no. 9, pp. 1036–1053, Jul. 2008, doi: 10.1016/j.ijmachtools.2007.12.013.

[34] J. Burtscher and J. Fleischer, “Adaptive tuned mass damper with variable mass for chatter avoidance,” *CIRP Ann.*, vol. 66, no. 1, pp. 397–400, 2017, doi: 10.1016/j.cirp.2017.04.059.

[35] L. Yuan, S. Sun, Z. Pan, D. Ding, O. Gienke, and W. Li, “Mode coupling chatter suppression for robotic machining using semi-active magnetorheological elastomers absorber,” *Mech. Syst. Signal Process.*, vol. 117, pp. 221–237, Feb. 2019, doi: 10.1016/j.ymssp.2018.07.051.

[36] C. Wang, H. Qu, H. Xu, and Z. Wang, “Influence of stell plate surface roughness on coal freezing adhesive strength,” *Jixie QiangduJournal Mech. Strength*, vol. 39, no. 1, pp. 53–56, 2017, doi: 10.16579/j.issn.1001.9669.2017.01.009.

[37] M. Newman and M. Khoshdarregi, “Automatic Structural Identification and Vibration Suppression of Industrial Robots using a Custom Active Damper,” in *2022 22nd International Conference on Control, Automation and Systems (ICCAS)*, Jeju, Korea, Republic of: IEEE, Nov. 2022, pp. 1033–1038. doi: 10.23919/ICCAS55662.2022.10003880.

[38] “CoreXY | Cartesian Motion Platform.” Accessed: Oct. 19, 2024. [Online]. Available: https://corexy.com/reference.html

Appendix A: Main AssemblyACME-00-00-00

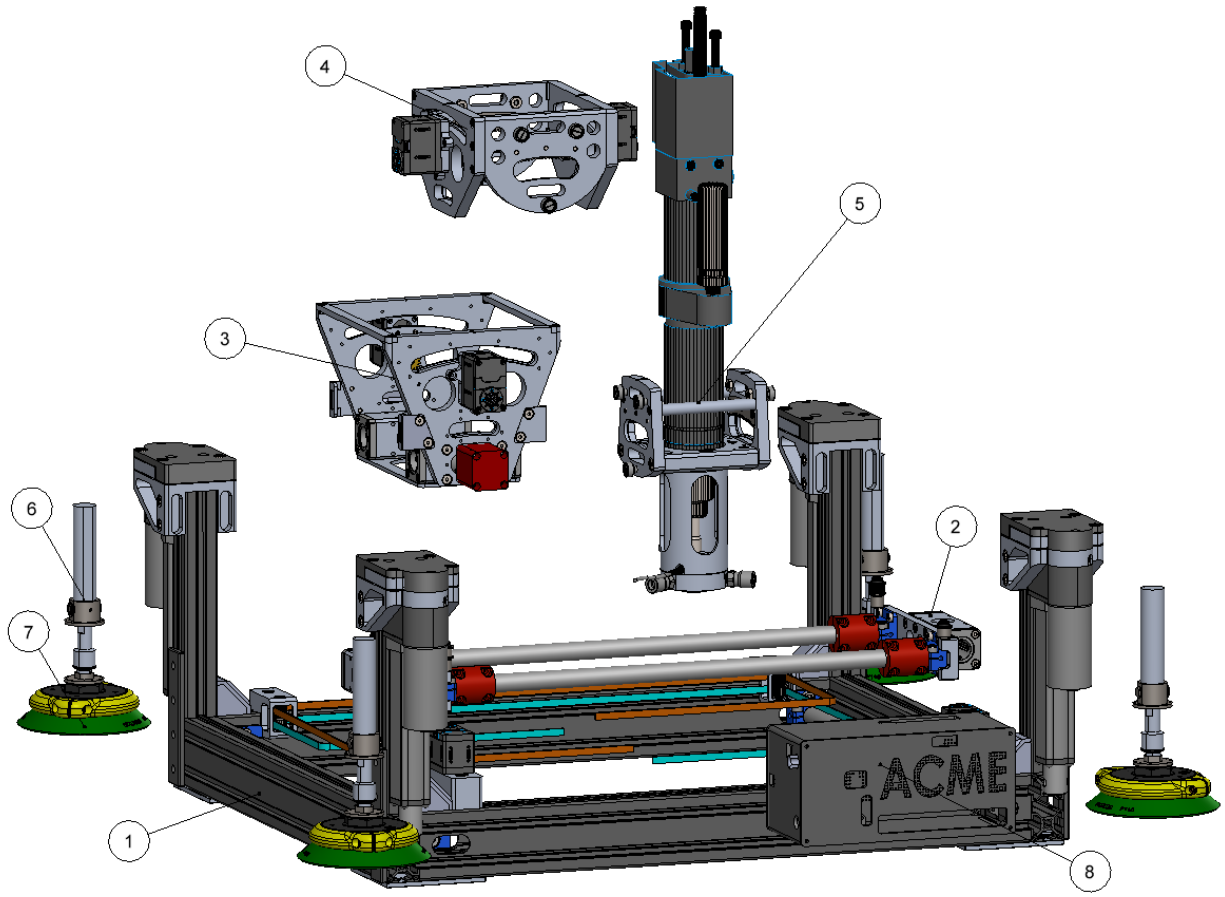

ITEM NO.	PART NUMBER	DESCRIPTION	QTY.
1	ACME-01-00-00	Outer frame	1
2	ACME-02-00-00	Y-axis carriage	1
3	ACME-03-00-00	X-axis carriage	1
4	ACME-04-00-00	B (Pitch) rotation axis	1
5	ACME-05-00-00	A (Roll) rotation axis	1
6	ACME-06-00-00	Attached to item #7 in real world	4
7	ACME-07-00-00	Suction cups	4
8	Box	Control and Electronics Box	1

Appendix B: Control and Electronics Box

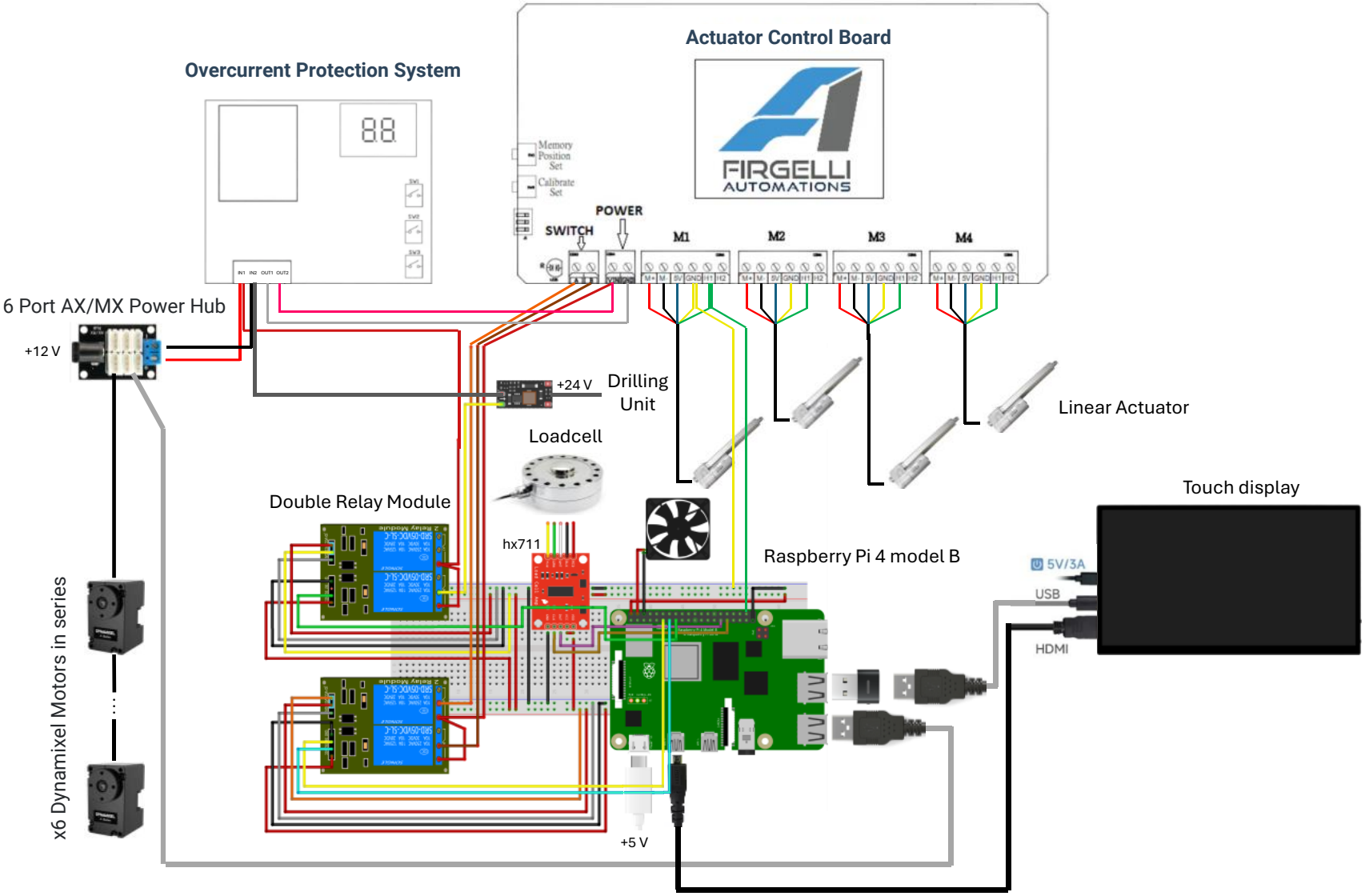

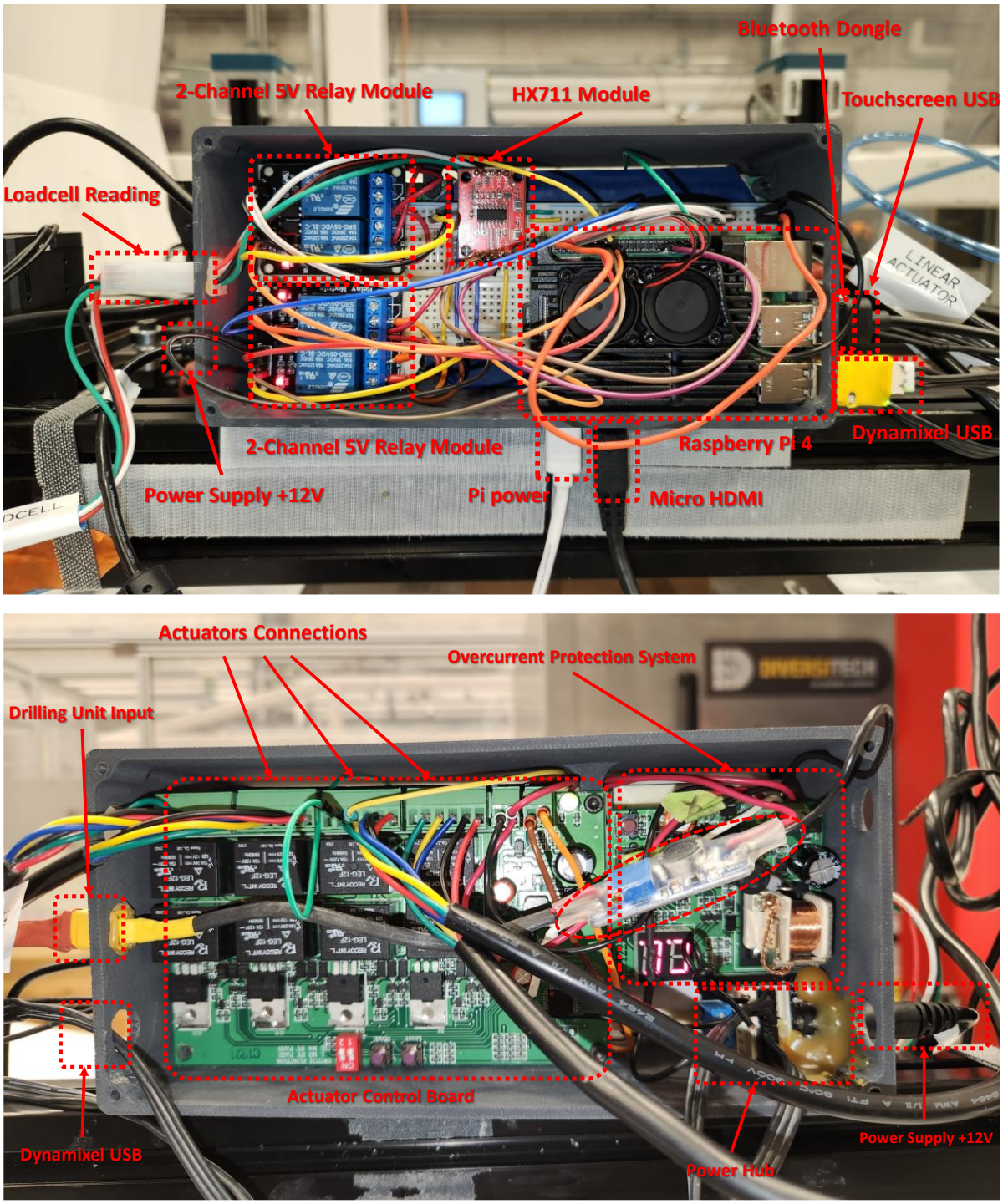

Figure 0-1 Overview of electronic components and connections on both sides of the electronic box

Appendix C: System Identification Measurements Setup

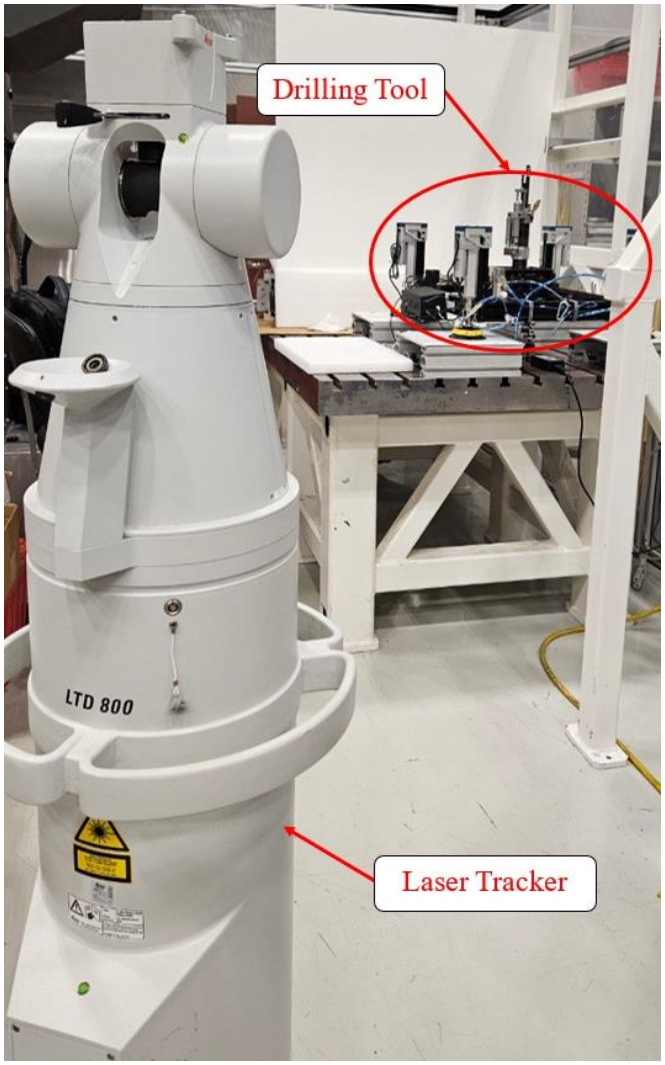

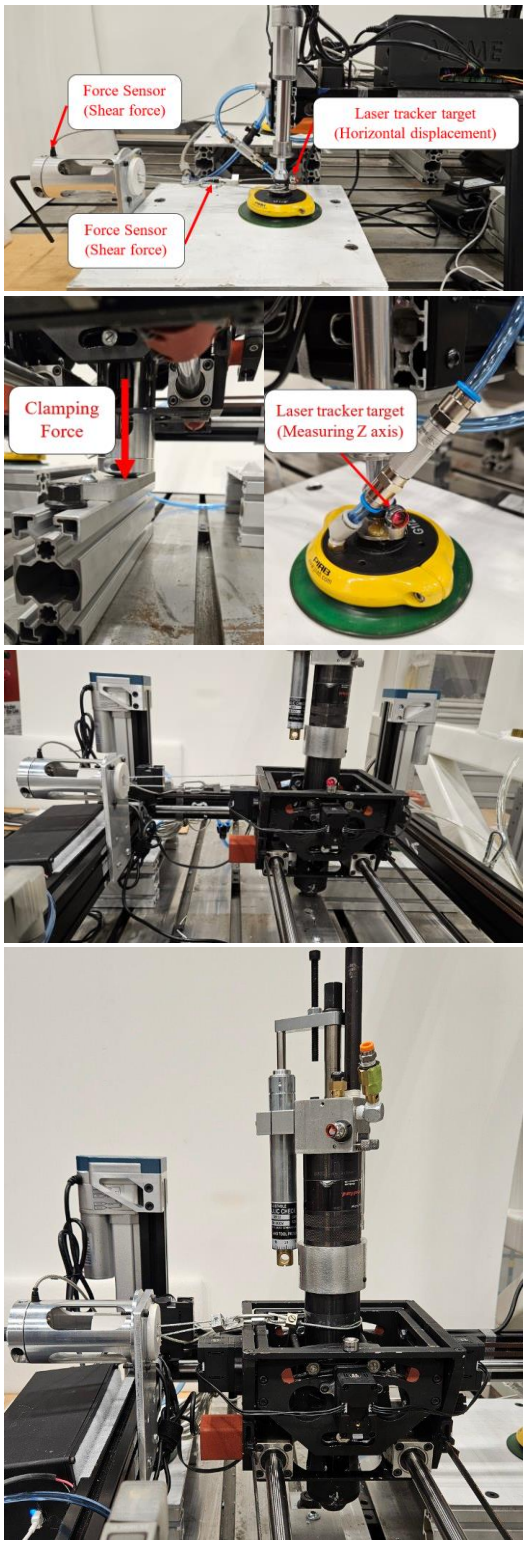

Displacement of the suction cups under shear (horizontal) load										
Test 1					Test 2					
Force	Pose [X, Y, Z]			Displacement	Force	Pose [X, Y, Z]			Displacement	Point
F [kg]	X [mm]	Y [mm]	Z [mm]	D [mm]	F [kg]	X [mm]	Y [mm]	Z [mm]	D [mm]	
0	638.4122	2174.9328	-304.9279	0	0.13	643.0645	2174.5322	-304.8546	0	P1
2.04	638.4229	2175.0224	-304.9118	0.0916689	2.14	643.0739	2174.5588	-304.8544	0.028203	P2
6	638.4418	2175.1789	-304.8855	0.2514714	6.14	643.0949	2174.7424	-304.8208	0.215052	P3
10.09	638.4667	2175.3710	-304.8500	0.4484189	10.12	643.1198	2174.9436	-304.7870	0.42054	P4
15.08	638.5103	2175.6347	-304.8041	0.7194528	15.06	643.1506	2175.1892	-304.7462	0.671410	P5
20.01	638.5556	2175.9758	-304.7536	0.6188002	20.04	643.1852	2175.4584	-304.6999	0.526289	P6
24.93	638.6300	2176.4833	-304.6712	1.5866641	25.09	643.2154	2175.6838	-304.6531	1.178793	P7
30.43	638.7005	2176.9367	-304.6028	2.0504756	30.02	643.2571	2175.9978	-304.5760	1.504203	P8

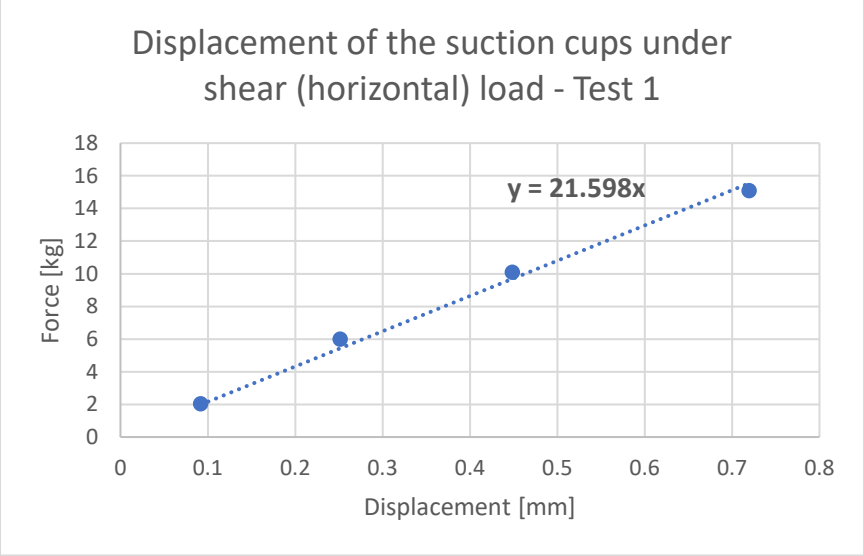

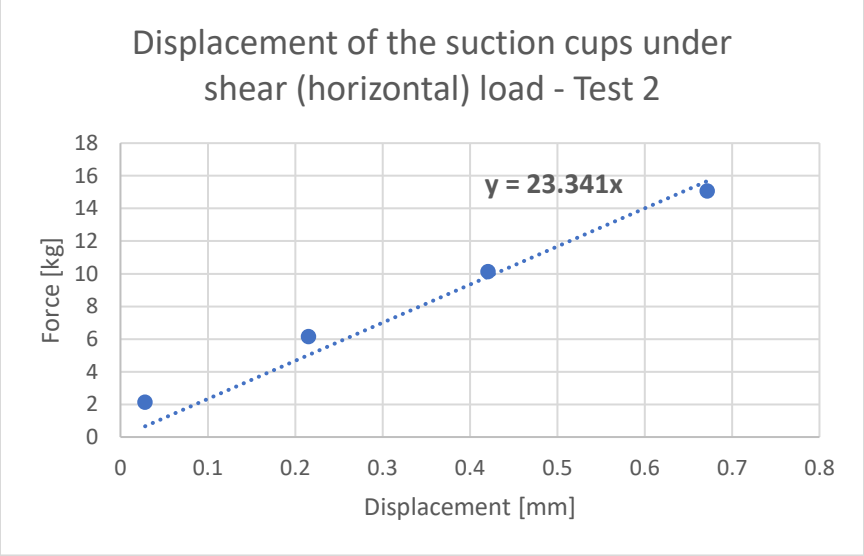

Appendix

Displacement of the suction cups under normal (vertical) load										
Test 1					Test 2					Point
Force	Pose [X, Y, Z]			Displacement	Force	Pose [X, Y, Z]			Displacement	
F [kg]	X [mm]	Y [mm]	Z [mm]	D [mm]	F [kg]	X [mm]	Y [mm]	Z [mm]	D [mm]	
24.63	-89.0006	2042.7988	-323.3187	0	19.84	-89.0032	2042.7886	-323.3328	0	PZ-1
27.88	-88.9920	2042.7945	-323.2995	0.0214958	27.67	-88.9882	2042.7860	-323.3139	0.0243036	PZ-2
37.8	-88.972	2042.7781	-323.2461	0.0806618	41.82	-88.9713	2042.7717	-323.2543	0.0863960	PZ-3
54.53	-88.9509	2042.7628	-323.1706	0.1603242	52.38	-88.9544	2042.7637	-323.1879	0.1549587	PZ-4
67.18	-88.9361	2042.7532	-323.1134	0.2199811	65.56	-88.9363	2042.7515	-323.1323	0.2146318	PZ-5
73.42	-88.9331	2042.7548	-323.0877	0.0850803	79.29	-88.9186	2042.7524	-323.0587	0.1345617	PZ-6
91.36	-88.9162	2042.747	-322.9800	0.3528575	88.67	-88.9056	2042.7468	-323.0162	0.3339133	PZ-7
105.58	-88.8778	2042.7353	-322.9100	0.4314040	98.76	-88.8808	2042.7408	-322.9474	0.4072365	PZ-8

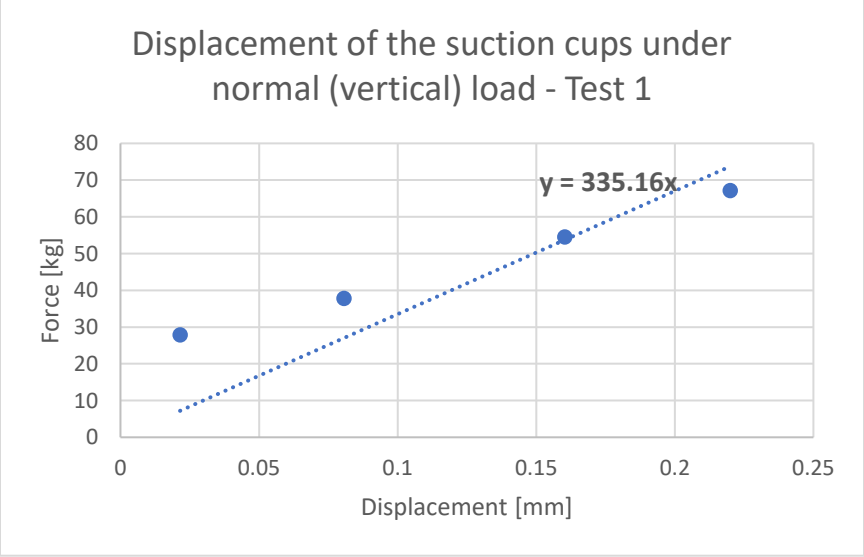

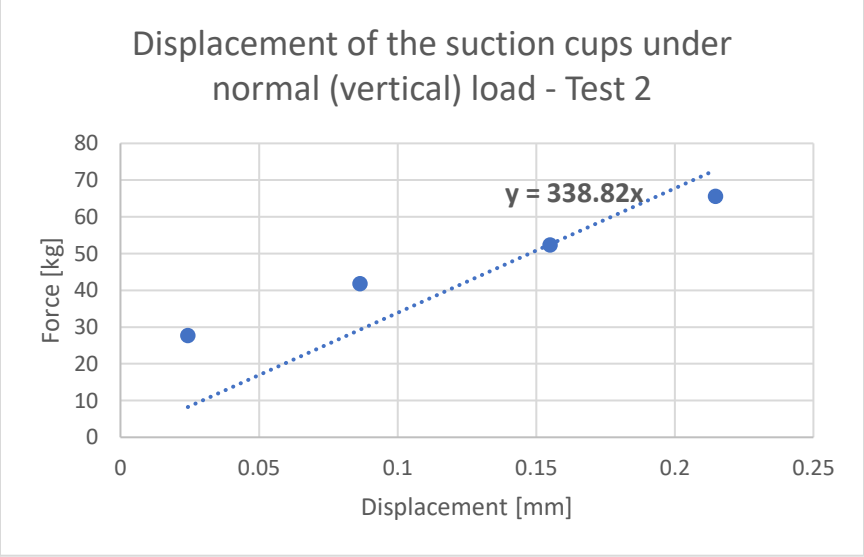

Axis X - Motor On - No Clamping										
Test 1-1					Test 1-2					Point
Force	Pose [X, Y, Z]			Displacement	Force	Pose [X, Y, Z]			Displacement	
F [kg]	X [mm]	Y [mm]	Z [mm]	D [mm]	F [kg]	X [mm]	Y [mm]	Z [mm]	D [mm]	
0.03	251.4740	2407.6770	-86.9078	0	0.06	251.3293	2408.0859	-86.8991	0	PX1-1
2	251.3823	2407.8479	-86.8867	0.195107	2.05	251.2521	2408.2307	-86.8859	0.1645916	PX1-2
6.04	251.2148	2408.2224	-86.8726	0.604911	6.15	251.1079	2408.5012	-86.8648	0.4718531	PX1-3
10.08	251.0245	2408.5815	-86.8540	1.011500	10.12	250.9649	2408.7722	-86.8569	0.7781355	PX1-4
15.1	250.6761	2409.1738	-86.8333	1.697848	15.06	250.6794	2409.2434	-86.8340	1.3290246	PX1-5
20.1	250.3982	2409.6210	-86.8137	1.214321	20.3	250.2735	2409.8859	-86.8159	1.3115568	PX1-6
25.24	250.0323	2410.2561	-86.8161	2.956155	25.06	249.9548	2410.3500	-86.7991	2.6505951	PX1-7
30.17	249.4526	2410.9133	-86.7822	3.817822	30.06	249.4842	2410.8840	-86.7978	3.3531582	PX1-8

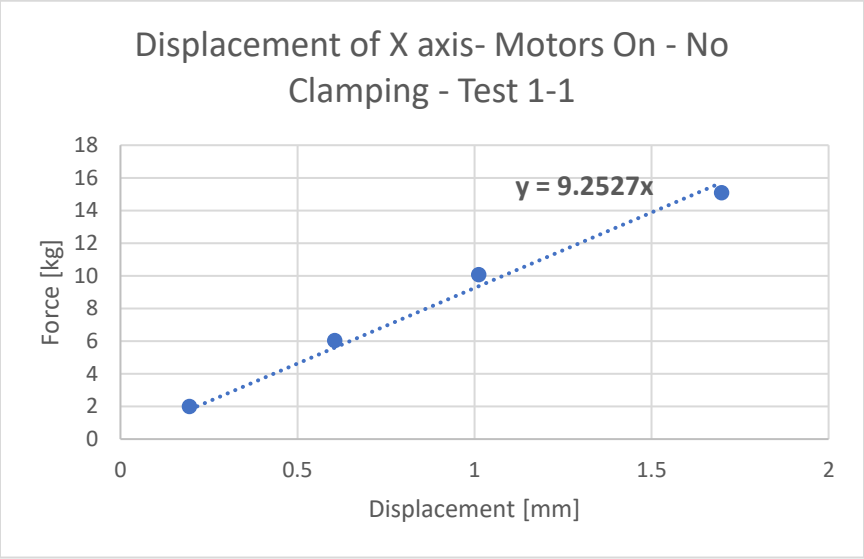

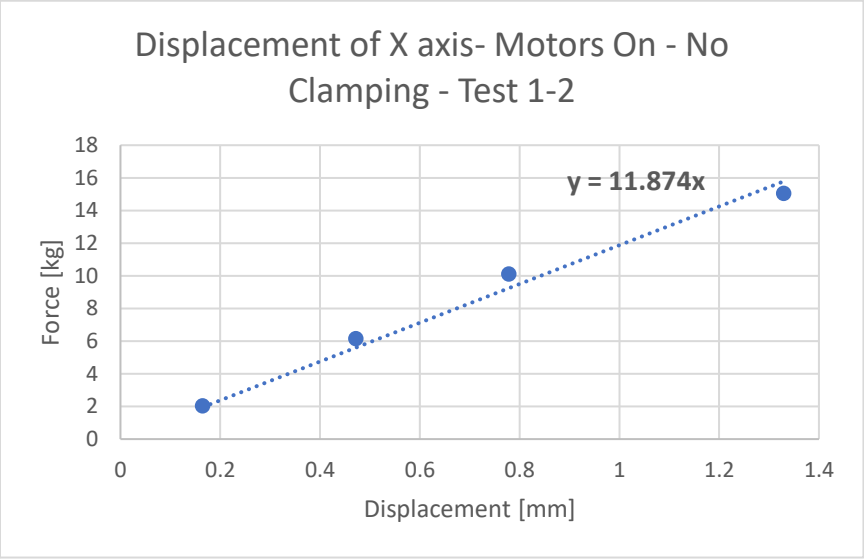

Appendix

Axis X - Motor On - With Clamping										
Test 2-1					Test 2-2					Point
Force	Pose [X, Y, Z]			Displacement	Force	Pose [X, Y, Z]			Displacement	
F [kg]	X [mm]	Y [mm]	Z [mm]	D [mm]	F [kg]	X [mm]	Y [mm]	Z [mm]	D [mm]	
0	149.6261	2384.5761	-162.9403	0	0	148.1101	2386.3518	-162.8764	0	PX2-1
2	149.6152	2384.5881	-162.9442	0.0166651	2	148.1005	2386.3679	-162.8731	0.0190606	PX2-2
6	149.5925	2384.6191	-162.9377	0.0546171	6	148.0685	2386.4016	-162.8728	0.06498613	PX2-3
10	149.5211	2384.7121	-162.9267	0.1723622	10.15	148.0110	2386.4626	-162.8702	0.14884482	PX2-4
15	149.3610	2384.8068	-162.9163	0.3522612	15.1	147.8238	2386.6228	-162.8506	0.39509980	PX2-5
20.3	149.2182	2384.9294	-162.9069	0.3733031	20	147.6614	2386.7614	-162.8289	0.46172958	PX2-6
25.12	148.9364	2385.1501	-162.8757	0.8996110	25	147.5044	2386.9147	-162.8129	0.82937132	PX2-7
30.63	147.3334	2387.1091	-162.7824	3.4201772	30	146.0677	2388.7683	-162.7957	3.16507913	PX2-8

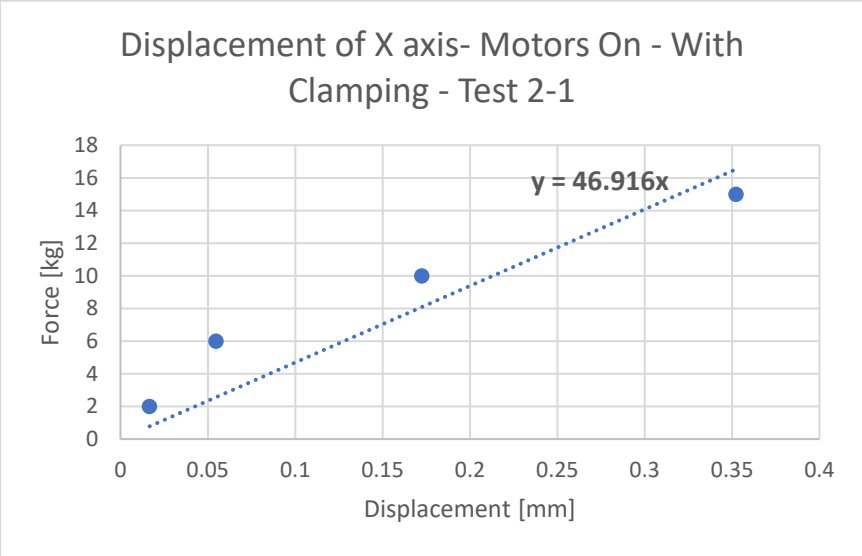

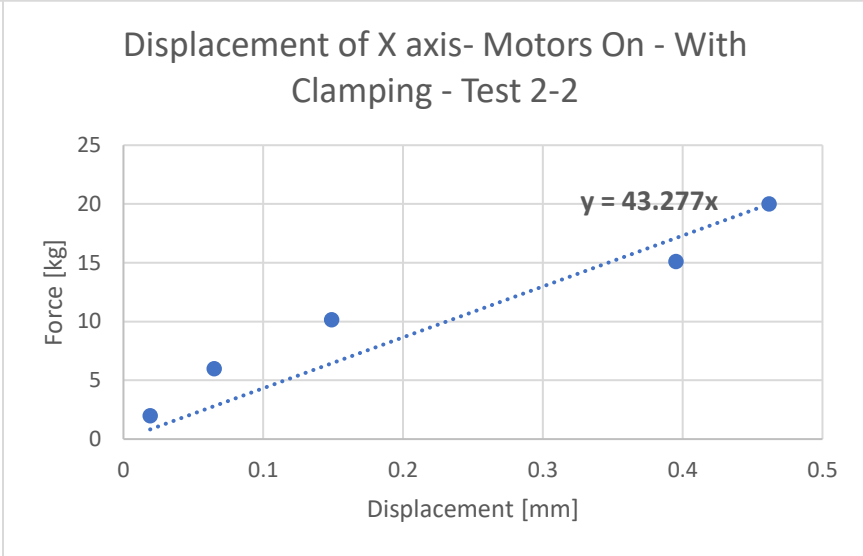

Axis Y - Motor On - No Clamping										
Test 1-1					Test 1-2					Point
Force	Pose [X, Y, Z]			Displacement	Force	Pose [X, Y, Z]			Displacement	
F [kg]	X [mm]	Y [mm]	Z [mm]	D [mm]	F [kg]	X [mm]	Y [mm]	Z [mm]	D [mm]	
0	122.534447	2460.266602	-101.038567	0	0				0	PY1-1
2	122.235191	2460.062256	-101.034637	0.362390516	2				0	PY1-2
6	121.60701	2459.668701	-101.025742	1.103534991	6				0	PY1-3
10	121.05851	2459.335693	-101.027611	1.745021956	10				0	PY1-4
15	120.145996	2458.842041	-101.043617	2.781024582	15				0	PY1-5
20				2464.385074	20				0	PY1-6
25				2465.387441	25				0	PY1-7
30				2465.387441	30				0	PY1-8

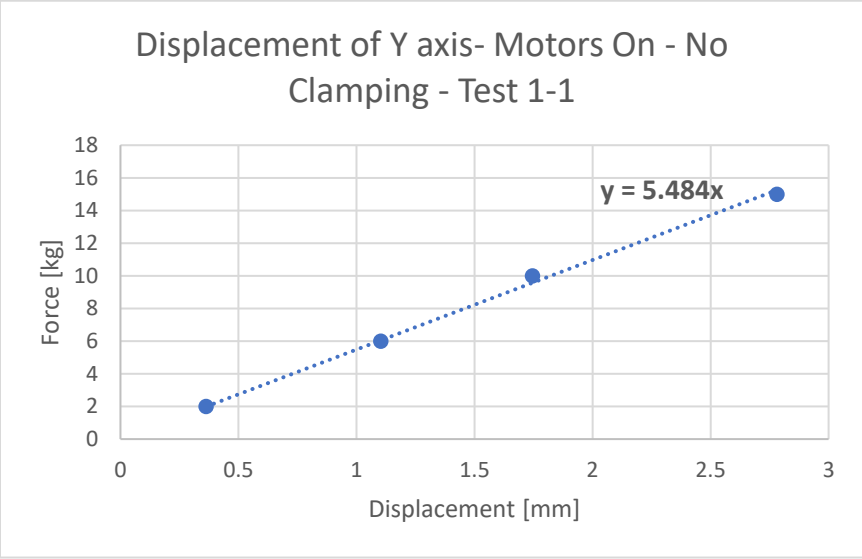

Axis Y - Motor On - With Clamping										
Test 2-1					Test 2-2					Point
Force	Pose [X, Y, Z]			Displacement	Force	Pose [X, Y, Z]			Displacement	
F [kg]	X [mm]	Y [mm]	Z [mm]	D [mm]	F [kg]	X [mm]	Y [mm]	Z [mm]	D [mm]	
0	121.8245	2458.1262	-163.1404	0	0	121.6933	2458.0332	-163.1480	0	PY2-1
2	121.7330	2458.0595	-163.1407	0.11317	2	121.6177	2457.9692	-163.1528	0.09911	PY2-2
6	121.5704	2457.9404	-163.1451	0.31478	6	121.4516	2457.8581	-163.1534	0.29842	PY2-3
10	121.3465	2457.7868	-163.1358	0.58617	10	121.2620	2457.7368	-163.1508	0.52331	PY2-4
15	121.0562	2457.5871	-163.1284	0.93859	15	120.9848	2457.5332	-163.1313	0.86733	PY2-5
20	120.6449	2457.2846	-163.1306	0.86285	20	120.6865	2457.3151	-163.1369	0.71355	PY2-6
25	120.3120	2457.0363	-163.1180	1.86435	25	120.3559	2457.0747	-163.1216	1.64561	PY2-7
30	119.9768	2456.7893	-163.1082	2.28084	30	120.0402	2456.8398	-163.1230	2.03898	PY2-8

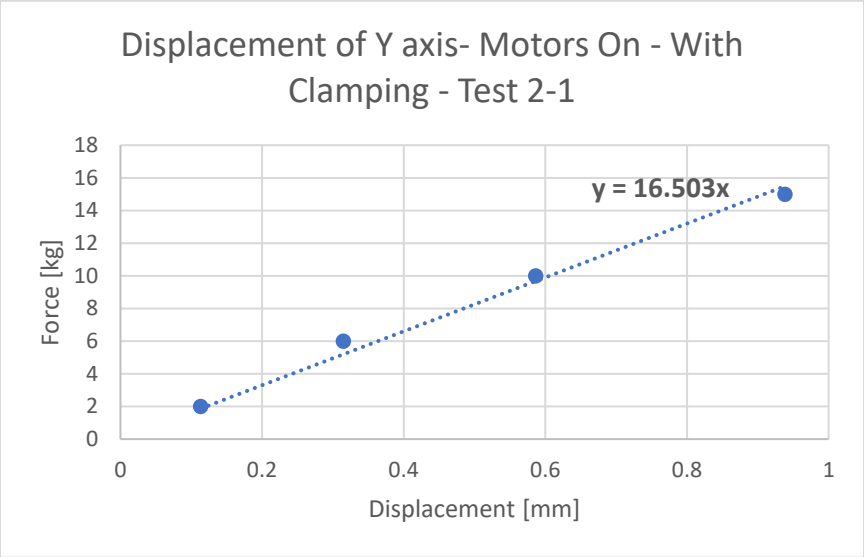

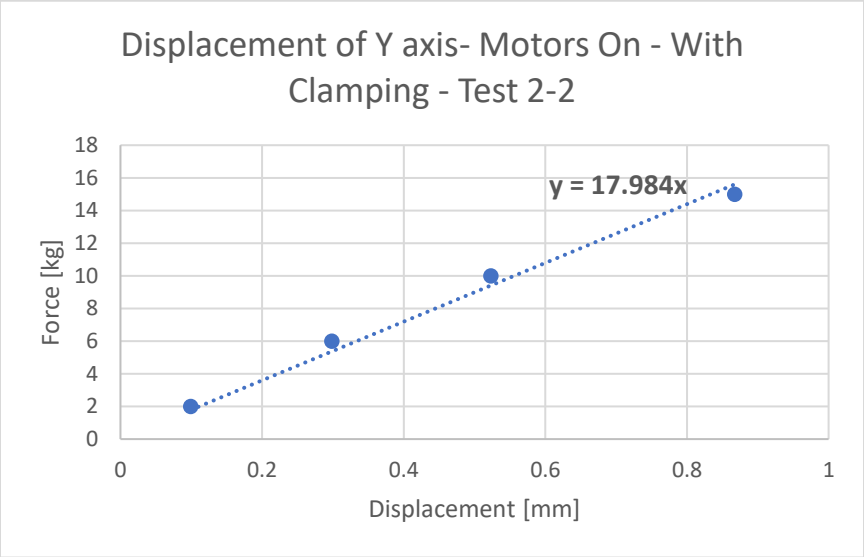

A&B Axes - Motor On - No Clamping										
Test 1-1					Test 1-2					Point
Force	Pose [X, Y, Z]			Displacement	Force	Pose [X, Y, Z]			Displacement	
F [kg]	X [mm]	Y [mm]	Z [mm]	D [mm]	F [kg]	X [mm]	Y [mm]	Z [mm]	D [mm]	
0	-8.8627	2427.8906	71.4636	0	0	-10.0393	2428.9069	71.5798	0	PA1-1
2	-9.5135	2427.3381	71.4769	0.85379	2	-10.5212	2428.3627	71.5818	0.72694	PA1-2
6	-10.7216	2426.2189	71.5586	2.50175	6	-11.6513	2427.2771	71.6406	2.29321	PA1-3
10	-11.1139	2425.7578	71.5501	3.10230	10	-12.5046	2426.5329	71.6545	3.42334	PA1-4
15	-11.7476	2425.1103	71.5526	4.00752	15	-12.7424	2426.2805	71.6335	3.76936	PA1-5
20	-12.2444	2424.4960	71.5544	1.69409	20	-12.9846	2426.1020	71.6287	0.64558	PA1-6
25	-12.3525	2424.3007	71.5502	5.00732	25	-13.3037	2425.8371	71.6242	4.481351	PA1-7
30	-12.6181	2423.9870	71.5351	5.41719	30	-13.6054	2425.5393	71.6215	4.905158	PA1-8

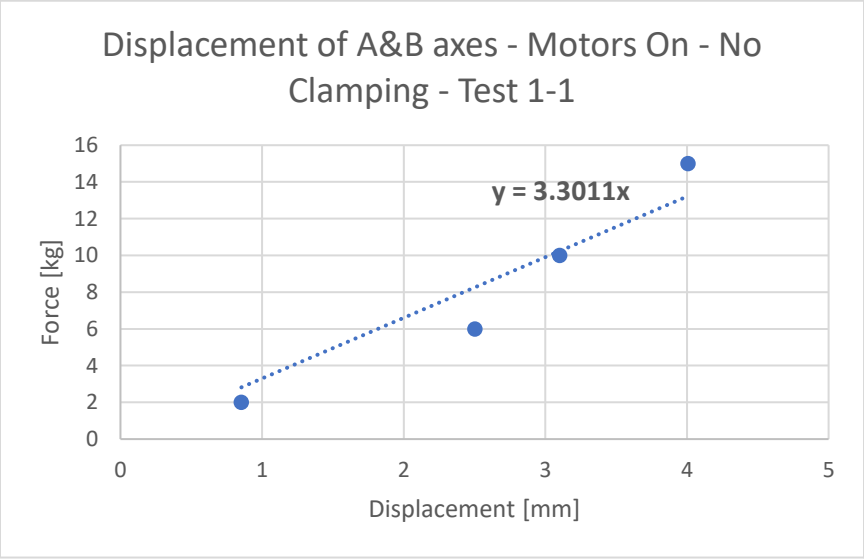

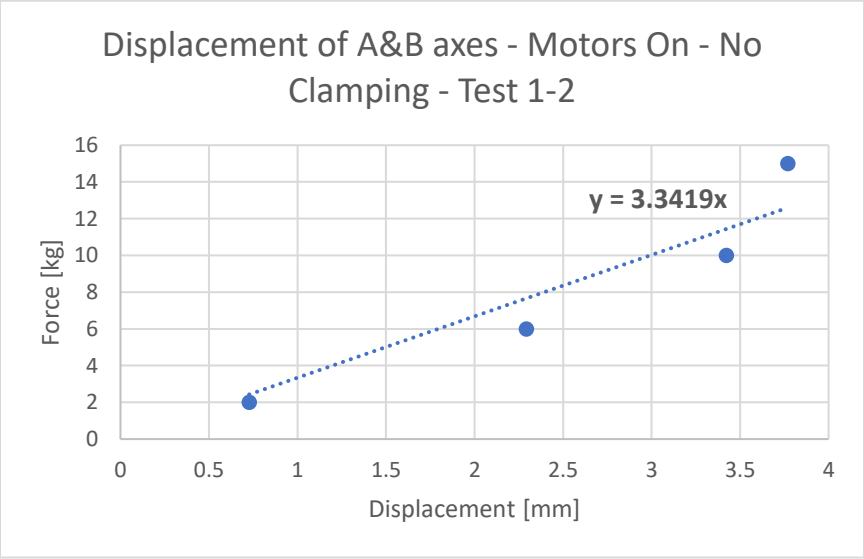

Appendix

A&B Axes - Motor On - With Clamping										
Test 2-1					Test 2-2					Point
Force	Pose [X, Y, Z]			Displacement	Force	Pose [X, Y, Z]			Displacement	
F [kg]	X [mm]	Y [mm]	Z [mm]	D [mm]	F [kg]	X [mm]	Y [mm]	Z [mm]	D [mm]	
0	-17.2492	2404.2204	6.9596	0	0	-18.0560	2403.7526	6.8983	0	PA2-1
2	-17.3722	2404.1320	6.9551	0.15153	2	-18.1553	2403.6772	6.8865	0.12526	PA2-2
6	-17.6472	2403.9504	6.9197	0.48259	6	-18.2607	2403.5966	6.8880	0.25756	PA2-3
10	-17.8314	2403.8137	6.9139	0.71165	10	-18.3780	2403.5124	6.8568	0.40387	PA2-4
15	-18.1965	2403.5656	6.8841	1.15407	15	-18.5504	2403.3781	6.8448	0.62248	PA2-5
20	-18.4638	2403.3801	6.8577	0.76884	20	-18.7215	2403.2275	6.8247	0.44737	PA2-6
25	-18.8552	2403.0722	6.8191	1.97920	25	-19.1058	2402.9360	6.7897	1.33445	PA2-7
30	-19.2757	2402.7675	6.7750	2.50037	30	-19.2835	2402.8107	6.7646	1.55296	PA2-8

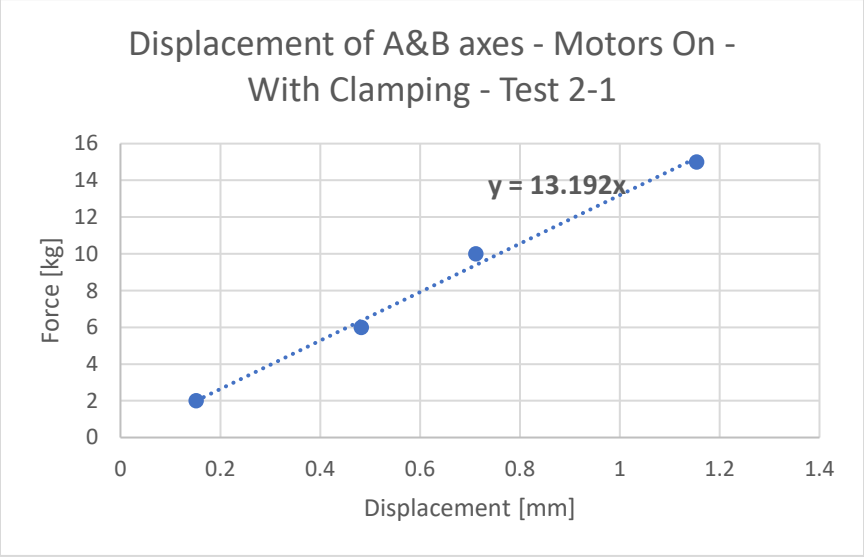

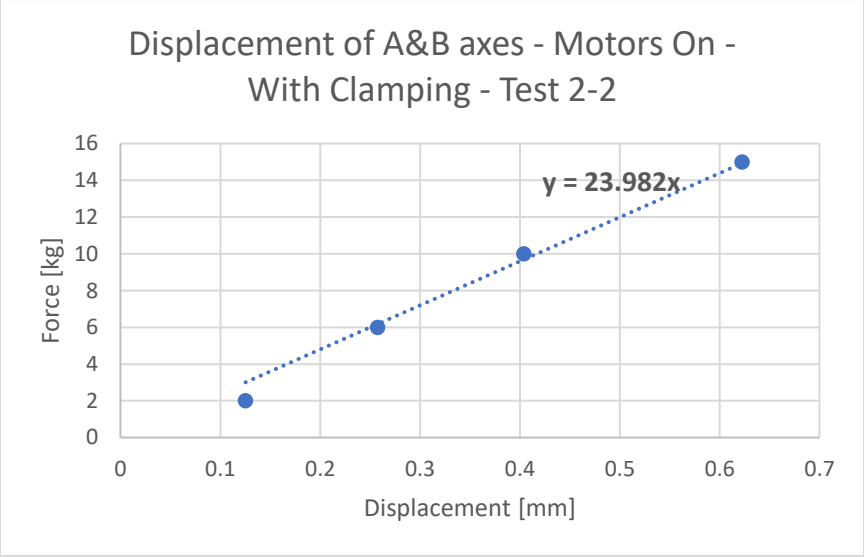

Appendix D: Simulink Model

Full Model

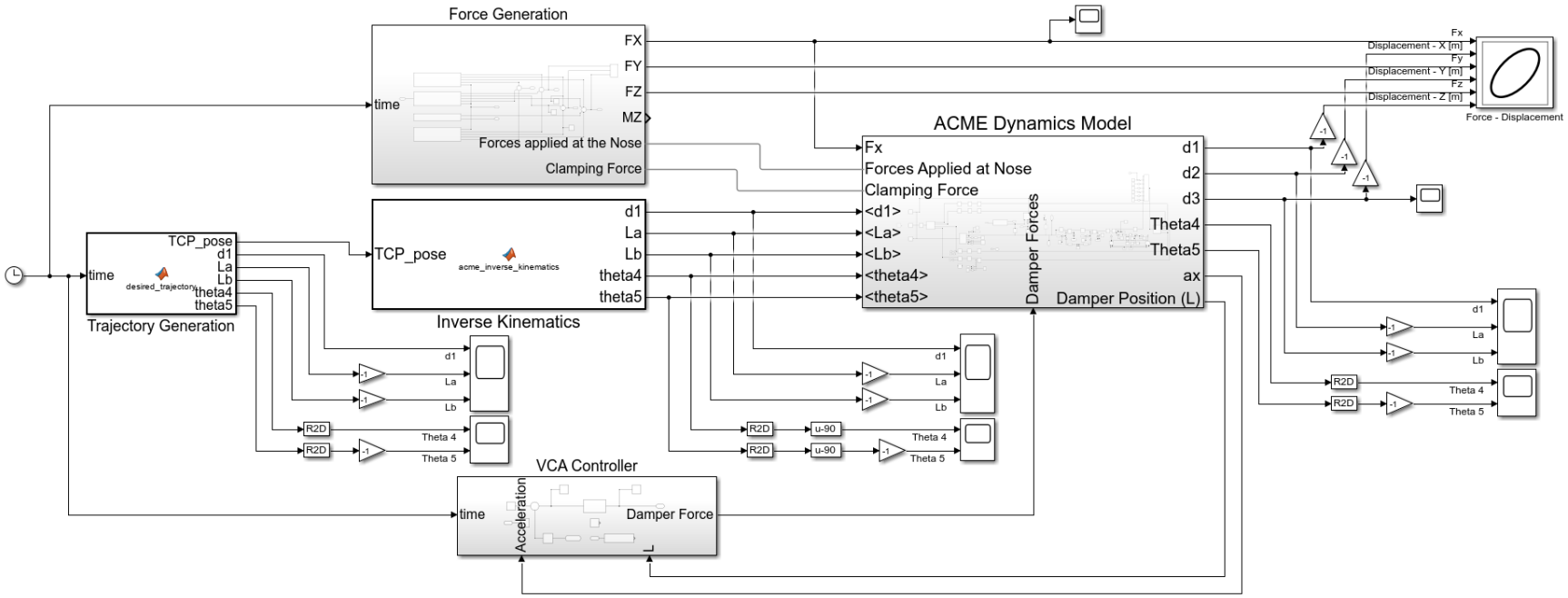

Mechanical Dynamics Model

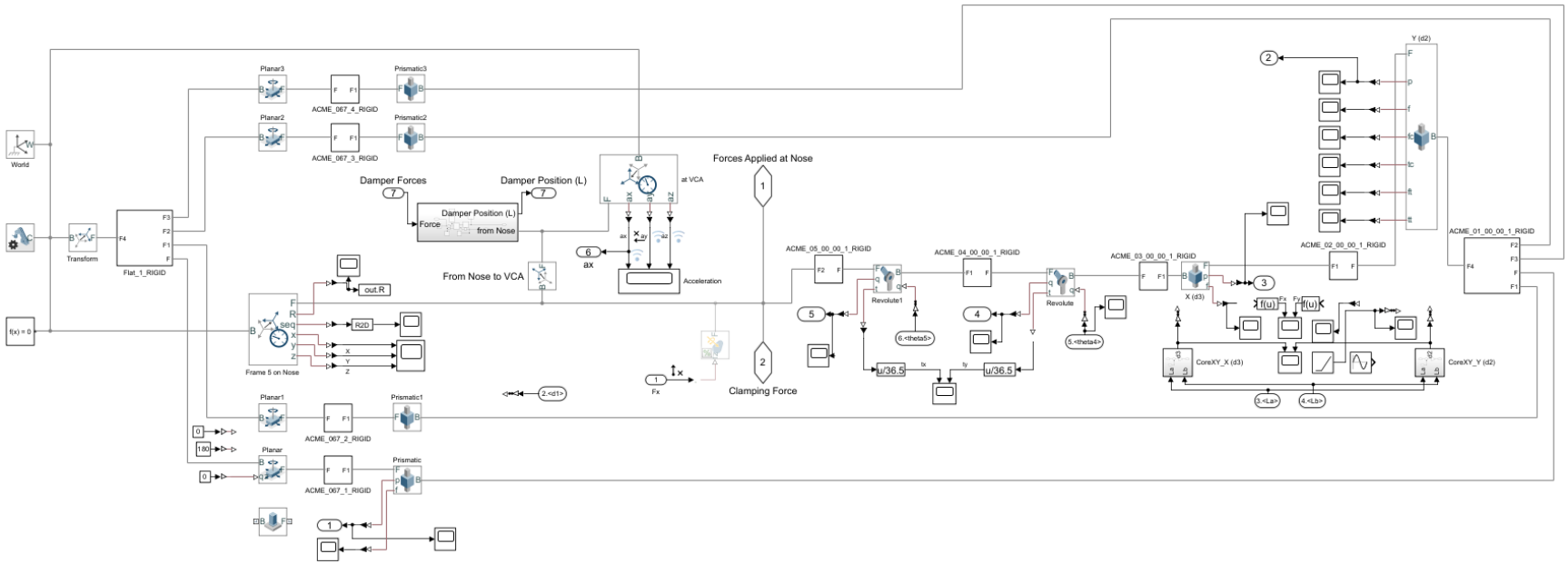

Appendix